uOttawa

L'Université canadienne
Canada's university

FACULTÉ DES ÉTUDES SUPÉRIEURES ET POSTOCTORALES

uOttawa

L'Université canadienne
Canada's university

FACULTY OF GRADUATE AND POSDOCTORAL STUDIES

Jason W. Middleton
AUTEUR DE LA THÈSE / AUTHOR OF THESIS

Ph.D. (Physics)
GRADE / DEGREE

Department of Physics
FACULTÉ, ÉCOLE, DÉPARTEMENT / FACULTY, SCHOOL, DEPARTMENT

Neural Information Processing: Temporal Features and Spike Train Statistics

TITRE DE LA THÈSE / TITLE OF THESIS

André Longtin
DIRECTEUR (DIRECTRICE) DE LA THÈSE / THESIS SUPERVISOR

Leonard Maler
CO-DIRECTEUR (CO-DIRECTRICE) DE LA THÈSE / THESIS CO-SUPERVISOR

EXAMINATEURS (EXAMINATRICES) DE LA THÈSE / THESIS EXAMINERS

P. Johns

A. Neiman

M. Kearn (absent)

R. Metzler

Gary W. Slater
Le Doyen de la Faculté des études supérieures et postdoctorales / Dean of the Faculty of Graduate and Postdoctoral Studies

Neural Information Processing:

Temporal Features and Spike Train Statistics

by

Jason W. Middleton

A thesis presented to the University of Ottawa,
Ottawa-Carleton Institute of Physics,
in fulfillment of the thesis requirement for the degree of
Doctor of philosophy in Physics

Ottawa Ontario,
September 21, 2006

Your file Votre référence
ISBN: 978-0-494-34137-7
Our file Notre référence
ISBN: 978-0-494-34137-7

Abstract

Sensory stimuli are received by sensory neurons and information about these stimuli is further transmitted throughout the brain as electrical signals. These electrical signals do not directly resemble the stimuli they represent, but instead are temporal sequences of discrete electrical impulses, known as action potentials (APs) or "spikes". This thesis aims to further the understanding of how the statistical properties of neural output is determined by the statistical properties of inputs; also it aims to understand what temporal features of the inputs are represented in AP output sequences, or "spike trains".

In the first part of this thesis, consisting of chapters 2 and 3, we study how input signals with long-range correlations impart slow correlations in output interspike intervals (ISIs). These correlations are important for information transmission at plastic synapses, which is dealt with in chapter 3. In the second part of this thesis we examine how the temporal structure of a specific class of relevant sensory stimuli affects the spike train patterning of the neurons they impinge on. Single cell recordings in weakly electric fish, presented in chapter 4 uncover a simple two-cell network responsible for transmitting a narrowband signal and high-order features (i.e. the time-varying contrast, or envelope) of the signal through parallel neural channels. In chapter 5 we examine, using experiments and theory, the single cell mechanism responsible for representing the envelope directly in the AP firing rate of neurons. In chapter 6 we extend these results to show that in parameter regimes where the firing rate cannot convey information about signal envelopes, networks of electrically coupled cells can convey this information through their precise relative spike times.

Résumé

Les stimuli sensoriels sont reçus par les neurones sensoriels et l'information à propos de ces stimuli est subséquemment transmise à travers le cerveau sous la forme de signaux électriques. Ces signaux électriques ne ressemblent pas directement aux stimuli qu'ils représentent, mais sont plutôt des séquences temporelles d'impulsions électriques, connues sous le nom de potentiel d'action (PAs) ou "décharges". Le but de cette thèse est d'améliorer la compréhension de la façon dont les propriétés statistiques de la sortie neuronale sont déterminées par les propriétés statistiques de l'entrée. Elle nous aidera aussi à comprendre quelles caractéristiques temporelles de l'entrée sont représentées dans la séquence de PAs de sortie, autrement dis, dans le train de décharges.

Dans la première partie de cette thèse, les chapitres 2 et 3, nous examinons comment des signaux d'entrée avec des corrélations à long terme imposent des corrélations lentes dans les intervalles inter-décharges (IIDs) à la sortie. Ces corrélations sont importantes pour la transmission de l'information dans les synapses plastiques, ce que nous traitons dans le chapitre 3. Dans la seconde partie de cette thèse nous examinons comment la structure temporelle d'une classe spécifique de stimuli pertinents affect les patrons de trains de décharges des neurones qu'ils mobilisent. Des enregistrements de cellule unique dans le poisson faiblement électrique, présentés au chapitre 4, révèlent que un simple réseau de deux cellules est responsable pour la transmission d'un signal à bande étroite et de caractéristiques d'ordre supérieur (i.e. les variations temporelles de contraste, soit l'enveloppe) du signal à travers des canaux neuronaux parallèles. Dans le chapitre 5 nous clarifions, à l'aide d'expériences et de théories, le mécanisme unicellulaire responsable pour la représentation de l'enveloppe directement par la vitesse de décharge des neurones. Au chapitre 6 nous étendons ces résultats pour montrer que, dans un régime avec des paramètres tel que la vitesse de décharge ne peut pas communiquer d'information sur l'enveloppe du signal, des réseaux de cellules couplés électrotoniquement peuvent comporter cette information dans le timing relatif des décharges.

Acknowledgements

I'd like to thank André and Len for their endless enthusiasm for science... it's been a pleasure working with them over the past few years. Thanks to my family and friends back home for supporting me throughout the years and helping me get through school. Thanks to Brent for his constant encouragement and for being a great friend. No thanks to his poor personal hygiene. Also to the Doiron family for being a family away from home. To Margaret for being my partner in crime and always having my back; bros before... well, you know. Thanks to Bill for his bow-hunting skills. To everyone else in the Lewis, Longtin and Maler labs, past and present, for creating a stimulating scientific environment to work in. Thanks for translating the abstract Gary! This work was funded by NSERC, OGSST and CIHR, so thanks to the Canadian government. Let's hope they continue with their generous support of Canadian science. Thanks to all my other friends in Ottawa for the fun times.

Thesis Format

This is a paper format thesis. Chapters 2 and 4 are published articles and chapter 5 is a submitted article; they have been directly copied and reformatted for this thesis. Chapters 3 and 6 are unpublished works that have been written as preliminary manuscripts, both pending further preparation for submission.

This thesis is a combination of computational, theoretical, and experimental work. The computational work, analysis and experiments were performed primarily by myself with contributions from various co-authors. I was the primary writer of each chapter with corrections offered by various co-authors. I will outline my contributions to each chapter separately:

II. This chapter is a copy of the article:

Middleton, J. W., Chacron, M. J., Lindner, B. and Longtin, A.
Firing statistics of a neuron model driven by long-range correlated noise.
Physical Review E. **68**: 021920 (2003)

This paper is a study of how the temporal correlations of input noise to a neural model shapes the output spike train statistics with connection to signal detection. The numerical simulations were done jointly by M. Chacron, B. Lindner and myself. Analytic expressions were derived by B. Lindner and myself.

III. This chapter is an unpublished manuscript:

This manuscript is a study of the role that presynaptic spike train statistics has in determining the form of temporal filtering of signals transmitted through plastic synapses. I performed all numerical simulations, analytics and analysis.

IV. This chapter is a copy of the article:

Middleton, J. W., Longtin, A., Benda, J. and Maler, L.
The cellular basis for parallel neural transmission of a high-frequency stimulus and its low-frequency envelope.
Proceedings of the National Academy of Sciences USA. **103**:14596-14601 (2006)
This paper outlines the cellular basis and network structure for extracting higher-order stimulus features and transmitting them in parallel to first-order features. I performed all experiments and analysis.

V. This chapter is a copy of a submitted manuscript:

Middleton, J. W., Harvey-Girard, E., Longtin, A. and Maler, L.
Envelope gating and noise shaping in populations of noisy neurons
Submitted (2006)

This paper is a computational and experimental study of the inherent non-linearities in simple neurons that lead to extraction of amplitude modulations, or envelopes, from narrowband input signals. These results are used to propose a new form of noise shaping when a population experiences spatially correlated narrowband rhythms. E. Harvey-Girard prepared the brain slices for recording, while both he and myself carried out the data collection. I performed all the numerical simulations, theory and data-analysis.

VI. This chapter is an unpublished manuscript:

This manuscript extends the work of chapter V and describes how networks of coupled can transmit first-order and higher-order stimulus through first and second order network firing variables. I performed all the numerical simulations, analytics and analysis.

List of Figures

Table of Acronyms

ANOVA	Analysis of Variance
AM	Amplitude Modulation
AP	Action Potential
CV	Coefficient of Variation
DC	Direct Current
DBP	Deep Basilar Pyramidal Cell
EEG	Electroencephalogram
EGp	Eminentia Granularis Posteriori
ELL	Electrosensory Lateral Line Lobe
EOD	Electric Organ Discharge
E-R	Envelope-Response
F-I	Firing-Input
IC	Inferior Colliculus
IF	Integrate-and-Fire
IPSP	Inhibitory Postsynaptic Potential
ISI	Interspike Interval
ITD	Interaural Time Difference
GABA	Gamma-Aminobutyric Acid
GTP	Guanosine Triphosphate
LIF	Leaky Integrate-and-Fire
LIFDT	Leaky Integrate-and-Fire with Dynamic Threshold
MEG	Magnetoencephalogram
nP	Nucleus Praeminentialis
OU	Ornstein-Uhlenbeck
PDF	Probability Density Function
PRC	Phase Resetting Curve
PSC	Postsynaptic Current
PSP	Postsynaptic Potential
R-R	Response-Response
RAM	Random Amplitude Modulation
S-R	Stimulus-Response
SAM	Sinusoidal Amplitude Modulation
SCC	Serial Correlation Coefficient
SNR	Signal-to-Noise Ratio
SSR	Superthreshold Stochastic Resonance
SR	Stochastic Resonance
SRM	Spike Response Method

Table of Contents

CHAPTER 1: INTRODUCTION

1.1 GENERAL NEUROSCIENCE

One of the major tasks of the central and peripheral nervous system is to acquire sensory information that will ultimately be used to guide behaviour, form perceptions or become memories. Sensory neuroscience, and neuroscience in general, is a field traditionally rooted in the biological sciences. As such, its methodology has been largely observational and descriptive in nature. However, over the past years there have been increasing contributions to neuroscience from the physical, mathematical and engineering sciences. These disciplines lend themselves well to sensory neuroscience, in particular allowing a quantitative description of the detection, processing and transmission of sensory inputs. The synergistic relationship between experimental neuroscience and a computational description of neural processing will undoubtedly continue as the field of neuroscience evolves.

In the late 1800s Ramón y Cajal (1) speculated that the brain is comprised of discrete elements, interconnected with each other to carry out specific neural tasks. It was not until the discovery by Camillo Golgi of a procedure involving silver staining of brain tissue and visualization under a light microscope that Cajal could begin a systematic description of neural anatomy. Thus began the view of the brain as a machine composed of discrete, highly complex computational elements. Altogether there are on the order of 10^{12} neurons in the human brain with different morphologies and connections, located in various functional structures. Ignoring the complexity of a single neuron itself, we are faced with a seemingly limitless computational capacity of the brain, due to the potential combinatorial complexity of neural connections. One of the primary goals in

neuroscience is to understand how the interplay between single cell complexity and structured connectivity leads to the vast repertoire of behavioural and perceptual responses.

The basic elements describing the microstructure of the brain are illustrated in Fig. 1-1. A typical neuron is composed of: (i) a soma, or cell body, similar in size, shape and cytoplasmic content to many other cells in the body, (ii) an axon, which is a lengthy cylindrical extension of the cell membrane, and (iii) dendrites which typically emanate from the cell body and have intricate branching structures (1-3). The axonal branches of a neuron end in small swellings called boutons that are in close proximity to the dendrite of other neurons. The specialized regions of contact between axonal boutons and dendrites are called synapses. Transmission of information in the nervous system is usually unidirectional: from the axon to dendrite via the synapse. Stereotyped electrical signals are generated near the soma in a location called the axon hillock, set apart by the electrical properties of its cell membrane; these signals propagate down the axons and, upon reaching the boutons, trigger the release of molecules (transmitters) that excite or inhibit the target dendrites. Thus neurons are connected to each other at specialized points of contact between axons and dendrites, called synapses. The electrical properties of the neural membrane and the function of synapses will be described in more detail in sections 1.3 and 1.4 of this introduction.

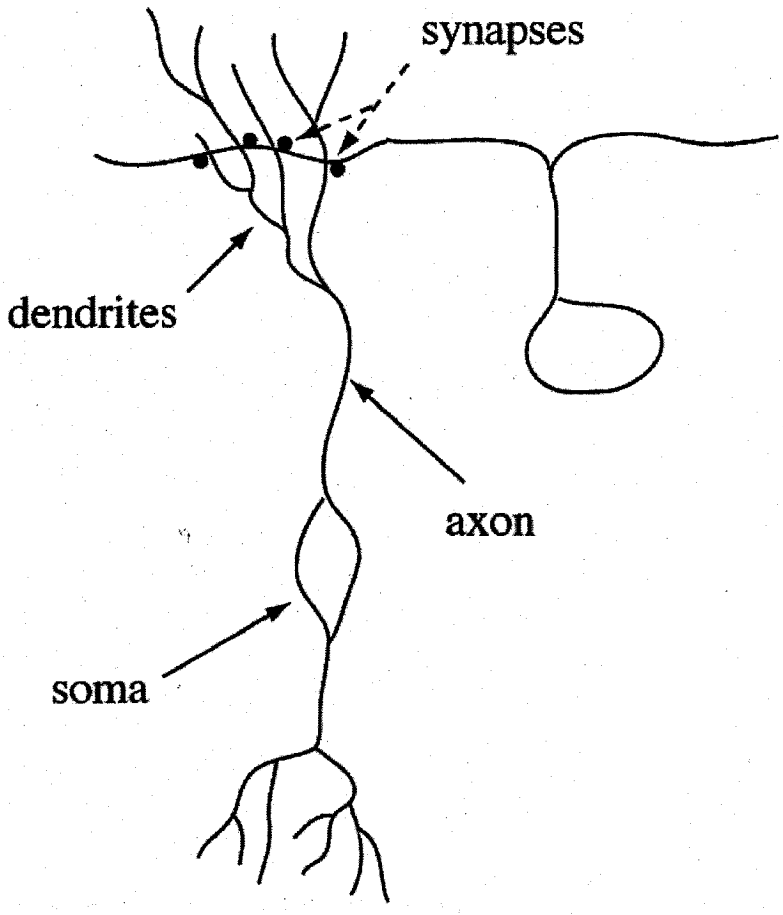

Figure 1-1: The basic components of neurons, the units of computation in the brain. A typical cell consists of a soma, an axon and dendrites. Neurons are interconnected with each other via synapses, typically located at the termination of one neuron onto the dendrite of another.

1.2 SENSORY SYSTEMS AND ELECTRIC FISH

The understanding of sensory processing is aided by the study of a plethora of different animals, humans least of all. Sensory experience involves the receipt of some environmental factor (stimulus) by an observer; this environmental factor is then transformed by lower brain centres into the "language of the brain" and relayed to higher brain centres where it is used for higher cognitive function, such as sensory perception, working memory formation or long term memory storage. Different species have various strengths and weaknesses when it comes to interacting with their sensory environments, and so it makes sense to study the sensory modality for which a particular species has been well adapted. Some examples include audition for barn owls, olfaction for insects (4), and vision for primates (5). Outside the typical range of sensory modalities we are familiar with in our everyday experience, there are sensory "champions", species who have highly specialized sensory cues and sensory organs with which to detect them (6). These unique sensory systems, while not utilized by humans, offer the study of specialized aspects of sensory processing. A common problem facing many different sensory systems is to extract multiple types of weak signals that interfere with each other and are contaminated by noise. There may be similar adaptations to solve these problems; thus the "champion" systems offer an opportunity to investigate well-developed common computational adaptations.

Weakly electric fish offer such an opportunity. The focus of part of this thesis concerns the study of the electrosensory system of the species *Apteronotus Leptorhynchus* (shown in Fig. 1-2 A), a species indiginous to South America (7). They

use a highly evolved set of cutaneous electroreceptors that are a form of modified hair cell (hair cells are the receptors of the evolutionarily related auditory system). In contrast to other aquatic animals that have electroreceptors (sharks, rays, paddlefish, etc.) weakly electric fish require a specific frequency of time-varying electrical input. This input comes from a self-generated quasi-sinusoidal electrical discharge known as the electric organ discharge (EOD). The source is a caudally located organ that consists of, in most cases, a series of modified muscle cells that, upon activation by spinal nerves, generate a concerted large-scale electrical impulse (instead of contracting). In rarer cases, and in particular with the species of interest, *A. leptorhynchus*, the EOD comes instead from the capacitive discharge of a series of modified motor nerves (the muscle that they would normally innervate degenerates during development) (8). The EOD sensitive electroreceptors come in two varieties: probability coders and phase coders. The former give a graded response to the amplitude of the EOD, and the later give a response temporally locked to a specific phase of the EOD (9). Environmental modifications of both phase and amplitude of the self-generated EOD form the most important sensory cues for *A. leptorhynchus* (10, 11). A typical EOD waveform and an amplitude modulation conveying environmental information are illustrated in Fig 1-2 C. These two forms of EOD modulations arise from a wide array of environmental sources, such as communication with conspecifics (i.e. same species) or prey objects (Fig. 1-2 B), predators and inanimate background objects. Later we will associate specific temporal forms of signals with specific sources, and discuss the their sensory and behavioural relevance.

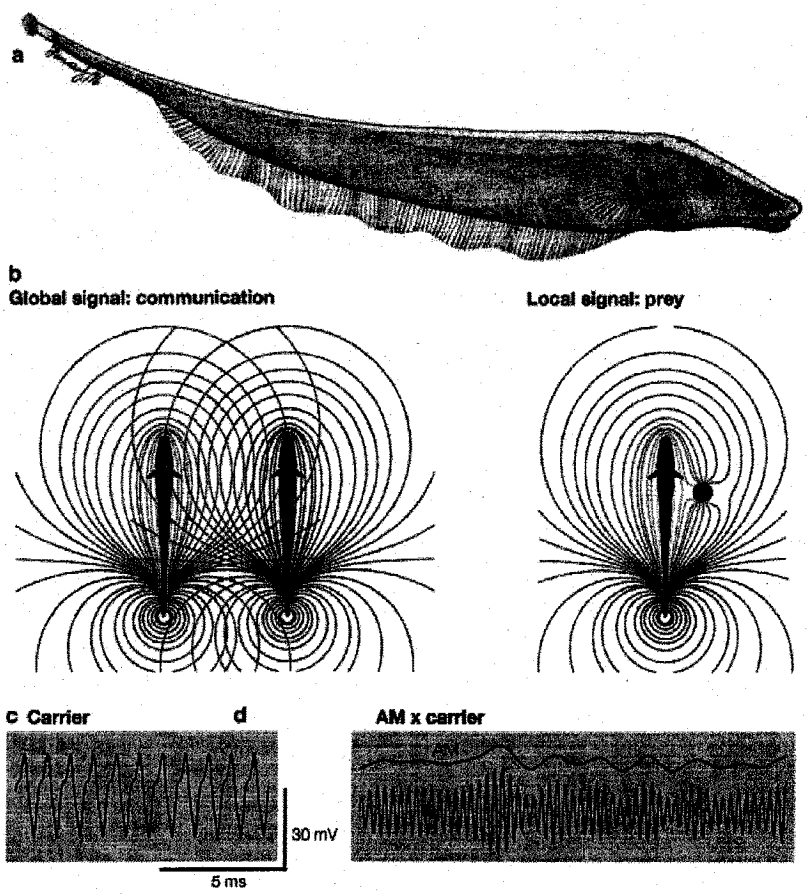

Figure 1-2: **A** The weakly electric fish *A. Leptorhynchus* can detect objects in its environment through amplitude modulations of its self-generated EOD. **B** Conspecifics generate amplitude modulations that are broad in spatial extent (left) while prey objects generate spatially localized amplitude modulations. **C** The high frequency EOD (left) can be amplitude-modulated by objects in the environment, conveying information to electroreceptors. This figure is modified from Krahe and Gabbiani, *Nat Rev Neurosci*, 2004 (12).

1.3 NEURAL MODELS

Three of the most fundamental advances in the history neuroscience were the discovery that the brain is composed of discrete elements, neurons, by Ramon y Cajal (1), the understanding of the nature of the action potential in terms of voltage dependent trans-membrane ion channels, by Hodgkin and Huxley (13) and the discovery of the quantal, chemical nature of synaptic transmission by Bernard Katz (14, 15). The action potential, a rapid large increase in the trans-membrane voltage (depolarization) followed by a rapid decrease back to resting voltage values (hyperpolarization) was previously observed, but it was not until Hodgkin and Huxley that the underlying physical mechanism was understood, opening the way for detailed recordings and modeling of the electrical activity of neurons. The importance of the action potential cannot be understated; as will be discussed in a following section it mediates the majority of signal transfer between neurons in the CNS and is widely believe to be the substrate itself for information transmission in the brain.

1.3.1 CONDUCTANCE BASED NEURAL MODELS

The cell membrane, nearly impermeable to any flow of molecules, acts as a capacitor to separate charge from the inside to the outside of the neuron. Ions can flow across the membrane through transmembrane protein pores known as ion channels (16). Channels are typically selective to specific ions based on size and valence charge. There are also classes of channels that are not selective, but they are typically lumped together during analysis and mediate the flow of mostly Cl^- and some K^+. This is illustrated in Fig. 1-3 A. In addition to ion channels the membrane also contains ion pumps, proteins that use

the energy from ATP hydrolysis to actively move ions across the membrane to maintain ion specific electrical gradients. Associated with each ion population is a reversal, or Nernst, potential, E_i. This is the value of the transmembrane voltage difference, V, at which the osmotic and electric forces balance so that the transmembrane ion concentration difference is in equilibrium. As a consequence of the conservation of charge we have a balance of currents equation relating the capacitive current to all ion mediated currents across the cell membrane (17):

$$C\frac{dV}{dt} = -\sum_i g_i(V - E_i) \tag{2.1}$$

where g_i is the conductance of each ion channel population, C is the capacitance of the cell membrane, and E_i is the aforementioned reversal potential. The second term on the right is the battery term or electromotive force (EMF) on a particular ion type. Even if the channel is in a conductive state (i.e. high g_i) there will be no current if the membrane voltage is at the reversal potential. At the single channel level, ion channels are not continuously open with a specific permeability. Instead it is in one of two states: open or closed. The conductance is equal to the maximum total conductance times the fraction of channels in the open state. So relating to the single channel, g_i is proportional to the probability of being in the open state. The probability of being in either state can be constant, as is the case for most non-selective or leak channels, or depend on other factors. Voltage-activated channels are sensitive to changes in the membrane voltage, ligand-activated channels respond to extracellularly applied chemicals and messenger-activated channels respond to the release of intra-cellular molecules. Only voltage-

activated channels are discussed here, as they are primarily responsible for action potential generation.

The form of current balance as described by Hodgkin and Huxley is as follows (13):

$$C\frac{dV}{dt} = -g_L(V - E_L) - g_{Na}m^3h(V - E_{Na}) - g_K n^4(V - E_K). \quad (2.2)$$

The first term represents (L) the non-selective leak current. The second term (Na) is the sodium current; the constant g_{Na} represents the maximal sodium conductance (i.e. when all the sodium channels are open), m is related to the probability of channels being in the open state and h is related to the probability of it being in the inactivated state. For potassium (K) currents g_K is the maximum conductance and n is related to the probability of a channel being in the open state.

Qualitatively, the progression of ion currents in an action potential is as follows: at low voltages both sodium and potassium channels are mostly closed. If the membrane voltage reaches a high enough level, sodium channels are the first to open ($m \to 1$), causing the membrane to rapidly depolarize even further. At higher voltages, sodium channels are actively closed ($h \to 0$), which stops the cell from depolarizing further. The time course of the membrane voltage and the sodium and potassium conductances are shown in Fig. 1-4. I will not go beyond a qualitative description for the ionic basis for action potential generation as the following simplified model is used in this thesis wherever modeling is necessary.

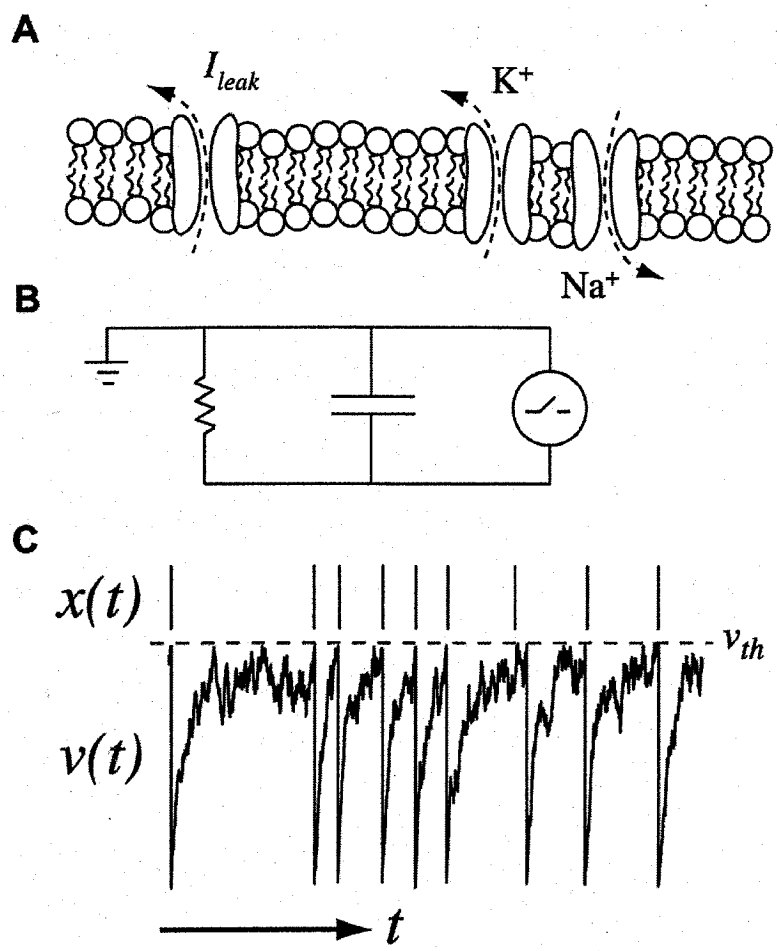

Figure 1-3: The electrical equivalence of a neural membrane and an RC circuit with reset. **A** The lipid bilayer is traversed by protein pores that are selectively permeable to different ion populations. The voltage-dependent activations of the different ion channels act in a concerted fashion to give rise to action potentials. **B** The RC circuit can integrate inputs until the threshold is first crossed from below, triggering a short circuit which resets the circuit to a reference voltage. **C** A simulation of the circuit in **B**, with an input bias and additional noise input. The times of threshold crossing and reset of $v(t)$ can be used to construct a representative neural spike train, $x(t)$.

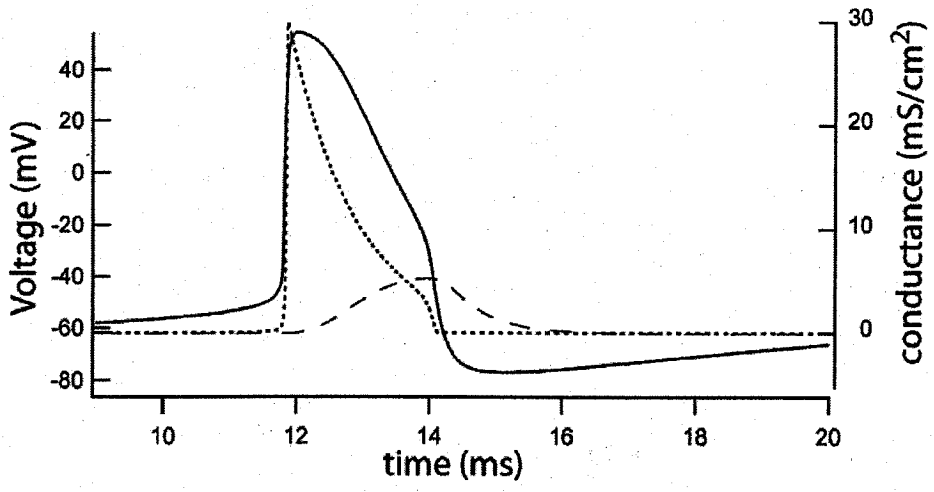

Figure 1-4: The time course of an action potential and the underlying ionic conductances leading to it in a model modified from the original Hodgkin-Huxley equations (18). The solid trace shows the action potential following the course of a fast depolarization, followed by a slightly delayed rectifying hyperpolarization and a slow depolarization to resting level. The dotted trace illustrates the voltage-dependent sodium conductance, which activates rapidly once a threshold voltage is reached and then inactivates once an even higher voltage threshold is crossed. The dashed line shows the slow voltage dependent activation of the potassium conductance.

1.3.2 THE LEAKY INTEGRATE-AND-FIRE NEURON MODEL

The previous model for describing voltage dynamics and AP generation is highly successful at replicating experimental data but is not analytically tractable due to its high dimensionality. The magnitudes of sodium and potassium currents throughout the course of an AP are typically much larger than other current sources, resulting in a stereotyped AP shape. Because of this, the AP time of occurrence, rather than its shape, is usually viewed as having more significance. The leaky integrate-and-fire model (LIF) is very similar in its description of the voltage trajectory to threshold (19, 20). It largely differs in its description of currents during an AP; the LIF model imposes an artificial hard threshold so that when the voltage reaches this level it is explicitly reset to another prescribed value. This replaces the implicit threshold at which spiking sodium channels are activated and the reset voltage the potassium hyperpolarizes to. The LIF has been used successfully to describe neural activity observed in many experimental studies, as well as to allow useful analytic descriptions of their behaviour. In addition to spiking currents, neurons may receive currents coming from synaptic sources that in general could have deterministic and noisy components. This form of the LIF can be written as follows:

$$C\frac{dV}{dt} = -g_L V + \mu + I(t) + \sqrt{2D}\xi(t) \tag{2.3}$$

where g_L is the leak conductance, μ is a lumped parameter that takes into account the leak reversal potential and the mean value of any synaptic inputs and $\xi(t)$ is a Gaussian white noise current . Figure 1-3 B shows the equivalent RC circuit to the LIF dynamics as well

as a sample simulated voltage trace, $v(t)$, and corresponding spike train output, $x(t)$ in Fig 1-3 C.

The noise in Eq. (2.3), when treated as background noise can come from various sources. Spontaneous fluctuations in open and closed states of transmembrane ion channels can contribute to voltage fluctuations (21), but perhaps an even more important source of noise is large numbers of synaptic inputs with random arrival times (22, 23). Using the central limit theorem (24) Stein has shown that in the limit of a large number of synaptic inputs the effective membrane fluctuations become a random walk which can be described by continuous Gaussian white noise (23). More recently it has been shown that if the statistics of the individual synaptic inputs are not Poissonian (i.e. synaptic arrival times are independent of one another), the effective noise will have a different power spectrum (defined in section 1.6.3) from that of Gaussian white noise (25).

Numerical simulations of equations of the form of Eq. (2.3) throughout this thesis are performed using a Euler-Maruyama approximation scheme (26, 27). The contributions to the membrane voltage at each time step are approximated by a Wiener process with variance $\sqrt{2D/\Delta t}$ so that the voltage update rule becomes:

$$CV(t+\Delta t) = CV(t) - g_L V(t)\Delta t + \mu\Delta t + I(t)\Delta t + \sqrt{2D}N(0,1)\sqrt{\Delta t} \qquad (2.4)$$

where Δt is the fixed integration time step and $N(0,1)$ is a zero-mean Gaussian distributed random variable with unit variance. Equation (1.4) is the discrete approximation of the integral solution of Eq. (1.3), used to find the numerical solution for the LIF neuron model.

1.3.3 THE PHASE OSCILLATOR NEURON MODEL

Another model, used in chapter 6 of this thesis, is the phase oscillator model (28, 29). This model can be obtained by mapping a limit cycle in a state space consisting of membrane voltage and ionic conductances onto a single scalar variable, θ, with periodic boundary conditions. The dynamical model described by the scalar phase variable, θ, is know as the phase oscillator model. It is a convenient description when the dynamics of the system is periodic, and is also useful in geometrically visualizing phase relationships between coupled neurons. The general dynamics of a pair of identical coupled neural oscillators has the form:

$$\begin{aligned} \dot{\theta}_1 &= f(\theta_1) + g(\theta_1, \theta_2) \\ \dot{\theta}_2 &= f(\theta_2) + g(\theta_2, \theta_1). \end{aligned} \tag{2.5}$$

When adding noise to this dynamics, care must be taken in choosing the distribution and correlations describing this noise, if the quantitative effects that noise has in the original system are to be preserved [not used in this thesis, but instead for more realistic phase oscillator models such as the theta-neuron model, see refs. (30, 31)].

1.4 NETWROKS AND SYNAPSES

In the previous section we discussed the electrical behaviour of neurons and their non-linear AP generation mechanism. These are the building blocks for input integration and output signaling. It was briefly mentioned that for the most part AP generation and transmission form the substrate for most long-range information transmission in the nervous system. Here we introduce the biophysical mechanism through which the influence of an AP is transmitted across the junction between two cells, and describe how this mechanism can be modulated by neural activity.

1.4.1 NEURAL CONNECTIVITY: SYNAPSES

The connection between two neurons occurs at a specialized site known as a synapse which usually involves the protrusion of membranes of adjacent cells forming a small, flat separation (≅30 nm) known as the synaptic cleft (2, 3). In the absence of neural activity, the cleft is filled with extracellular fluid of typical ionic concentrations. The sending (via its axon) and receiving (via their dendrites) cells are known as the presynaptic and postsynaptic neurons, respectively. Synapses are not exclusively found at one characteristic site in the neuron; axon-dendritic and axo-somatic synapses vastly predominate in the vertebrate brain but there are examples of dendro-dendritic and axo-axonic connections as well. When a somatically generated AP travels down the axon to the site of a synapse, the local depolarization causes an influx of Ca^{2+} through the voltage-gated, calcium-specific ion channels. The increase in intracellular [Ca^{2+}] causes fusion of the neurotransmitter-containing vesicles with the presynaptic membrane. Neurotransmitters are chemicals which, when exocytosed into the synaptic cleft, diffuse over the short distance to bind with receptors on the extra-cellular, post-synaptic membrane. These receptors are either directly connected to ion channels (ionotropic) or indirectly to ion channels via intracellular secondary messengers (metabotropic), usually G-proteins (requiring GTP for their function). The activation of these ion channels causes transient conductance changes in the post-synaptic membrane whose influence is either excitatory (depolarizing) or inhibitory (hyperpolarizing). The small, transient, deflections they cause in the post-synaptic membrane voltage are known as post-synaptic potentials.

The major inhibitory and excitatory transmitters in the central nervous system are gamma aminobutyric acid (GABA) and glutamate, respectively. Glutamate mainly activates two types of ionotropic receptors called AMPA and NMDA receptors. Both mediate mixed cationic conductances. AMPA conductances are typically fast to activate and de-activate, while NMDA receptors evoke slower conductances. GABA activates two types of receptors: GABAa receptors directly and rapidly activating and de-activating Cl^- conductances, and GABAb receptors indirectly (via G-proteins) activating much slower K^+ conductances. In addition to these two classes of chemical synapses, there are specialized proteins that span the gap between pre- and post-synaptic membranes, directly linking the intracellular fluids of both cells. These pores, also known as gap junctions, mediate (instantaneous) electronic current flow between cells.

The postsynaptic potentials (PSPs; stereotyped voltage deflections) caused by chemical or electric synapses, though not APs themselves, are transmitted to the soma where they are integrated and cause an AP when the somatic voltage threshold is surpassed. In some cases, dendrites may themselves contain highly non-linear, or active (i.e. voltage dependent), ion channels causing smaller APs or spikelets before reaching the soma. Regardless of the type of PSP, their entry into the somatic membrane dynamics can be modeled using terms such as $S(t)$:

$$S(t) = \begin{cases} \alpha^2 t e^{-\alpha t} & , \quad t \geq 0 \\ 0 & , \quad t < 0 \end{cases}. \tag{2.6}$$

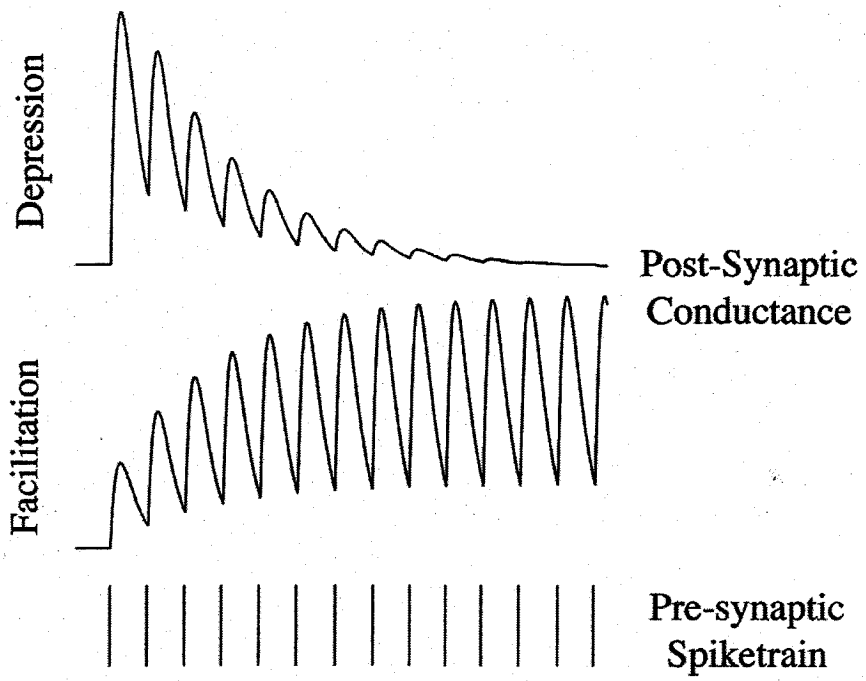

Figure 1-5: The effects of plasticity on postsynaptic conductances. The top trace illustrates the attenuating effect of depression on the postsynaptic conductance, in response to a repetitive presynaptic spike train (bottom), when the synapse exhibits depression. The bottom trace illustrates the enhancing effect of facilitation on the postsynaptic conductances, in response to a repetitive presynaptic spike train (bottom), when the synapse exhibits facilitation.

1.4.2 SYNAPTIC PLASTICITY

Common to many synapses is a form of firing activity history-dependence known as plasticity. Plasticity is the process where repeated synaptic transmissions cause a change in the efficacy of the synaptic transmission itself (2). Facilitation and potentiation are forms of plasticity where repeated transmission of events causes an increase in the magnitude of currents through the post-synaptic membrane. Depression has the opposite effect whereby the magnitude of the post-synaptic current is reduced in response to repeated transmission. Plasticity can be implemented by feedback mechanisms occurring at either or both the pre- and post-synaptic sites, and occur on many different time scales. Synaptic plasticity is believed to be important, not only as a potential substrate for long-term memory storage, but is also in filtering time-varying inputs through the synapse (32, 33). Figure 1-5 illustrates qualitatively the effect that synaptic plasticity has on the conductance and the postsynaptic cell due to repeated action potential stimulation. The presynaptic spike train (Fig. 1-5, bottom) drives the postsynaptic conductance. In the case of depression (Fig. 1-5, top) the amplitude decreases with repeated stimulation and in the case of facilitation (Fig. 1-5, middle) the amplitude increase with repeated stimulation.

1.5 NEURAL CODE

The computational nature of the brain necessitates some form of code used in information transfer and to computations. The question of the basis of the "neural code" is still under debate. The dominant view is that the code involves patterns of action potentials being transmitted between neurons and neural assemblies. In contrast to this, a growing body of evidence is highlighting the importance of glial cells in information transfer (34-36).

Glial cells outnumber neurons in the CNS, but were previously relegated to the supporting roles of providing nutrients and guiding neuronal growth. They do, however, form a network through which slower, graded voltage signals can be propagated. These can, in turn, regulate neuronal activity. This form of information transmission and processing will not be focused on here; instead we will concentrate on the traditional neural network view of information transmission.

There are two opposing views of the form of code that spiking neurons can be used to implement: a rate code and a temporal code. According to the rate coding doctrine, stimuli are encoded in the average firing rate of a population of neurons (37). In this scenario, the high variability of neuronal responses to similar inputs is detrimental for signal fidelity and must be averaged out amongst neurons in a population to achieve a clean signal. As a result of the required averaging the spike times of individual neurons convey no information. An alternative view is that precise spike timing of individual neurons is important in conveying information in an efficient manner (38, 39). If the pattern of action potentials a neuron emits is reliable and reproducible given a particular time-varying input, theoretical analysis has shown that the capacity of the neuron as an information channel could be high (38, 40), even when the spike times do not directly reflect the population-averaged firing rate.

1.6 EXPERIMENTAL TECHNIQUES & ANALYSIS

In the previous sections we discussed the importance of the action potential as a unit of information. In order to determine action potential times we must have access to the transmembrane voltage. I will now review basic electrophysiological techniques and tools used to obtain the data component of this thesis. Figure 1-6 is a schematic of the

basics of single cell recording. The transmembrane voltage is measured by placing a voltmeter in parallel with the membrane. A microelectrode is advanced into the cell membrane and the voltage difference between this electrode and a nearby reference electrode is measured and then passed to a data acquisition board on a personal computer where it is stored for further analysis. The microelectrodes are constructed by heating a borosilicate micropipette (I.D 0.86 mm; O.D. 1.5 mm) with a tungsten filament in a commercial microelectrode puller (Flaming Brown). Tension is applied across the pipette so that, as it heats up, it is stretched and eventually breaks leaving a fine, needle-like tip (<1 μm). This tip can then be positioned across the cell membrane inside the cell with a motorized micro-manipulator with sub-micrometer precision (Inchworm, Burleigh) without excessive damage to the cell membrane. The microelectrode is filled with a highly conductive ionic solution (3M potassium acetate, KAc) and is connected to complete the circuit with a wire, usually chloridized silver to reduce fluid metal junction potentials. The voltmeter-electrode circuit forms a voltage divider on the transmembrane voltage (Fig. 1-6, right). The measured voltage will be $V_m R_{in} / (R_{in} + R_e)$ where V_m is the transmembrane voltage, R_{in} is the input resistance of the amplifier and R_e is the resistance of the microelectrode. If the input resistance of the amplifier is sufficiently high, the true membrane voltage will be recorded. This mode of recording is known as "current clamp" from the fact that the current drawn by the recording device is clamped to zero.

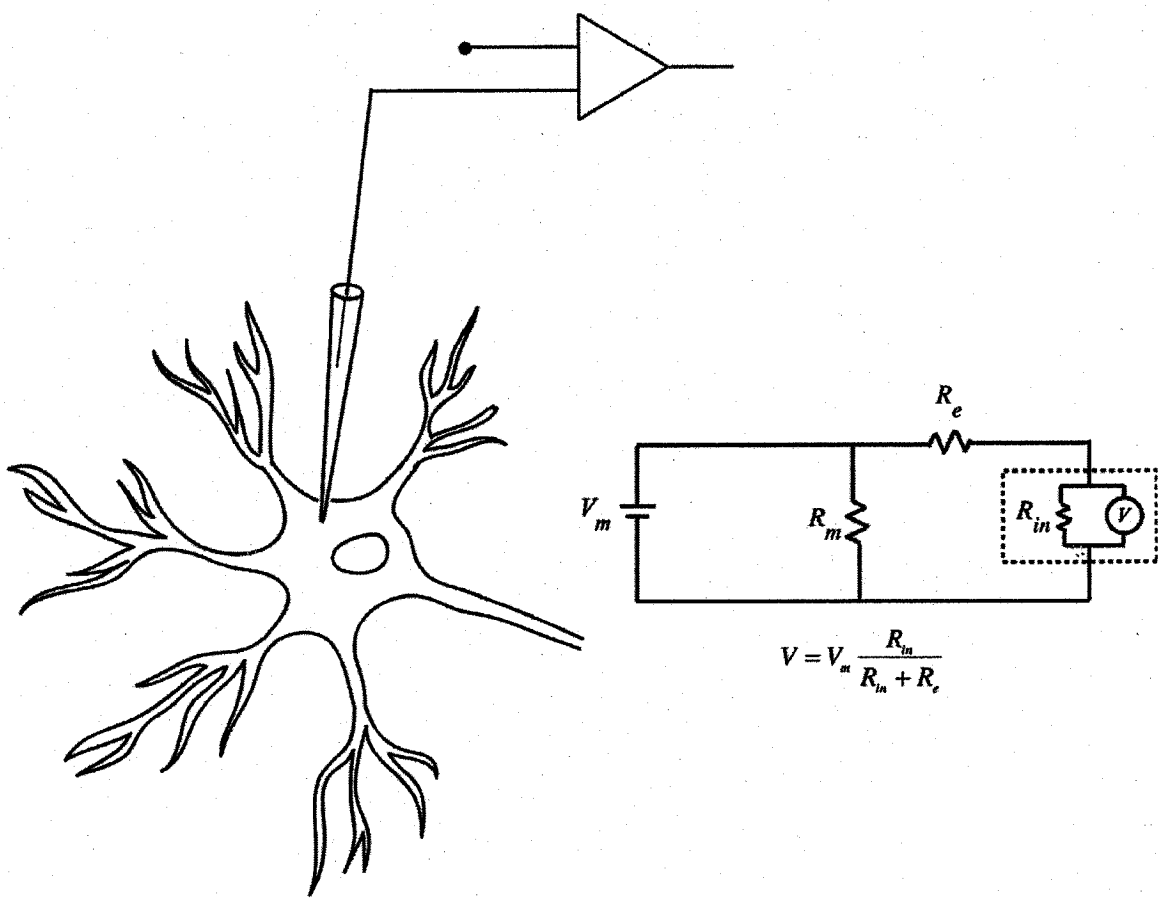

Figure 1-6: An illustration of the essential technique of electrophysiology. A microelectrode is advanced towards the cell (left), either through an intact brain or in a brain slice, and then is placed just exterior to the cell body or pierces the membrane to obtain intracellular potentials. The difference in the microelectrode potential with respect to some reference electrode, placed in the nearby brain tissue, is then amplified and stored on a personal computer. On the right we see the equivalent circuit including the cell membrane, the micorelectrode and the recording device. If the input resistance is high enough the observed voltage, V, will be close to the true transmembrane voltage, V_m.

1.6.1 IN VIVO EXPERIMENTAL TECHNIQUES

The goal of the *in vivo* experiments presented in this thesis is to explore sensory processing in the electrosensory lateral line lobe (ELL) of weakly electric fish. The ELL is a brain nucleus, located in the hindbrain, that performs the first extensive processing on electrosensory signals. Fish are first anaesthetized by placing them in tank water with 0.2% 3-aminobenzoic acid ethyl ester (MS-222, Sigma) and then transferred to a custom made stereotax where they are respirated with the same oxygenated, anaesthetic solution. Local anaesthetic is applied to the dorsal side of the head above where the ELL is located, a small area of skin is removed and then a high-speed dental drill is used to clear away the exposed cranium. Once the eminentia granularis posterior (EGp) is visible (allowing microelectrode access to the ELL) the respiration fluid containing anaesthetic is substituted by water from the fish's housing tanks. The fish is then immobilized by an intramuscular injection of pancuronium bromide (1 μL/1g body weight, Sabex, Boucherville, Quebec) and then transferred to a tank with 28°C water so that all but the exposed brain is submerged.

The aforementioned electric organ discharge (sect. 1.2), or EOD, unperturbed by the stimulus was recorded between the head and tail of the fish using two vertical carbon rods (11 cm long, 8 mm diameter). Two silver-silver chloride wires, insulated except at the tips, spaced 2 mm apart, and oriented perpendicular to the rostral-caudal axis of the fish were place approximately 1mm away from the fish's body. Amplitude modulations of the EOD were created by sampling the EOD using head-tail carbon electrodes, multiplying this EOD with the desired modulation and delivering this signal, in phase

with the fish's own EOD, via stimulation electrodes of either local (spatially focal) or global (spatially extent) geometry. The output of the stimulation electrodes was attenuated so that when combined with the self-generated EOD, it produced the correct signal contrast (i.e. stimulus amplitude relative to the EOD amplitude). The stimulation electrodes in global geometry consisted of two carbon rods (20cm long, 8mm diameter) placed laterally, on either side of the fish 10cm away, with each electrode oriented parallel to the rostral-caudal direction. In local geometry two thin tungsten wires, insulated except at the tips, with a spacing of 2mm were place 5mm away from the surface of the fish perpendicular to the body axis. Microelectrodes are advanced through the EGp, roughly 700 μm below the surface of the brain until the cell body layer is reached (cross section shown in Fig. 1-7 A). Action potentials from single units were recorded either intracellularly with borosilicate microelectrodes (70-140 MΩ, filled with 3M KAc) or extracellularly with tungsten wire electrodes (1MW, TM33C10, WPI, Sarasota, FL) that were advanced with a piezoelectric microdrive (Inchworm, IW-711, Burleigh, Fishers, NY) into the ELL.

The extracellular potential, the EOD, the transdermal potential, and the attenuated stimulus were digitized at 20kHz with a 12-bit Multi-IO board (PCI-MIO-16E-4; National Instruments, Austin, TX) on an Intel Pentium IV 1.8 GHz Linux personal computer. Spike and EOD detection, stimulus generation and attenuation, and pre-analysis of the data were performed on-line during the experiment within Online Electrophysiology Laboratory (OEL) software. Analysis was performed offline using

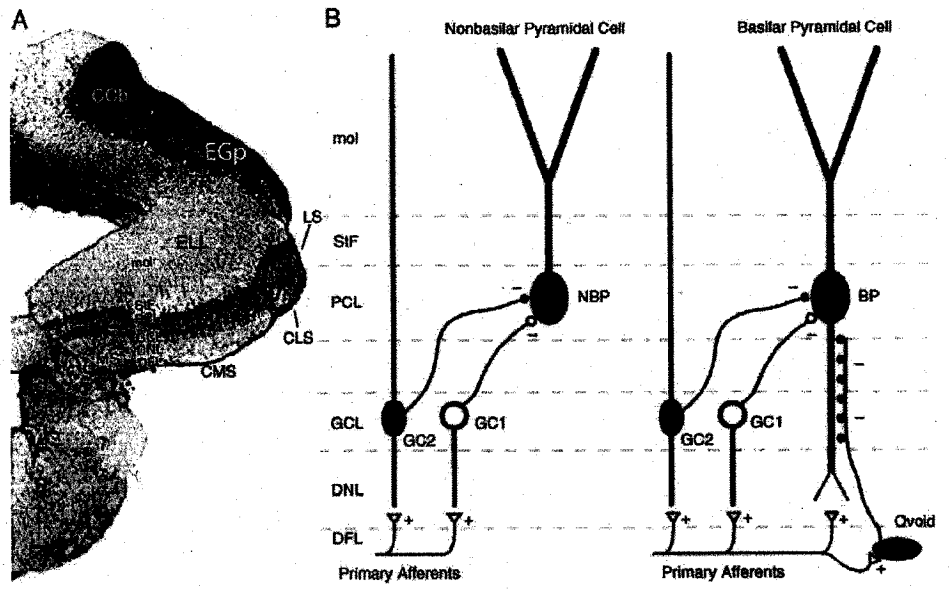

Figure 1-7: A cross section of the brain of *A. Leptorhynchus* displaying the relative positions of the EGP and ELL and a schematic diagram of the connections between the primary neurons and local interneurons in the ELL. **A** Microelectrodes are advanced vertically downward through the EGp, typically over a distance of around 700 μm to record from pyramidal cell bodies in the cell body layer of the ELL. **B** Basilar pyramidal cells (right) receive direct excitatory inputs from primary afferent inputs on their basilar dendrites; afferents also excite several classes of inhibitory interneurons which then project onto pyramidal cells. Nonbasilar pyramidal cells (left) receive inputs from only inhibitory interneurons. Figure modified from Berman et al. *J. Neurophysiol.* 1998 (41).

Matlab software (Mathworks, Natick, MA). All experimental protocols were approved by the University of Ottawa Animal Care Committee.

1.6.2 IN VITRO EXPERIMENTAL TECHNIQUES

ELL slices were prepared for in vitro recording using a technique modified from Mathieson and Maler (1988). Fish of 5-10 g weight were positioned on a custom-made stereotaxic apparatus. The gills were superfused with oxygenated tank water (95% O_2 5% CO_2) through a burette in the fish's mouth, and anesthesia provided by 0.2% 3-aminobenzoic acid ethyl ester (MS-222; Sigma) in the superfusate. The tissue overlying the skull was dissected away under microscopic observation, and the cranium lifted away with forceps after cutting along the lateral cranial sutures with iridectomy scissors. The brain was superfused with an oxygenated (95% O_2, 5% CO_2) artificial cerebrospinal fluid (ACSF) consisting of (in mM) 124 NaCl, 3 KCl, 0.75 KH_2PO_4, 1.6 $CaCl_2$, 1.2 $MgSO_4$, 24 $NaHCO_3$, and 10 D-glucose, pH 7.4. A micro-blade was used to cut the anterior lateral line nerve at the ventrolateral surface of the medulla, sever the spinal cord, and block the brain at roughly a 45° angle at the level of optic tectum. The fish was then immersed in cold (4°C) preoxygenated ACSF and the brain lifted out with a spatula.

The rostral surface of the brain was attached to a pre-cooled aluminum block with cyanoacrylite glue and surrounded with gelatin (20% in distilled water) ejected from a previously cooled syringe (-28°C) to provide support during slice preparation; 550 pm slices were cut by vibratome under microscopic observation in a chamber filled with cold oxygenated ACSF (4°C). Excess gelatin was trimmed from a slice using forceps and iridectomy scissors, and the slice floated onto a spatula rostral side up for transfer to an in

vitro recording chamber. Slices were maintained as an "interface preparation" at room temperature by perfusion of oxygenated ACSF (l-2 ml/min) and superfusion of humidified 95% O_2, 5% CO_2 gas. Dissection was completed in about 15 min and the tissue was allowed 1.5 h for recovery and equilibration before recordings were carried out.

Intracellular recordings were made in the pyramidal cell layer of the centromedial and centrolateral segments of the ELL with 3M potassium acetate–filled electrodes (80–120 MΩ). Electrical signals were amplified (Axoclamp-2B, Axon Instruments), filtered (10 kHz cutoff), digitized (ITC-16, Instrutech, Port Washington, NY), and analyzed off-line (IgorPro, Wavemetrics, Lake Oswego, OR). All experiments were software-controlled (A/Dvance, McKellar Designs, Vancouver, BC, Canada or Pulse Control, NIH). All experimental protocols were approved by the University of Ottawa Animal Care Committee.

1.6.3 DATA ANALYSIS

The focus of the mose of this thesis is the capability of neurons to transfer information down axons and across synapses to other neurons. With this in mind, the quantification of information should be done with respect to the action potential sequence, not the full time course of the transmembrane voltage. Since the voltage trajectory during an action potential is stereotyped, only the spike times themselves are important. The spike train can thus be represented mathematically as a time-varying signal, $x(t)$, by a sequence of Dirac detla functions:

$$x(t) = \sum_i \delta(t - t_i) \tag{2.7}$$

where $\{t_i\}$ is the set of spike times.

If the neuron receives a time-varying input, $S(t)$, we can ask how well the output spike train linearly represents the input. This representation is quantified by the coherence function (24). The coherence function between two time varying signals, in this case $x(t)$ and $S(t)$ is:

$$C_{XS}(f) = \frac{|S_{XS}(f)|^2}{S_{XX}(f)S_{SS}(f)}, \quad 0 < C_{XS}(f) < 1 \tag{2.8}$$

where $S_{XS}(f)$ is the cross spectral density of $x(t)$ and $S(t)$:

$$S_{XS}(f) = \lim_{T\to\infty} \frac{1}{2T}\left(\int_{-T}^{T} x(t)e^{-i2\pi ft}dt\right)^*\left(\int_{-T}^{T} S(t)e^{-i2\pi ft}dt\right) \tag{2.9}$$

and the autospectral densities, $S_{XX}(f)$ and $S_{SS}(f)$, are defined similarly.

The types of delivered stimuli/signals used in this study to test neural responses are either single harmonics or Gaussian noise. In terms of spectral content, tonal structures are ubiquitous in natural sensory systems (42-45), whether they are pure tones or modulated tones. Since studying the response to pure tone driven systems is sometimes analytically difficult a popular method has been to use Gaussian noise, thereby simultaneously testing sensitivity to all frequencies. This also leads to the question of whether or not the processing is linear or nonlinear. A linear ansatz states that the response, in the frequency domain, is expressed as the unperturbed spectrum plus a small correction linearly dependent on the input:

$$\tilde{x}(\omega) = \tilde{x}_0(\omega) + A(\omega)\tilde{S}(\omega) \tag{2.10}$$

where the tilde is shorthand denoting the Fourier transform of the corresponding variable and $A(\omega)$ is the susceptibility of the process $x(t)$ (27) .We can use this to compute the auto-spectrum, cross-spectrum and coherence function:

$$S_{XX}(\omega) = S^0_{XX}(\omega) + |A(\omega)|^2 S_{SS}(\omega) \tag{2.11}$$

$$S_{XS}(\omega) = A(\omega) S_{SS}(\omega) \tag{2.12}$$

$$\begin{aligned} C_{XS}(\omega) &= \frac{|A(\omega)|^2 S_{SS}(\omega)^2}{\left(S^0_{XX}(\omega) + |A(\omega)|^2 S_{SS}(\omega)\right) S_{SS}(\omega)} \\ &= \frac{1}{1 + S^0_{XX}(\omega) \Big/ \left(|A(\omega)|^2 S_{SS}(\omega)\right)}. \end{aligned} \tag{2.13}$$

where S^0_{XX} is the "background" power spectrum of the spike train, i.e. the unperturbed spectrum, in the absence of any stimulus. Using these expressions we can test whether or not the system is linear by comparing the predicted quantities to those obtained directly measured from response at different amplitudes. Another issue of linearity arises when we ask not only what happens when the response magnitude depends on the size of the input, but also on the presence of the frequency components in the signal.

To assess whether a linear model is sufficiently accurate to describe the transfer of a given signal, we can analyze the variability in the responses as a function of frequency. Roddey et al. (47) have shown that the square root of the coherence between two responses, $R(t)$ and $R'(t)$ to the same stimuli $S(t)$ is greater than or equal to the coherence between the stimulus and a single response, i.e. $C_{SR}(f) \le \sqrt{C_{RR'}(f)}$. The equality holds in the case where the transfer is linear. This procedure is illustrated in Fig. 1-8. If a frequency in the stimulus, through the action of the neuron, reliably results in

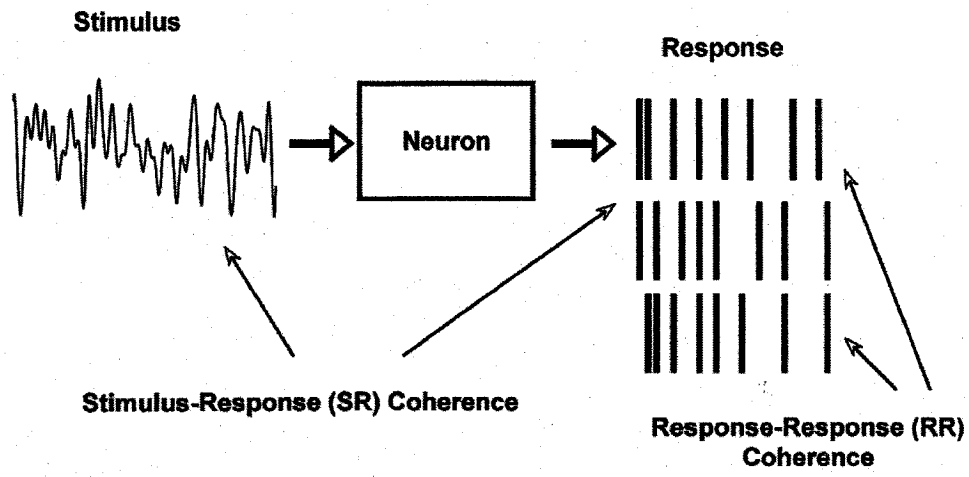

Figure 1-8: A time-varying input to a neuron or neural model results in a patterned output sequence of action potentials, a spike train. This pattern will vary from presentation to presentation, due to sources of randomness in the system. The coherence between the stimulus and spike train can be calculated to quantify the frequency-dependent, linear information transmitted. The same stimulus can be presented repeatedly to form a set of spike train responses. The average coherence between different response can be calculated, the response-response coherence; any discrepancies between the square root of this quantity and the stimulus-response coherence indicate the presence of non-linear processing in the neuron (46, 47).

power not at this frequency then some of the transfer is nonlinear. This is also connected to estimates of the mutual information between the stimulus and the response. The mutual information between a response, R, and a stimulus, S, is given by the reduction in entropy, H, or uncertainty, in observed responses when this stimulus is presented (38, 46):

$$\begin{aligned} I(R,s_j) &= H[R] - H[R|s_j] \\ &= \sum_i p(r_i|s_j)\log_2 \frac{p(r_i|s_j)}{p(r_i)} \end{aligned} \tag{2.14}$$

where we have made use of Bayes' formula (24). Averaging over the entire stimulus ensemble, or set of all possible stimuli, we have:

$$I(R|S) = \sum_j \sum_i p(s_j)p(r_i|s_j)\log_2 \frac{p(r_i|s_j)}{p(r_i)}. \tag{2.15}$$

If the input to and output of the neuron display Gaussian statistics (i.e. the neuron is a Gaussian channel) then an estimate for the lower bound on mutual information, I_{LB}, can be obtained by using the coherence function in eq. (2.13) (38, 46):

$$I_{\mathrm{LB}} = -\int_{f_l}^{f_u} \log_2\left(1 - C_{SR}(f)\right) df \tag{2.16}$$

where f_l and f_u are the lower and upper cutoff frequencies of the stimulus. If the neuron performs any nonlinear operations on the input, the mutual information may be larger than this lower bound estimate. In the same way, we can use the coherences between two responses to two presentations of the same stimulus to estimate the upper bound, I_{UB}, of mutual information (38, 46):

$$I_{\mathrm{UB}} = -\int_{f_l}^{f_u} \log_2\left(1-\sqrt{C_{RR'}(f)}\right)df \tag{2.17}$$

In chapter 4 we will show how the use of the response-response coherence can uncover non-linearities in neural processing. The class of signals used in that and the remaining chapters is a narrowband Gaussian signal (i.e. a signal containing power within a narrow range of frequencies).

1.7 THESIS OVERVIEW

In chapter 2 we study the output statistics of a simple neural model driven by temporally correlated inputs. The model used is the leaky integrate-and-fire (LIF) neuron and the form of input being used is the Orstein-Uhlenbeck process, a form of Gaussian white noise that is low-pass filtered. Temporal correlations are widely observed in signals throughout the brain, whether they are single neuron spike trains, synaptic currents, or more macroscopic signals such as field potentials, electroencephalograms (EEGs) or magentoencephalograms (MEGs). The OU process was used as a starting point in the examination of the influence of temporally structured signals because it is defined by an intensity and a single time constant, the correlation time. We develop analytical expressions describing the input/output relationships both in the time domain and the frequency domain.

In chapter 3 we examine how signal transmission at synapses, the junction points between neurons, is affected by the temporal structure of the signal being passed. Transmission at synapses occurs when an action potential at the pre-synaptic neuron triggers the fusion of neurotransmitter-loaded vesicles into the pre-synaptic membrane.

The neurotransmitter, once released into the synaptic cleft (the space between pre- and post-synaptic membranes) binds with specific receptors in the postsynaptic membrane causing associated ion channels to transiently open, allowing current through the postsynaptic neuronal membrane. Synaptic plasticity is believed to be important, if not the substrate for long term memory storage, particularly in the hippocampus. It is also important for processes such as learning, pattern recognition, and temporal filtering. In the case of temporal signal filtering the common view is that synaptic depression mediates lowpass filtering and facilitation mediates highpass filtering. This filtering dichotomy relies on the fact that a harmonic signal from the sensory periphery is being transmitted through successive layers in terms of neural firing rate, i.e. a low frequency harmonic signal is represented in the brain as a low frequency spike train, and a high frequency signal is represented in the brain as a high frequency spike train.

Here I show that if sensory signals are conveyed as modulations of the firing rate around a constant mean value the roles of depression and facilitation are reversed. Analytic expressions are developed showing that the mean level of plasticity is dependent on the frequency of rate modulation coming from the pre-synaptic spike train. We then use numerical simulations of two LIF neurons connected by a plastic synapse to show that, in addition to attenuating the direct current (DC) component of the post-synaptic current, there is also additional frequency dependent filtering present.

In chapters 4, 5 and 6, I study neural processing of more temporally structured signals, and move beyond the focus of low versus high frequency first-order processing. In particular the focus is on narrowband signals. A narrowband signal contains harmonic

components limited to a frequency range between a lower and an upper cutoff frequency that are typically close together. As opposed to a single time constant characterizing a low pass filtered signal, there are two time constants that characterize narrowband signals: the inverse of the centre frequency and the inverse of the bandwidth. These types of signals are seen frequently in naturalistic signals across many sensory modalities. Auditory signals are comprised of different tones being modulated to produce vocalizations (45). In natural visual scenes, objects are sometimes defined by spatially varying contrast instead of luminance (48); this type of signal when decomposed in terms of spatial frequency content exhibits narrowband structure. Somatosensory stimuli also have complex textural structure (49). It has been observed that rat vibrissae (whiskers) vibrate with narrowband temporal structure. Further away from the sensory periphery many examples of narrowband processes have been observed. For example, in hippocampal and cortical areas, quasi-harmonic rhythmic activity is observed in both normal and pathological brain states (50).

Chapter 4 is a presentation of data obtained from electrophysiological recordings in the electrosensory lateral line lobe (ELL) of the weakly electric fish, *Apteronotus Leptorhynchus*. Giving narrowband sensory stimuli, we observed a response in the primary ELL cell type, known as pyramidal cells, to both the actual frequency component in the stimulus as well as to frequency components related to the bandwidth of the stimuli. Moreover, we ascertained that this response arose specifically from a distinct class of interneurons projecting onto pyramidal cells. It forms the basis of a canonical circuit we have found, in which linear and non-linear stimulus features are processed

separately and in parallel. This type of neural architecture is responsible, in these systems, for certain types of cue invariant responses. Cue invariant responses are neural responses that are similar, independent of whether the relevant sensory object is defined by first order signal features or higher order signal features.

Having localized the neuron responsible for our observations of cue invariant-like narrowband responses in a network context, we then went on, in chapter 5, to examine the general properties of a single neuron that allow it to extract and transmit higher order stimulus features. It has long been known that simple non-linear transformations of a narrowband signal will introduce frequency components, in the spike train, related to the signal envelope. One example non-linearity is rectification. There are many biophysical mechanisms available to single neurons capable of implementing this transformation, but here we focus on a ubiquitous property of spiking neurons, the spike generation threshold. We show how the input/output relationship in reference to the spiking threshold, known as the FI-curve, determines a neuron's ability to extract the higher order envelope from narrowband signals when it is in different parameter regimes. This semi-analytical analysis is supported by electrophysiological recordings of pyramidal cells in a brain slice exhibiting the same FI-curve-dependent envelope processing capabilities. Here the main results are that neurons whose mean level of input places their excitability near the spike generation threshold are proficient at extracting signal envelopes, while neurons whose level of excitability has far surpassed this threshold are poor at extracting signal envelopes, yet still respond well to the direct signal.

In chapter 6, we take the same neurons, far away from spike threshold or in the superthreshold regime, and connect them with other neurons to form mutually coupled networks of oscillating neurons. We review an existing method to represent the limit cycle of neural firing as a scalar variable and to transform signals either from coupled neurons or external sources into forcing terms in this picture. Given the appropriate forcing terms, the neuron they influence will become locked into a fixed relative phase with respect to the source (either a coupled neuron or external signal). If both of these sources are simultaneously present and their preferred phases differ, the new fixed point in phase will attain some intermediate value. We show how this phenomenon can form the basis for a new coding scheme with which the envelope of an entraining carrier signal is represented as a slowly varying phase difference between the two coupled neurons. In the conclusion of this thesis (chapter 7) I summarize key findings of this thesis and elaborate on the connections between the chapters. Finally I suggest some future challenges in extending this work to fit within the general framework of sensory decoding.

CHAPTER 2: FIRING STATISTICS OF A NEURON MODEL DRIVEN BY LONG-RANGE CORRELATED NOISE

2.0 ABSTRACT

We study the statistics of the firing patterns of a perfect integrate and fire neuron model driven by additive long-range (i.e. large time constant) correlated Ornstein-Uhlenbeck noise. Using a quasistatic weak noise approximation we obtain expressions for the interspike interval (ISI) probability density, the power spectral density, and the spike count Fano factor. We find unimodal, long-tailed ISI densities, Lorentzian power spectra at low frequencies, and a minimum in the Fano factor as a function of counting time. The implications of these results for signal detection are discussed.

2.1 INTRODUCTION

Long-range correlations are ubiquitous in nature (51). For example, it is known that natural images (52) as well as music (53) display long-range correlations. These signals serve as natural stimuli to neurons in the visual and auditory systems, respectively. It is known that these neurons exhibit long-range correlations in their spike trains (17, 54), and there is much speculation as to the functional role these correlations might serve. For example, it has been proposed that long-range correlations in neurons provide some advantages in terms of matching the detection system to the expected signal (54, 55).

The regularity shown by neural spike trains will have consequences on stimulus encoding and detection. It has been shown recently that both auditory neurons (54) and electroreceptors of weakly electric fish display both short-range anti-correlations and long-range correlations in the interspike interval (ISI) sequence (56, 57). Long-range correlation of a different kind, namely long-range anti-correlation, have also been observed in paddlefish electroreceptors (58).

It has been shown that short-range anti-correlation and long-range correlation could contribute to give a minimum in spike train variability as measured by the Fano factor (variance-to-mean ratio of the spike count) at a behaviorally relevant time scale (56). In that study the minimum was numerically observed for a leaky integrate-and-fire neuron with dynamic threshold (LIFDT) driven by periodic forcing and weak long-range correlated noise. Our study focuses on the sufficient conditions under which such a minimum can be obtained in a neuron model. Our results show that dynamic threshold, leakage, and periodic forcing are not necessary to obtain a non-monotonic Fano factor. A perfect integrate-and-fire model driven by long-range correlated noise contains all the essential elements to reproduce a minimum in the Fano factor.

We also examine how the long-range correlated noise affects ISI statistics and the spike train power spectrum. The ISI densities and correlation measures are difficult to obtain analytically for the LIFDT, but are possible, with certain approximations, for the perfect integrate-and-fire neuron. Unimodal ISI densities with long tails are analytically obtained, and the correlation present in the driving noise source is shown to carry over to the ISI correlation coefficients. The structure of the power spectrum follows as a consequence of the Fano factor shape. Analytic results are compared with results of numerical simulations throughout.

Section 2.1 presents the model system and outlines the approximations used for the analytics as well as the parameter regime under which they are valid. Section 2.2 characterizes the ISI statistics and shows how their properties reflect the properties of the input to the neuron. In sections 2.3 and 2.4 the statistics of the output spike trains are analyzed using the Fano factor, the spike-spike autocorrelation function and the power

spectral density. The analytic expression for the Fano factor agrees with the simulation results, revealing a minimum for this simple integrate-and-fire model. Finally, the implications of these results are discussed.

2.1.1 MODEL

Here we look at a simple neuron model, the perfect integrate-and-fire neuron, driven by Ornstein-Uhlenbeck (OU) noise, $\eta(t)$. The dynamical equations describing our system are

$$\begin{aligned} \frac{dv(t)}{dt} &= \mu + \eta(t) \\ \frac{d\eta(t)}{dt} &= -\frac{\eta(t)}{\tau} + \sqrt{\frac{2D}{\tau}}\xi(t) \end{aligned} \tag{2.1}$$

where $v(t)$ is the membrane voltage, μ is a constant bias, τ and D are, respectively, the correlation time and variance of the OU process and $\xi(t)$ is Gaussian white noise with autocorrelation $\langle \xi(t)\xi(t') \rangle = \delta(t-t')$. The driving OU process has a Gaussian stationary probability density, $\rho(\eta) = \exp\left[-\eta^2 / 2D\right] / \sqrt{2\pi D}$, and an exponential correlation function, $\langle \eta(t)\eta(t') \rangle = \exp\left[-|t-t'|/\tau\right]$. The voltage is reset to zero once it reaches a threshold value, v_{th}, without resetting $\eta(t)$. For all numerical results, unless stated otherwise we use the parameter values $v_{th} = 2\pi$ and $\mu = 1$. The times at which the voltage crosses threshold, $\{t_k\}$, will be the spike times of the resulting spike train given by the expression:

$$x(t) = \sum_k \delta(t - t_k). \tag{2.2}$$

The spike count, $N(t)$ (i.e. the number of spikes observed in a counting window $(0,t)$) is given by:

$$N(t) = \int_0^t dt\ x(t) = \sum_{0<t_k} \Theta(t - t_k) \tag{2.3}$$

where $\Theta(t)$ is the Heaviside step function. Figure 2-1 shows a realization of the membrane voltage, $v(t)$, and its corresponding driving noise, $\eta(t)$. This illustrates the slow modulating effects of the noise on the ISIs.

An equivalent spike train can be generated without the explicit reset of the voltage, but instead by incrementing the threshold by v_{th} every time the voltage reaches it. Spikes are generated each time the threshold is incremented. In this picture, without explicit voltage reset, the spike count at time t is equal to the threshold divided by the constant v_{th}. The freely evolving dynamics in Eq. (2.1) is equivalent to the Brownian motion of a particle on an inclined plane. Variables $v(t)$ and $\mu + \eta(t)$ are then viewed as the particle's position and velocity, respectively. Provided we have a finite positive bias, $\mu > 0$, the average difference between $v_{th}(N(t)+1)$ and $v(t)$ does not grow unbounded in time, whereas the standard deviation of $v(t)$ grows as $\sqrt{t}$, asymptotically. Consequently, in the asymptotic limit, the statistics of the threshold and of the counting process, $N(t)$, become indistinguishable from the statistics of $v(t)$ as seen in Fig. 2-2.

2.1.2 QUASI-STATIC APPROXIMATION

We wish to look at the effect of long-range correlated noise, so we use a quasi-static approximation for the noise. If τ is much larger than the average ISI, then on short time

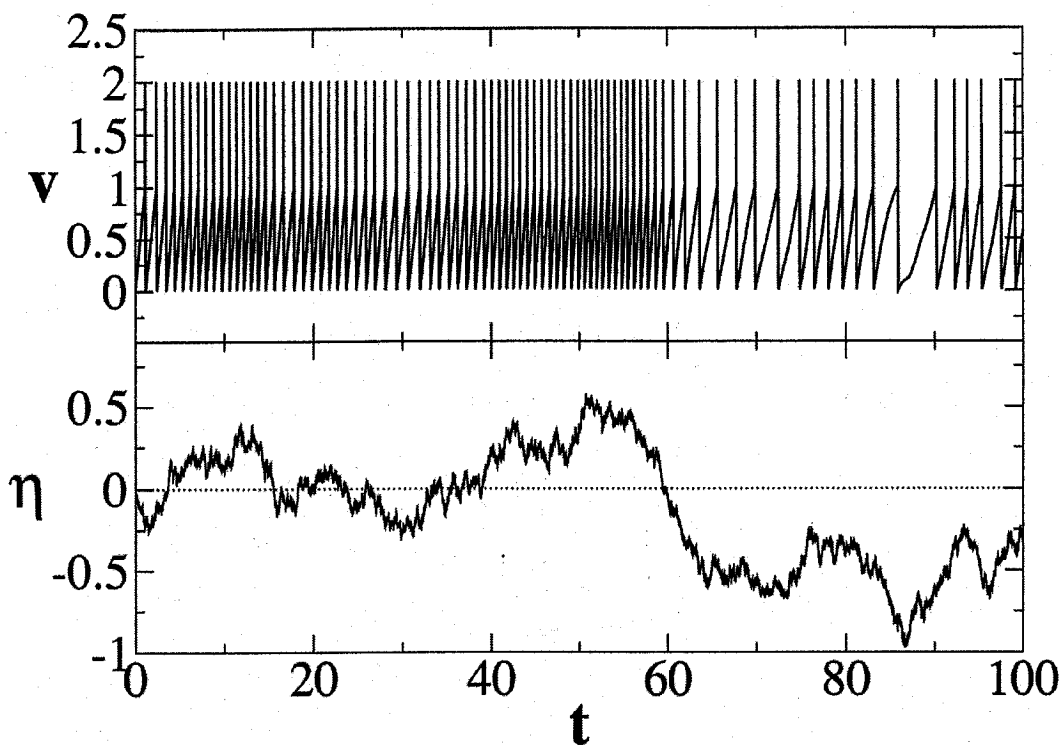

Figure 2-1. A sample spike train with subthreshold voltage variations and the corresponding driving noise. The variance of the noise was set to a large value, $D = 1$, which is used here to visually discern the modulation of the interspike intervals. The time constant used was $\tau = 100$. The vertical bars on top of the voltage trace in the upper panel is not from the dynamics in Eq. (2.1), but were added to illustrate spikes.

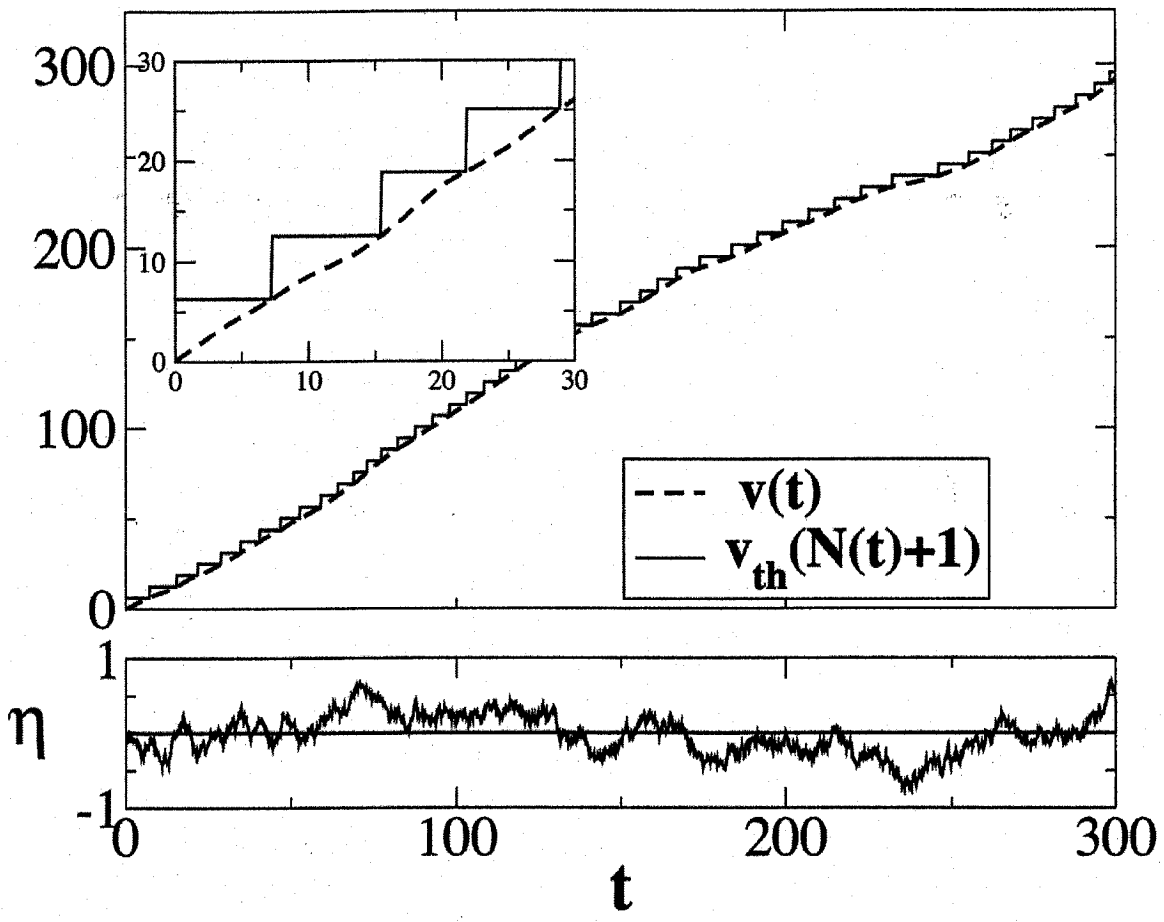

Figure 2-2. The freely evolving voltage, $v(t)$, and the increment threshold variable (upper panel) driven by the OU process $\eta(t)$ (lower panel). The difference between the threshold variable and the voltage are only noticeable on smaller scales (inset).

scales η is approximately constant. In this way we can relate each ISI to a unique value of the OU process

$$I_k = \frac{v_{th}}{\mu + \eta_k} \tag{2.4}$$

where k denotes the index in a sequence of ISIs, and η_k is the value of η at the beginning of the k^{th} interval. Equation (2.4) is a good approximation as long as $\eta_k > -\mu$ and $I_k << \tau$. As η_k approaches $-\mu$ from above, the ISI obtained from the static-noise approximation diverges and is negative for $\eta_k > -\mu$. This is problematic as negative ISIs have no physical meaning. In order to minimize the occurrence of these values we require that:

$$D = \langle \eta^2 \rangle << \mu^2 \tag{2.5}$$

i.e., we use weak long-range correlated noise. Whenever the noise attains values close to or below $-\mu$, the ISI will be of the order of magnitude of the correlation time, τ, during which the OU process returns to values greater than $-\mu$. Clearly, those ISI realizations are not captured by Eq. (2.4), however, their occurrence will be rare due to (2.5) and thus their influence on the firing statistics is negligible.

The approximation (2.4) not only allows us to write down a conditional probability density function (PDF) between I_k and η_k, but it also allows us to reduce this conditional PDF to a delta function due to the unique one-to-one correspondence between η_k and I_k:

$$P(I_k|\eta_k) = \delta\left(I_k - \frac{v_{th}}{\mu + \eta_k}\right). \tag{2.6}$$

2.2 INTERSPIKE INTERVAL STATISTICS

2.2.1 STATIONARY PROBABILITY DENSITY FUNCTION

The first quantity of interest is the stationary PDF of ISIs. In order to obtain the stationary ISI PDF we can average the conditional PDF between I_k and η_k over all values of η_k:

$$P(I_k) = \int_{-\infty}^{\infty} d\eta_k P(I_k|\eta_k)\rho(\eta_k). \tag{2.7}$$

The statistics of the values of the OU process sampled at the beginning of each ISI, η_k, are not the same as for the continuous OU process, η. Imagine we measure the noise value at the beginning of each interspike interval of a long spike train. Then a higher value of noise leads to a shorter interval and hence to more intervals within a given time period than a lower value of η. This problem is known as biased sampling of a stochastic variable (59) and is resolved by a corrective factor given by the inverse interspike interval (see also (60).) Normalization of the corrected PDF yields

$$\rho(\eta_k) = \frac{e^{-\eta_k^2/2D}}{\sqrt{2\pi D}}\left(1+\frac{\eta_k}{\mu}\right). \tag{2.8}$$

For simplicity, this normalization as well as any integration in the remainder of the paper is performed with respect to the full range of noise values, including $\eta < -\mu$, since these values will make a negligible contribution to the integrals we perform. Inserting Eq. (2.8) into (2.7) yields the PDF for the interspike interval density:

$$
\begin{aligned}
P(I_k) &= \int_{-\infty}^{\infty} d\eta_k \delta\left(I_k - \frac{v_{th}}{\mu+\eta_k}\right) \frac{e^{-\eta_k^2/2D}}{\sqrt{2\pi D}} \left(1+\frac{\eta_k}{\mu}\right) \\
&= \int_{-\infty}^{\infty} d\eta_k \delta\left(n_k - \frac{v_{th}}{I_k} + \mu\right) \frac{e^{-\eta_k^2/2D}}{\sqrt{2\pi D} v_{th}\mu} (\mu+\eta_k)^3 \\
&= \frac{v_{th}^2}{\sqrt{2\pi D}\mu} \frac{\exp\left[-(\mu I_k - v_{th})^2/(2DI_k^2)\right]}{I_k^3}.
\end{aligned}
\tag{2.9}
$$

Using these densities the means for the sampled stationary OU process and ISI are respectively D/μ and v_{th}/μ. Note, however, that the PDF decays as $1/I_k^3$ for large I_k according to a power law, in contrast to the white noise driven case (61). This implies a divergence for the second and higher moments revealing again that the approximation made is restricted to ISIs smaller than τ.

Figure 2-3 shows the stationary PDF for fixed τ and several values of D from both numerical simulation of Eq. (2.1) and the corresponding theoretical curves using (2.9). With increasing noise the mean of the density does, in fact, remain the same, at v_{th}/μ, because the shift of the peak towards smaller ISI values is balanced out by the long tails for larger ISI values. Even though we began with a weak noise condition (2.5) the theoretical densities agree with simulation results very well beyond this condition. The agreement holds even for higher noise values (i.e. $D=1$), though not as well as for smaller noise values.

Figure 2-4 shows the simulation and theoretical PDFs for fixed D and various values of τ. The numerical results agree well with the theory, but the agreement breaks down when τ is on the order of the mean ISI. For shorter values of τ, i.e. $\tau < v_{th}/\mu$, the quasi-static approximation is no longer valid.

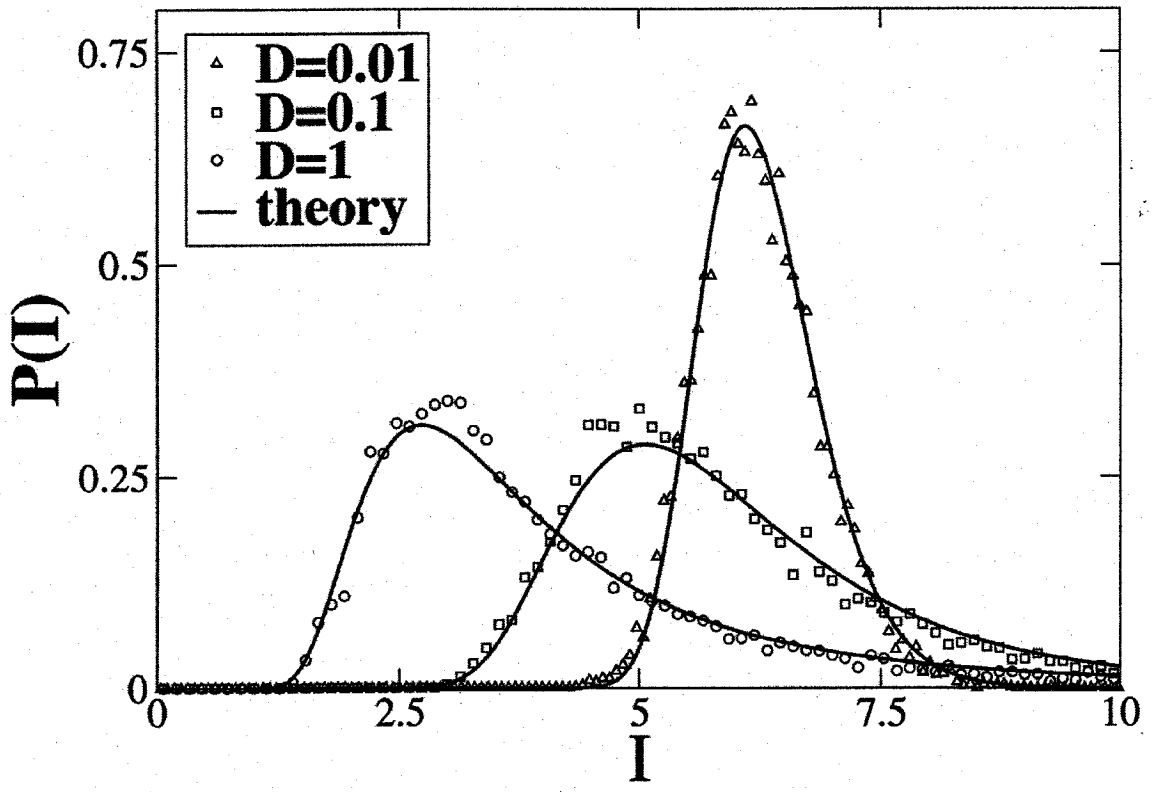

Figure 2-3. Stationary ISI probability densities. Numerical simulations for fixed $\tau = 1000$ and different values of variance, D, along with the theoretical probability densities (2.9). Note that the mean is v_{th}/μ in all cases.

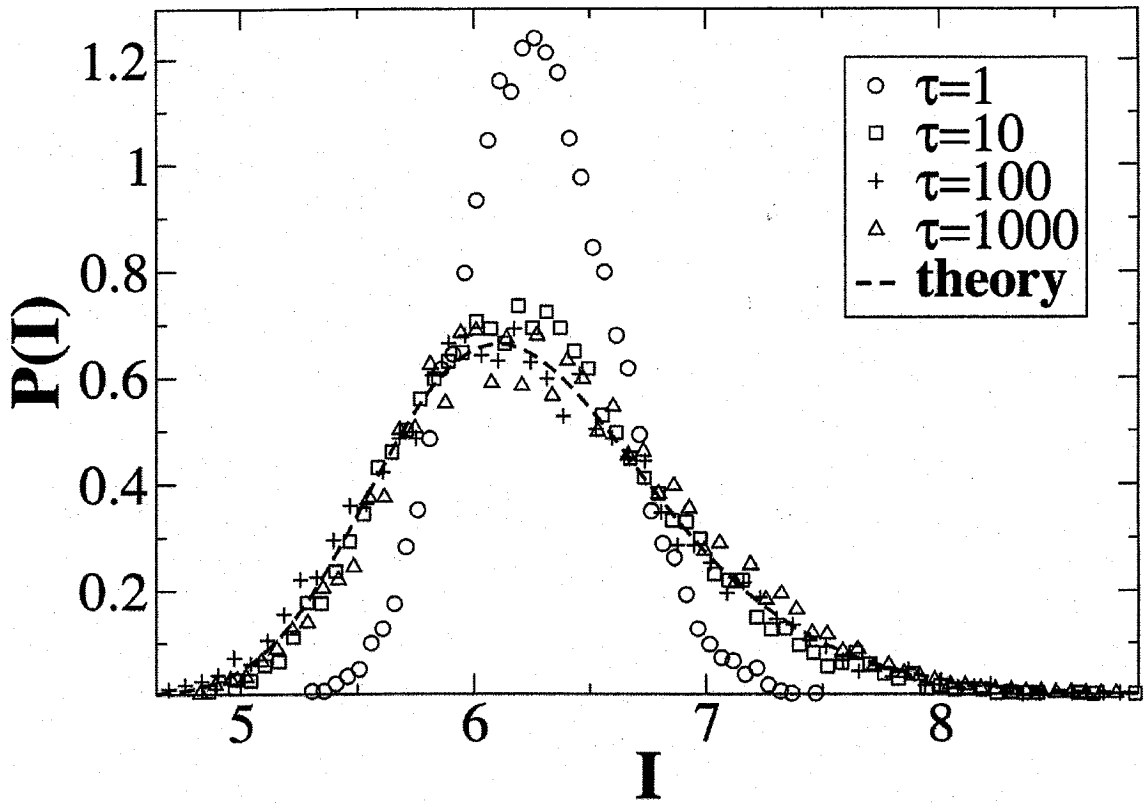

Figure 2-4. Stationary ISI probability densities. Numerical simulations for $D = 0.01$ and different values of the correlation time, τ. The theoretical result (2.9) is independent of τ because of the quasi-static approximation. The quasi-static approximation is not valid for small values of τ.

2.2.2 SERIAL CORRELATION COEFFICIENT

The serial correlation coefficient (SCC) is a measure of correlation between different elements in a sequence of random events. The SCC, ρ_l, in this case, is between two ISIs separated by l intermediate ones. The number l is referred to as the lag, and the SCC at lag l is given by:

$$\rho_l = \frac{\langle I_k I_{k+l}\rangle - \langle I_k\rangle\langle I_{k+l}\rangle}{\langle I_k^2\rangle - \langle I_k\rangle^2}. \tag{2.10}$$

where the averages here are over an ensemble of ISI sequences. The mean values for the k^{th} and the $(k+l)^{th}$ ISIs are the same if the process giving rise to these ISIs is stationary. A simple expression for these SCCs can be obtained first by taking the Taylor expansion of (2.4) about $\eta_k = 0$:

$$I_k \simeq \frac{v_{th}}{\mu}\left(1 - \frac{\eta_k}{\mu}\right) \tag{2.11}$$

provided the assumption (2.5) still holds. We may then approximate the serial correlation coefficient by inserting Eq. (2.11) into (2.10):

$$\rho_l \approx \frac{\langle \eta_k \eta_{k+l}\rangle - \langle \eta_k\rangle^2}{\langle \eta_k^2\rangle - \langle \eta_k\rangle^2} \equiv C_{\eta_k}(l) \tag{2.12}$$

which is simply the autocorrelation function of the sampled OU process. For low noise, the times, t_{k+l}, at which the process is sampled do not deviate much from $t_k + l\langle I\rangle$. This allows us to estimate the ISI correlation:

$$\begin{aligned}\rho_l &\approx C_{\eta_k}(l) \approx C_\eta(l\langle I\rangle) \\ &= \exp\left[-\frac{l v_{th}}{\mu\tau}\right] = \exp\left[-\frac{l\langle I\rangle}{\tau}\right].\end{aligned} \tag{2.13}$$

Although this formula is just a simple estimate it fits the simulation data, Fig. 2-5, rather well. Deviations become apparent for moderate values of the correlation time τ (i.e. in Fig. 2-5, $\tau = 10 \approx \langle I \rangle$) and for larger values of the noise variance (not shown). Numerical simulations have shown that for extremely large correlation times the noise variance needs to be scaled down appropriately in order to maintain agreement with the theoretical expression, Eq. (2.13). Apart from these small deviations, we can state that for weak long-range correlated noise, the exponential correlation of the noise carries over to the ISI statistics and that the "correlation lag" (i.e. the discrete counterpart of a correlation time) is given by

$$l_{\text{corr}} = \frac{\tau}{\langle I \rangle} = \frac{\tau\mu}{v_{th}}. \tag{2.14}$$

2.3 FANO FACTOR

2.3.1 LARGE-TIME ANALYTIC APPROXIMATION

The Fano factor (62), $F(t)$, is the variance to mean ratio of a counting process, $N(t)$, for a given counting time, t. It is useful for determining on which time scales the process is most regular. As discussed in the introduction, the spike count process is equivalent to the freely evolving dynamics of a particle executing Brownian motion on an incline in the asymptotic time limit. In this limit we can use the statistics of the two processes interchangeably, so that we can use the well known Fano factor for Brownian motion (63) as an approximation for the Fano factor of the spike count for large times

$$F_{\text{large}}(t) = \frac{2D\tau}{v_{th}\mu}\left(1 - \frac{\tau}{t}\left(1 - e^{-t/\tau}\right)\right). \tag{2.15}$$

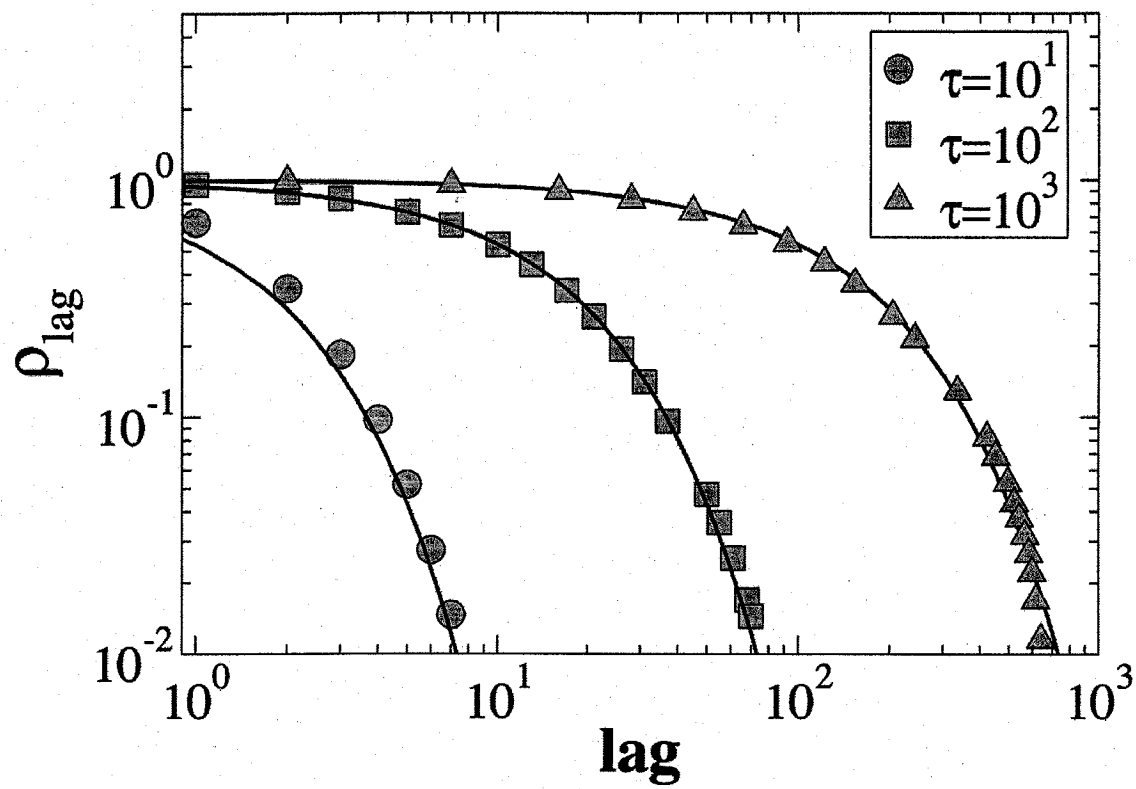

Figure 2-5. The serial correlation coefficient from numerical simulation (symbols) and theoretical result [Eq. (2.13)] (solid lines). Results for three values of the noise correlation time are shown. The variance of the noise used in simulations is $D = 0.01$; the theoretical curves are independent of the driving noise strength.

It is readily seen that for moderate time, $t < \tau$, the Fano factor is $F_{\text{large}} \approx Dt$ (no τ dependence), whereas for $t \to \infty$ we have $F_{\text{large}} \approx D\tau$ (i.e. saturation). Hence, the linear growth of the Fano factor in time (corresponding to the ballistic phase of Brownian motion) is determined only by the variance of noise values, while the correlation sets where the ballistic phase terminates. Figure 2-6 shows $F_{\text{large}}(t)$ for different variances of the OU process with $\tau = 10^3$. The theoretical curves (2.15) converge toward the numerical results for a sufficiently long counting time. The convergence is faster for intermediate noise values as seen in Fig. 2-6. The Fano factor curves reach an asymptotic value given by

$$\lim_{t\to\infty} F_{\text{large}}(t) = \lim_{t\to\infty} F(t) = \frac{2D\tau}{v_{th}\mu}. \tag{2.16}$$

2.3.2 SHORT-TIME ANALYTIC APPROXIMATION

The Fano-factor of the random point process described by our neuron with long-range noise (2.1) approaches 1 in the limit $t \to 0$, which is the Poissonian limit (59). Equation (2.15) is only valid in the large time limit and fails to capture the discrete nature of the point process which becomes apparent at small times (see Fig. 2-6.) If an approximation of the Fano factor for short counting windows times can be found, we can use this expression as well as the large time approximation (2.15) to interpolate values of the Fano factor at intermediate time scales.

The intensity of the long-range correlated noise is small in our approximation. Consequently, over short counting times the spike train appears very regular. Because of this regularity the Fano factor for a deterministic spike train will be a good

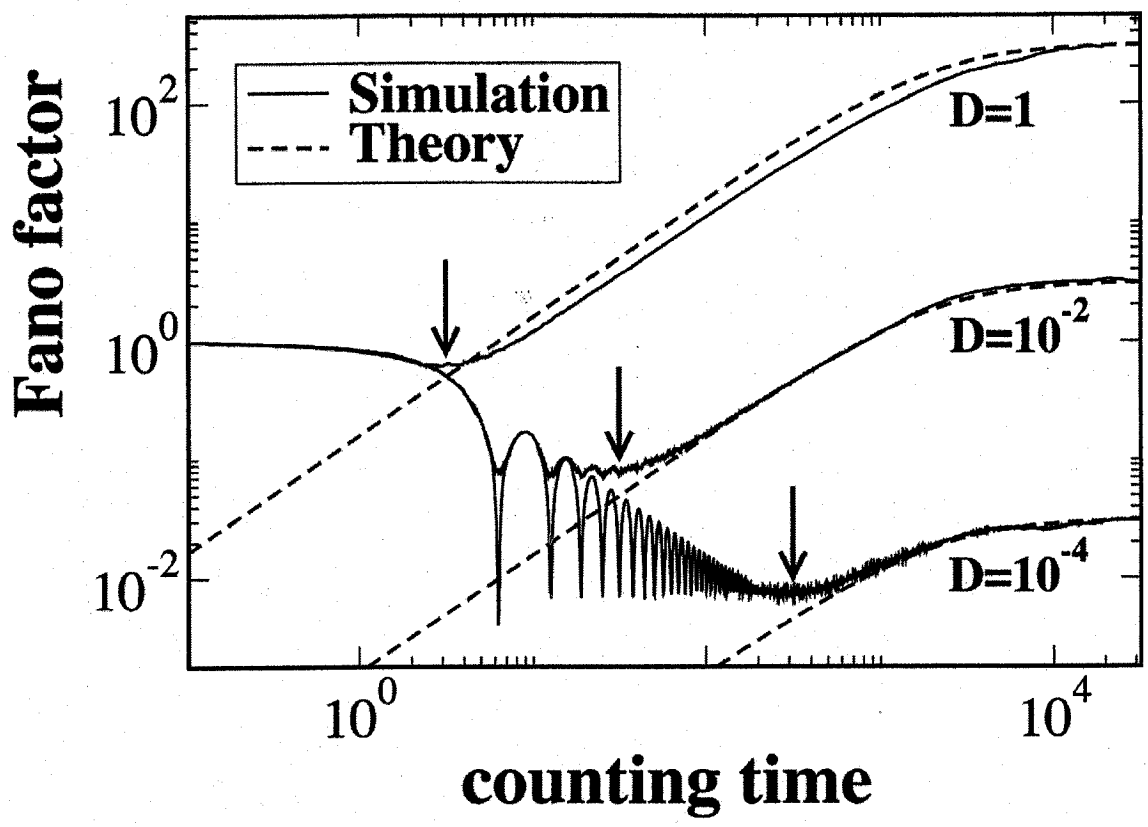

Figure 2-6. The numerical results (solid lines) of the Fano factor for different noise intensities with $\tau = 1000$ for the system of Eq. (2.1). The dashed lines are the theoretical curves obtained from equation (2.15). This theory is valid only in the large counting time limit. The arrows indicate the positions of the minimum in the Fano factor as given by equation (2.23).

approximation. Figure 2-7 shows such a spike train with a given counting time, t. The variable Δ (used here as shorthand for $\mathrm{mod}(t,\langle I\rangle)$) is the difference in time between t and the largest number of integer multiples of $\langle I\rangle$ that t contains. We shall refer to this largest integer as k, which gives us $t = k\langle I\rangle + \Delta$. As Figure 2-7 shows, for a given t, the spike count, N, can take on only one of two values: k or $k+1$. The probabilities of observing these counts are

$$P(i) = \begin{cases} 1 - \dfrac{\Delta}{\langle I\rangle}, & i = k \\ \dfrac{\Delta}{\langle I\rangle}, & i = k+1 \\ 0, & \text{otherwise} \end{cases} \tag{2.17}$$

where i is the index of the spike in the deterministic spike train. From $P(i)$ we can obtain the mean and variance of the spike count:

$$\langle n\rangle = \frac{t}{\langle I\rangle} \tag{2.18}$$

and

$$\langle n^2\rangle = \sum_{i=0}^{\infty} i^2 P(i) = k^2 + 2k\frac{\Delta}{\langle I\rangle} + \frac{\Delta}{\langle I\rangle} \tag{2.19}$$

and thus the variance becomes

$$\langle n^2\rangle - \langle n\rangle^2 = \frac{\Delta}{\langle I\rangle}\left(1 - \frac{\Delta}{\langle I\rangle}\right). \tag{2.20}$$

From this we can obtain an expression for the Fano factor for small counting times:

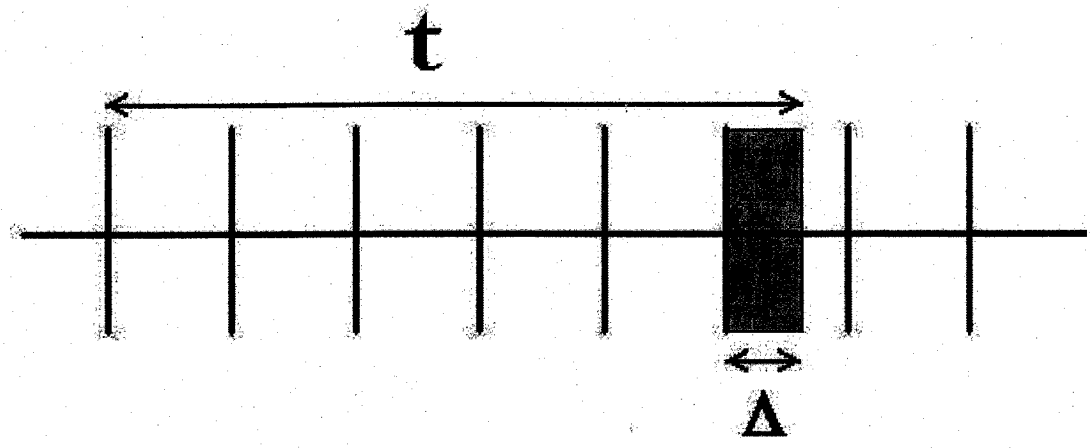

Figure 2-7. A regularly spaced spike train. Δ is the fraction of an ISI that remains after taking out the largest number of ISIs from the counting time, t.

$$F_{\text{small}}(t) = \frac{\langle n^2 \rangle - \langle n \rangle^2}{\langle n \rangle} = \frac{\Delta}{t}\left(1 - \frac{\Delta}{\langle I \rangle}\right) \tag{2.21}$$

The variance of the deterministic regular spike train is a periodic sequence of inverted parabolas with a local maximum of 1/4 located at every odd multiple of $\langle I \rangle/2$. Because the variance does not grow past a finite value in time, the Fano-factor is damped out by the linearly increasing mean and becomes negligible at large time scales.

2.3.3 *FULL-RANGE APPROXIMATION*

The sum of the short-time and the long-time approximations, $F(t) = F_{\text{small}}(t) + F_{\text{large}}(t)$, provides a good fit to data from numerical simulations over the full range of counting windows as can be seen in Fig. 2-8. Figure 2-6 shows that for a finite range of noise intensities the Fano factor exhibits a minimum and it is noteworthy that this crude approximation, $F(t) = F_{\text{small}}(t) + F_{\text{large}}(t)$, gives a very good estimate for the position of the minimum in the Fano factor. By minimum we mean the first local minimum encountered in going from large time values to small ones. It was previously shown that a minimum in the Fano factor indicates an optimal time scale on which to detect two distinct signals (56, 64). Since the variance of the deterministic spike train, Eq. (2.20) is confined to the interval [0,1/4], the small time Fano curve can be approximated by the envelope of its oscillations, $F_{\text{small}}(t) \simeq \langle I \rangle / 4t = v_{th}/4\mu t$. This agrees with our previous definition of the minimum of the Fano factor. This envelope and the large time Fano factor can be used to determine a minimum, given by:

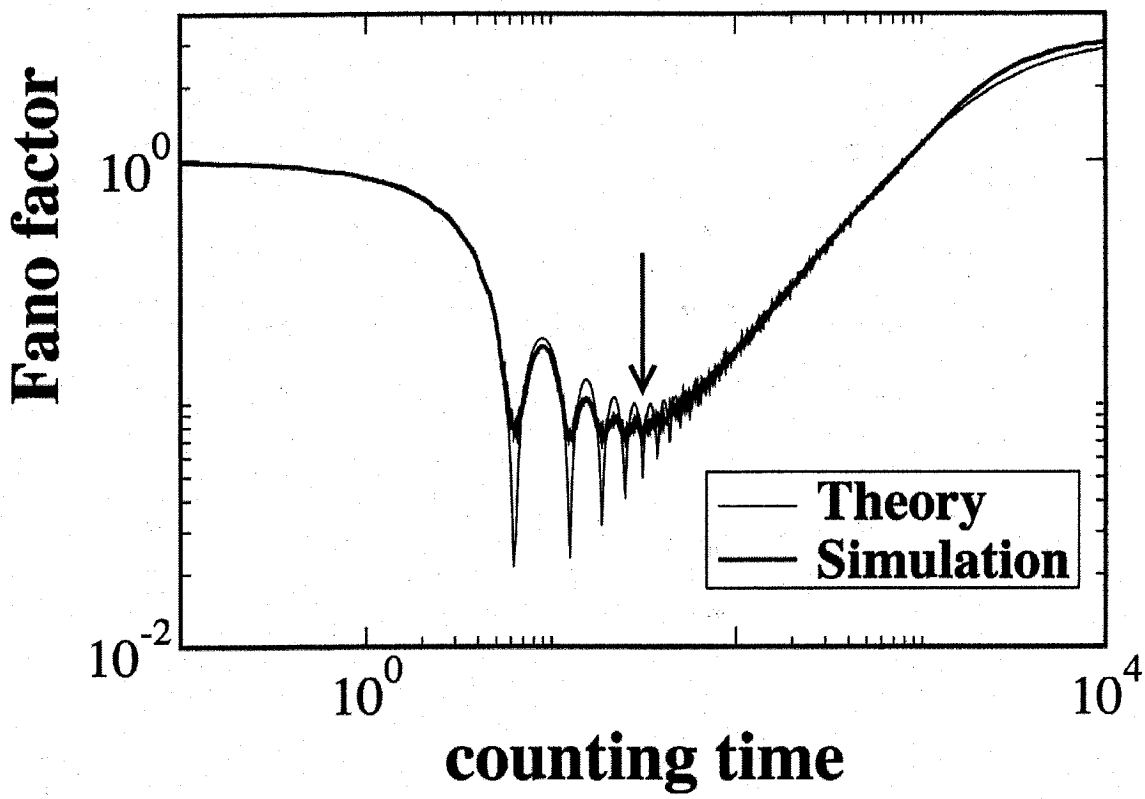

Figure 2-8. Comparison of the numerically obtained Fano factor along with the complete short- and long-time theoretical Fano factor from Eqs. (2.15) and (2.21) for $D = 10^{-2}$ and $\tau = 1000$. The arrow indicate the position of the minimum in the Fano factor as given by Eq. (2.23). The numerical data are the same as in Fig. 2-6.

$$\frac{d}{dt}\left(\frac{v_{th}}{4\mu t}+\frac{2D\tau}{v_{th}\mu}\left(1-\frac{\tau}{t}\left(1-e^{-t/\tau}\right)\right)\right)=0. \tag{2.22}$$

Since the position of the minimum is in general much smaller than τ we can expand the exponential in (2.22) to second order and differentiate. Solving the resulting equation yields the approximate position of the minimum of the Fano factor:

$$t_{\min}\simeq\frac{v_{th}}{2\sqrt{D}}. \tag{2.23}$$

Because we consider large correlation times, τ, the times at which the sum of $F_{\text{small}}(t)$ and $F_{\text{large}}(t)$ gives a minimum, occur only in the ballistic region of Brownian motion. Here, neither $F_{\text{small}}(t)$ nor $F_{\text{large}}(t)$ depend on τ. Hence, the minimum is determined by the only remaining parameter, namely the noise variance.

The positions of the minimum as given by (2.23) are indicated by arrows in Figs. 2-6 and 2-8, which agree very well with the apparent positions of the minimum given by the numerical simulations. We have thus shown that Eq. (2.1) exhibits a minimum in the Fano factor, and that the position of this minimum does not depend on the correlation time τ in this quasi-static approximation, but is entirely determined by the variance of the noise.

2.4 SPIKE TRAIN POWER SPECTRUM

We now derive correlation and spectral properties of the spike train generated by Eq. (2.1). The relation between the Fano factor and the spike auto-correlation function is given by (59)

$$F(t)=1+\frac{2}{f}\int_0^t ds\left(1-\frac{s}{t}\right)R_{xx}^{+}(s). \tag{2.24}$$

where $f = \mu / v_{th}$ is the mean firing rate of the point process and $R_{xx}^{+}(t)$ is the autocorrelation function of the spike train for $t > 0$ (not including the δ-function at the origin). We can invert this relation to find $R_{xx}^{+}(t)$ in terms of the Fano factor

$$R_{xx}^{+}(t) = \frac{u}{2v_{th}t}\frac{d}{dt}\left(t^2 \frac{d}{dt}F(t)\right). \tag{2.25}$$

The power spectrum can be calculated by the Fourier transform of the autocorrelation function

$$S(f) = \int_{-\infty}^{\infty} dt\, e^{i2\pi ft} R_{xx}(t). \tag{2.26}$$

Due to the linearity of the differential operator acting on the Fano factor in (2.25), the correlation can be expressed as a sum of two contributions: one coming from the small time approximation of the Fano factor and the other from the large time approximation. The discontinuities in the derivatives of the small time approximation make the integration of its corresponding correlation function analytically difficult. If we limit our focus to the correlation function at large times (coming from the large time Fano factor) we can describe the power spectrum at low frequencies. Substituting the expression for the large-time Fano factor, Eq. (2.15), will give us the autocorrelation function for large times:

$$R_{xx}^{+}(t) = \frac{D}{v_{th}^2} e^{-t/\tau}. \tag{2.27}$$

Inserting this expression into Eq. (2.26) gives us a Lorentzian spectrum:

$$S(f) = \frac{2D\tau}{v_{th}^2}\left(\frac{1}{1+(2\pi f\tau)^2}\right). \tag{2.28}$$

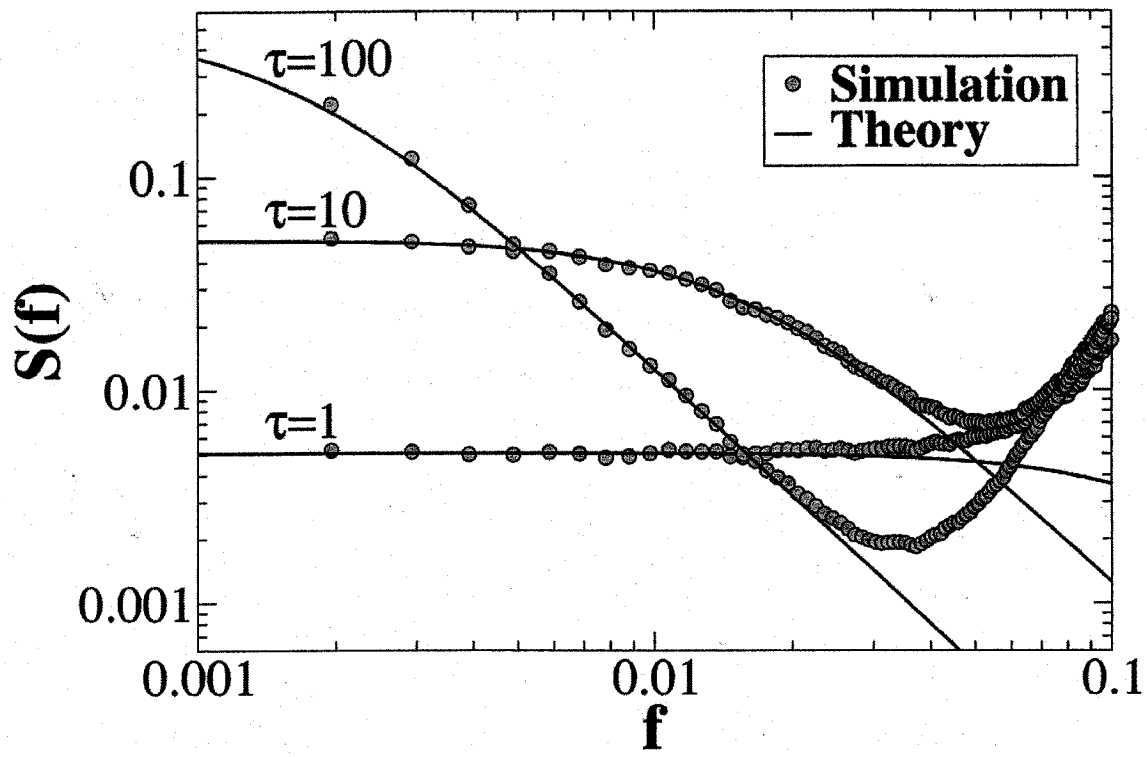

Figure 2-9. The low frequency power spectrum derived from the large time Fano factor approximation Eq. (2.15) compared with simulation results of Eq. (2.1). Results for three values of the noise correlation time are shown. The variance of the noise used in the simulations is $D = 0.1$. For reference, the frequency corresponding to the inverse ISI is $f = 0.159$.

Just as the spike-spike autocorrelation function displays properties of the input correlation, the low frequency power spectrum of the spike train has the same Lorentzian form as the OU input. Figure 2-9 shows the theoretical low frequency power spectral curves for several input noise correlation times compared with simulation results.

2.5 CONCLUSIONS

The effects of correlated noise have been of interest in the study of many stochastic systems (see eg. (51, 57, 65-70)). In this study, we have seen how long-range correlated noise can influence the spike train, ISI, and spike count statistics in a perfect integrate-and-fire model. Using a quasi-static approximation, analytical expressions for the ISI density were obtained. It was seen that the exponential correlations in the noise led to exponential correlations in both the ISI sequence and the spike train at long lags. As a consequence, the power spectrum of the spike train had a Lorentzian shape at low frequencies.

An expression for the Fano factor curve was then obtained. In particular, long range correlated noise was shown to increase the Fano factor at long time scales. Due to the finite correlation time used in the OU process, the Fano factor eventually saturates to a finite value. Such a saturation has been observed experimentally (17). An interesting finding of our study is the fact that a minimum in spike train variability as measured by the Fano factor can be obtained in this simple model. While the perfect integrate-and-fire neuron model used here as no explicit absolute refractory period there is a relative refractory period that arises due to the small noise and the fact that it takes a finite time (on the order of the average ISI) for the voltage to reach threshold from the reset value. It

is the interaction between this refractoriness, which decreases the Fano factor for small times, and the long-range correlated noise that will increase it for large times that causes the minimum.

It was shown that synaptic vesicle release observed in *Xenopus* neuromuscular junctions and in rat hippocampal synapses displayed long-range correlations (71). Our slow noise could thus model the synaptic current fluctuations received by a neuron. The Fano factor minimum has been observed in experimental data in both auditory fibers (54, 55) and weakly electric fish electroreceptors (57). Our study thus suggests that the Fano factor increase, and consequently the minimum, observed in many neurons (54, 72-76) could be due to long range correlations in the neurotransmitter secretion rate.

There is much speculation as to the significance of a minimum in spike train variability (56, 57, 64). For weakly electric fish electroreceptors, the time scale at which the minimum occurred matched the observed time scale at which these fish capture prey (77), giving a behavioral relevance to this minimum. It can be shown that the discriminability, d, between spike counts arising from distinct signal distributions is inversely proportional to $\left(F(t)/t\right)^{1/2}$ (56, 64); this latter quantity is also the relative error of an observed spike count. Figure 2-10 shows the relative spike count error, $F(t)/t$, as a function of counting time, t, for a single value of τ and two different noise intensities. The minimum of the Fano factors from Eq. (2.23) indicates the beginning of a plateau in the relative error. It is apparent that by increasing the counting time, while on the plateau, there is little improvement in the accuracy of spike count estimation. However, the relative error can be reduced to arbitrarily small values by taking increasing counting

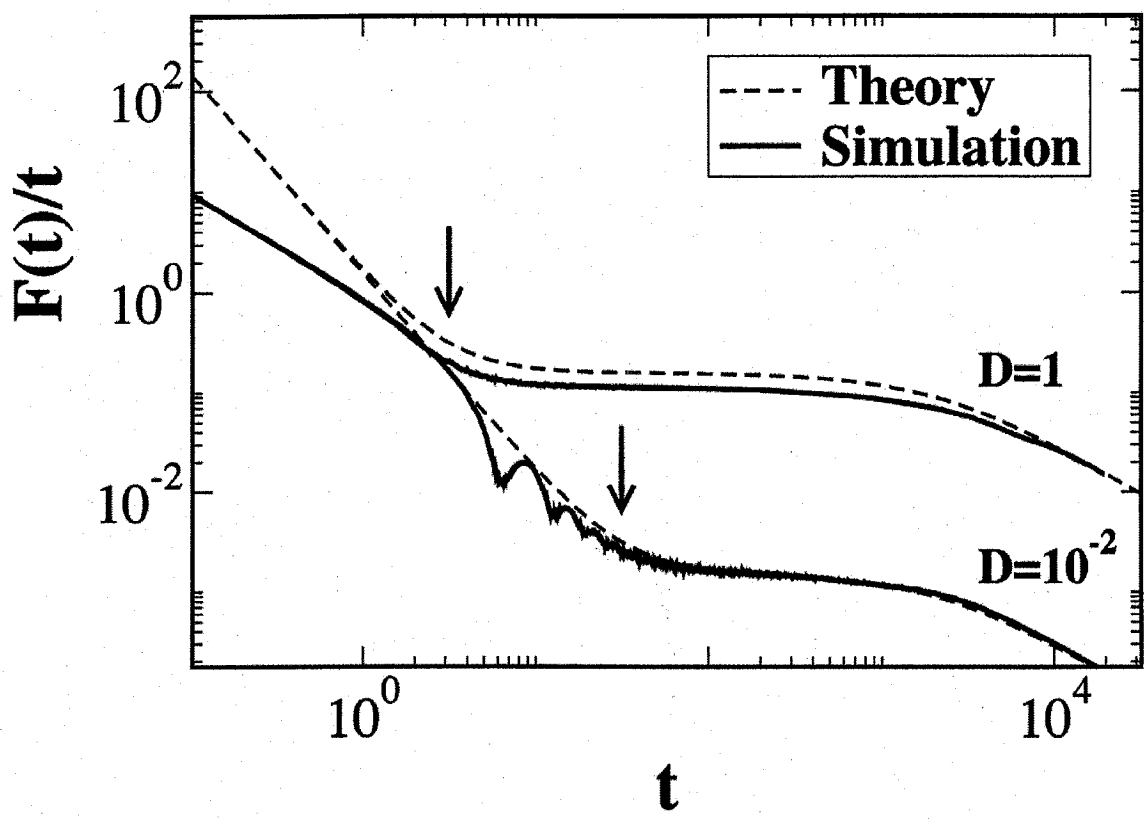

Figure 2-10. The relative spike count error, $F(t)/t$, as a function of counting time. The simulation results from integrating Eq. (2.1) are compared with the theory from the full range Fano factor approximation, $F_{\text{small}}(t)+F_{\text{large}}(t)$, where $F_{\text{large}}(t)$ is given by Eq. (2.15) and $F_{\text{small}}(t)$ is given by the envelope approximation $v_{th}/4\mu t$. Results are shown for $\tau=1000$ and for two different values of noise, $D=0.01$ and $D=1$. The arrows indicate the onset of the plateau region as given by Eq. (2.23). In each case the plateau persists until about the correlation time τ. While on the plateau there is very little change in the relative spike count error.

times greater than the correlation time of the OU process, τ. A sensory system using observed spike count to determine the presence or absence of prey would encounter the problem of having to wait long periods of time for the lowest possible spike count relative error. By the time a decision is made on the presence or absence of prey, any action based on that decision would be irrelevant, as the prey would have escaped in the meantime. The Fano factor might already implicitly factor in the cost of waiting too long. It is proportional to the relative error squared multiplied by counting time. The rise due to the factor of counting time implicitly accounts for the cost of indecision. If the Fano factor were actually an inverse measure of the benefit from the most accurate estimation in the shortest possible time, then its minimum would be the optimal time on which to perform computations used for signal detection, as has been observed experimentally in electric fish electroreceptors (57, 77).

An accurate electroreceptor model (78) driven by long-range correlated noise and periodic forcing was shown to reproduce this observed minimum (56). This result was later reproduced in a simpler leaky integrate-and-fire model with dynamic threshold (64) driven by both white and correlated noises without periodic forcing. In that study, negative ISI correlations, present due to a dynamic threshold (79), further decreased the Fano factor, from the value obtained with a renewal process, while the positive ISI correlations due to the slow noise increased it, giving rise to a minimum where signal detection with respect to an equivalent renewal process was greatest (64). Here we have found that the simple generic perfect integrate-and-fire driven by long-range correlated noise is sufficient to observe the Fano minimum. In particular, the counting time at which the minimum occurred varies with noise intensity, possibly explaining the experimentally

observed variability in the position of the minimum in weakly electric fish electroreceptors (57). While the minimum arising from the perfect integrate-and-fire neuron is not as pronounced as that from the LIFDT it is perhaps a less restrictive model. Because of this it may be useful for the phenomenological description of the Fano factor and its minimum, and thus signal detection time scales in various sensory system experiments.

CHAPTER 3: SYNAPTIC PLASTICITY AS A TEMPORAL FILTER IN DIFFERENT FIRING REGIMES

3.1 INTRODUCTION

Sensory systems detect and acquire information about the environment; this information is "processed" and relayed through successive stages up to higher brain centres where it is used to form perceptions, store memories or guide behaviour, among other things. Plasticity, which is the process by which the synaptic connection strength between neurons is modified based on their history of activity, has long been thought to be important in these cognitive/computational tasks.

It has been previously suggested that plasticity can play a role in neural dynamics other than as a substrate for memory storage [for comprehensive reviews see refs (32, 80)]. Synaptic depression has been proposed as a mechanism of adaptive gain control so that cortical neurons can respond in a invariant fashion to relative changes in presynaptic firing rates over a broad range of absolute firing rates (81). Activity dependent, or "plastic", synapses have been shown to enhance information transfer when compared to the case of activity independent synaptic transmission (33, 82), even in the paradoxical case where the synapses are depressing (83, 84). In addition to these roles it has recently been suggested that plasticity can act as a temporal filter, processing information streams to higher brain centres (85, 86). The prevailing belief is that depression (i.e. weakening synaptic strength with repeated activity) acts as a lowpass filter of time-varying signals and that facilitation (i.e. strengthening synaptic strength with repeated activity) acts as a highpass filter. Indeed this association is intuitive and it has been shown in sensory neurons that transmission of bursts events (high frequency spikes) is enhanced by facilitation and that transmission of single spike events are not affected by depression (12). This is specific to a neural spiking "code" whereby an oscillatory signal is

represented by a spike train firing at the same frequency of oscillation, namely that high (low) frequency signals are coded for by high (low) frequency spike discharge. The goal of this work is to expand this description to more general forms of spike train encoding and describe the overall filtering properties based on pre-synaptic inter-spike interval (ISI) statistics. We thus make the connection from sensory inputs to presynaptic neuron dynamics and resultant ISI statistics through to postsynaptic plasticity to form a generalized description of synaptic temporal filtering.

It was found (87) that sensory neurons, in a species of weakly electric fish, coded for oscillatory inputs by spiking once per cycle of oscillation. This is illustrated in Fig. 3-1 A where a representative high or low frequency signal is shown with their corresponding resultant spike train above. Plasticity was observed at the synapses that these neurons connect to; it was able to have long lasting cumulative effects in the case of high frequency firing. Facilitation thus enhances the post-synaptic current (PSC) resulting from high frequency events, acting as a highpass filter. Similarly, depression suppresses the current in the case of high frequency events, thus acting as a lowpass filter.

We can see for the rate-coded cases, Figs. 3-1 A, that the spiking frequency conveys the signal of interest. Both of these ISI sequences are very regular (i.e. low sequential interval variation) and have serial correlations only through their regularity. In this case it is expected that depression would filter the high frequency signal due to its short mean ISI and pass the low frequency signal through due to its long mean ISI, and vise versa for facilitation. The ISI sequences shown in the rate modulation case, Figs. 3-1 B, have the same mean ISI and so any differential effects of plasticity will not depend on the mean ISI. What is different between these two cases is the serial

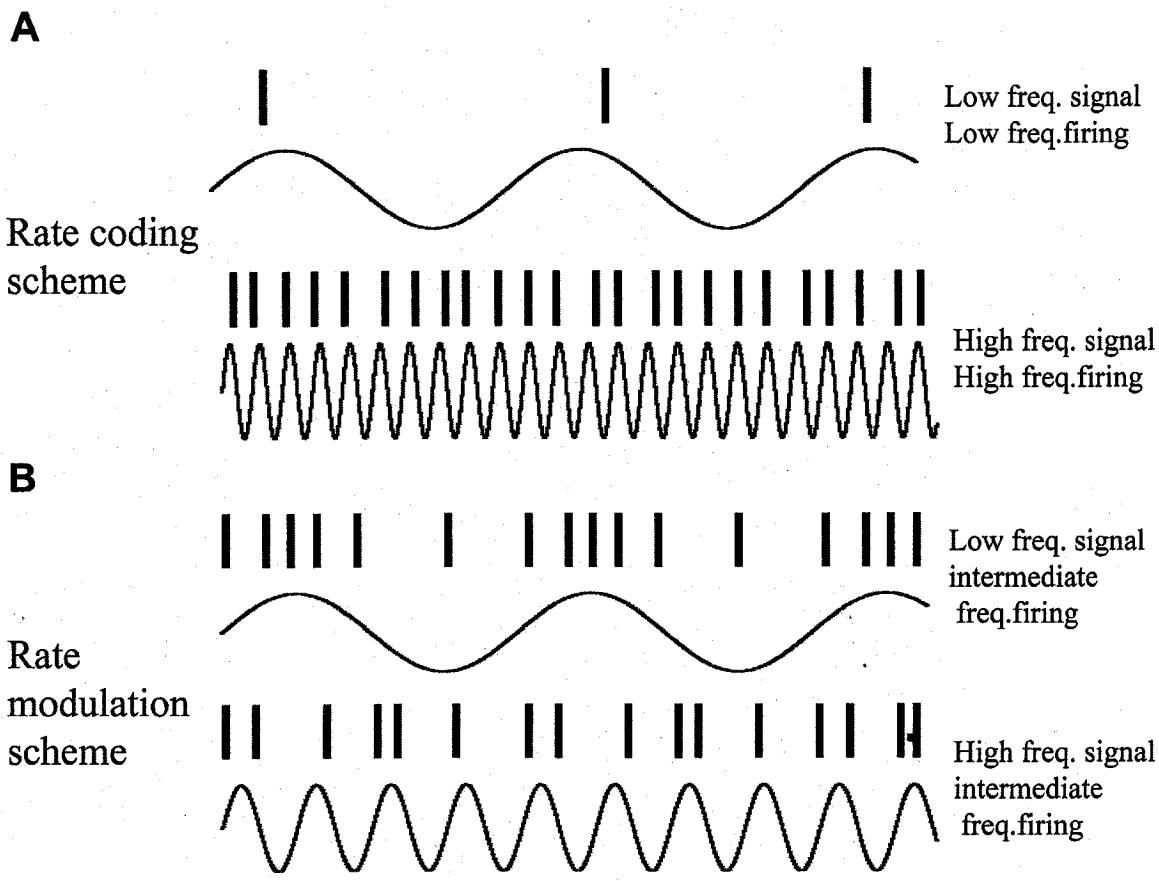

Figure 3-1. The different ways of coding for frequency content of input signals corresponds to different regimes of ISI statistics. In **A** the frequency of the input signal is conveyed through the mean firing rate of the encoding cell. The small ISIs of the high frequency coded signal will evoke a strong synaptic response compared to the long ISIs of the low frequency coded signal. In **B** the neurons have the same mean firing rate and yet are coding for different frequency inputs through modulations of the instantaneous firing rate. The long lasting positive correlations of the low frequency coded signal will evoke a strong synaptic response (in the case of either depression or facilitation) compared to the negative correlations of the high frequency coded signal.

correlations that the signals induce in the ISI sequences: the longer lasting positive correlations in the ISI sequence coding the low frequency result in subsequences of ISIs shorter than the mean. These subsequences of above, or below, average ISIs will increase or decrease the plasticity in a correlated manner. This signal will be suppressed or enhanced if the form of postsynaptic plasticity is depression or facilitation, respectively. This leads to the hypothesis that the roles of depression and facilitation as temporal filters can be switched under the right coding conditions, and given a fixed mean and variance of the ISI probability density; it is the serial correlations in the input ISI sequence that will determine the strength of the consequent filtering.

Here we present a simple linear model for synaptic plasticity and then show simulation results confirming the proposed roles of plasticity for both rate and modulation coded single harmonic signals. We then develop an analytic description of the role of ISI statistics in these filtering schemes. We then go on to show how the PSC resulting from our linear model responds to broadband inputs.

3.2 ISI STATISTICS AND POST SYNAPTIC PLASTICITY

A simple description of a post-synaptic current (PSC) generated from a single pre-synaptic spike is the "alpha function", $g(t)$. It has the form:

$$g(t) = \alpha^2 t e^{-\alpha t} \tag{3.1}$$

The parameter α is the inverse timescale of both the rise and fall of the PSC, and the prefactor α^2 normalizes the area under the PSC to 1. The full PSC arising from a presynaptic spike train is the solution of the dynamical system:

$$\begin{aligned} \dot{g} &= h \\ \dot{h} &= -\alpha^2 g - 2\alpha h + \alpha^2 \sum_k \delta(t - t_k) \end{aligned} \tag{3.2}$$

where $\{t_k\}$ is the set of pre-synaptic spike times. This dynamics generates a continuous PSC comprised of a linear sum of single PSCs each with unit area. The effect of plasticity on the PSC can be implemented in a simple way by scaling the integral of the PSC by the value that a plasticity variable has at the time of PSC generation. Introducing the variable, a, we can scale the area of a single PSC by a factor $1+a$ so that the case $a=0$ corresponds to no plasticity, $a<0$ corresponds to synaptic depression, and the case $a>0$ corresponds to synaptic facilitation. This plasticity dependent single PSC scaling can be realized by the dynamics:

$$\begin{aligned} \dot{g} &= h \\ \dot{h} &= -\alpha^2 g - 2\alpha h + \alpha^2 (1+a) \sum_k \delta(t - t_k) \\ \tau_a \dot{a} &= -a + \varepsilon_a \sum_k \delta(t - t_k) \end{aligned} \tag{3.3}$$

where τ_a and ε_a are the timescale and strength, respectively, of the plasticity. $\varepsilon_a < 0$ (> 0) corresponds to the case of synaptic depression (facilitation). These synaptic dynamics are a simplification of more realistic synaptic dynamics. The linearity of the system, however, offers analytical tractability and offers a starting point which may help in understanding non-linear synaptic models (82, 88). The average PSC in the absence of plasticity can be found easily by applying Campbell's theorem (89):

$$\langle g(t) \rangle = v \int_0^\infty \alpha^2 t' e^{-\alpha t'} dt' = v \tag{3.4}$$

where v is the presynaptic firing rate and the argument of the integral is the alpha function. To see how plasticity scales the average PSC we must determine the average effect of the plasticity on the dynamics $(\dot{g},\dot{h})$. With non-zero plasticity the running PSC takes the form

$$g(t) = \sum_k (1+a_k)\alpha^2 (t-t_k) e^{-\alpha(t-t_k)} \tag{3.5}$$

where $\{a_k\}$ is the set of plasticity variables at the presynaptic spike times. Using Campbell's theorem the average PSC becomes

$$\langle g(t)\rangle = v\left(1+\langle a_k\rangle\right)\int_0^\infty \alpha^2 t' e^{-\alpha t'} dt' = v\left(1+\langle a_k\rangle\right). \tag{3.6}$$

The dynamics of eq. (3.3) can be driven by a spike train generated from a leaky integrate-and-fire (LIF) neural model (19). The LIF has the dynamics:

$$\frac{dv}{dt} = -\frac{v}{\tau} + \mu + \sqrt{2D}\xi(t) \tag{3.7}$$

where v is the membrane voltage, τ is the membrane time constant, μ is the input bias and D is the membrane noise intensity. The bias can be first set in such a way that the LIF neuron is subthreshold (excitable) so that spikes will only be evoked by time varying inputs. Figure 3-2 shows the average plasticity (filled circles) in the case where one cycle of a sinusoidal input evokes one spike, the 'rate-coding' scenario described above. There is a compounding effect when the frequency of sinusoidal input increases such that the activation of plasticity is larger for high frequency input. When the bias, μ, is increased to put the neuron in the superthreshold regime (i.e. spontaneously firing) we can give different frequency inputs that leave the average firing unchanged, but modulate the rate

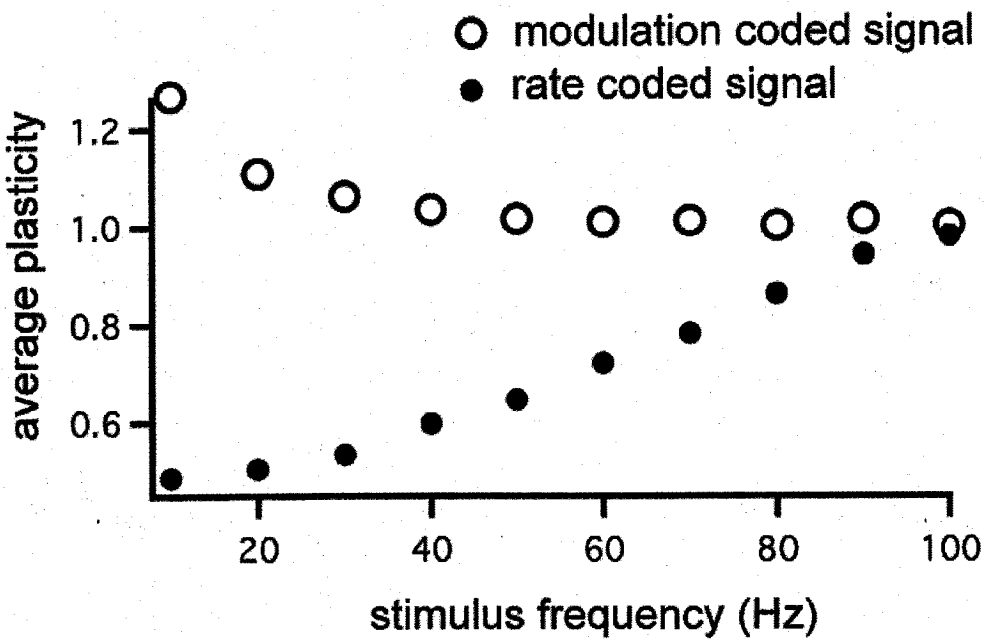

Figure 3-2: The average plasticity resulting from the dynamics of Eq. (3.3) being driven by an LIF neural model responding to sinusoidal inputs in the subthreshold (filled circles) and superthreshold (open circles) regimes. The subthreshold and superthreshold regimes correspond to the rate coding and modulation coding scenarios, respectively. Both the bias, μ, and the noise intensity, D, were tuned to keep the firing rate at 100 Hz for the superthreshold case, and locked to the stimulus frequency for the subthreshold case. In both cases the noise was kept at low values ($D \leq 10^{-4}$).

of spiking proportional to the input signal. This plasticity resulting from this form of driving is shown in Fig. 3-2 (open circles). We can see that the response, in terms of average plasticity, has the opposite dependence on input frequency; only in the case of low frequency inputs are there many successive short intervals between spikes allowing a build-up of plasticity.

3.2.1 PLASTICITY WITHOUT PRESYNAPTIC PLASTICITY

Given that the dynamics of (3.3) is linear we may attempt to formalize the dependence of the average plasticity on input ISI statistics, thus developing an analytic description. Eq. (3.3) shows that the value of a is incremented by an amount ε_a/τ_a every time a spike occurs. The contribution from the previous spike is $(\varepsilon_a/\tau_a)\exp\left[-(t_0-t_{-1})/\tau_a\right]$, and in general from the k^{th} preceding spike we have a contribution of $(\varepsilon_a/\tau_a)\exp\left[-(t_0-t_{-k})/\tau_a\right]$, where t_k denotes the spike time of the k^{th} preceding spike. Therefore the value of the plasticity at the current spike time, t_0 is given by

$$a(t_0)=\frac{\varepsilon_a}{\tau_a}\sum_{k=1}^{\infty}\exp\left[-\frac{(t_0-t_{-k})}{\tau_a}\right] \tag{3.8}$$

or introducing the notation $a_k=\exp\left[-(t_0-t_{-k})/\tau_a\right]$, the current plasticity value can be expressed as:

$$a(t_0)=\frac{\varepsilon_a}{\tau_a}\sum_{k=1}^{\infty}a_k \tag{3.9}$$

with $a_0=1$. Figure 3-3 illustrates the geometrical relationship between the set $\{a_k\}$ and the value $a(t_0)$. The arguments of the summation in Eq. (3.8) can be expressed in terms of the preceding ISI sequence, instead of the set of preceding spike times. The difference

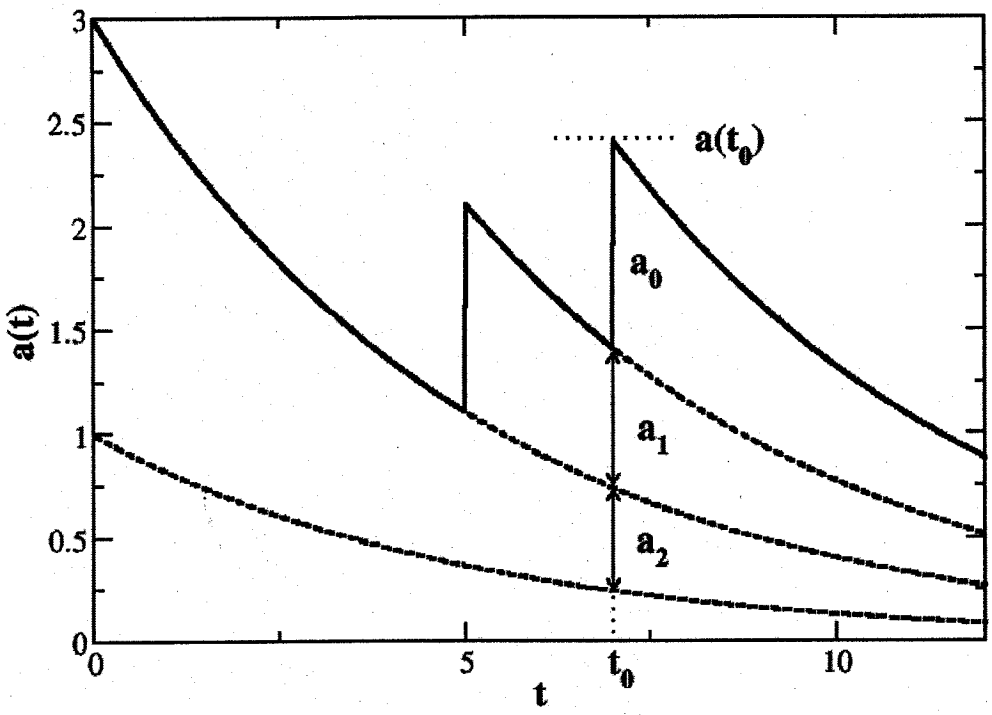

Figure 3-3: The value of the plasticity at the time of a spike, t_0 is a random variable whose value is a linear sum of exponential decays from all previous spike times. a_0 is the value of the instantaneous jump from the current spike time, and a_k is the contribution from the k^{th} previous spike.

between the current and the k^{th} preceding spike time is the sum of all intervening ISIs,

$$t_0 - t_{-k} = \sum_{j=1}^{k} I_j \tag{3.10}$$

where I_j denotes the ISI between the j and $(j-1)^{th}$ preceding spikes. The above sum of ISIs is also known as the k^{th} order ISI, which we shall label with T_k.

Before dealing with the complete sum in Eq. (3.8) we will show how the statistics of the first order ISI contribute to $a(t_0)$ and then extrapolate those results to contributions of higher order ISIs. The average contribution of the first order ISI to the synaptic variable a is

$$a_1 = \langle \exp(-T_1/\tau_a) \rangle = \langle \exp(-I_1/\tau_a) \rangle \tag{3.11}$$

If the CV of ISIs is small the spread of the ISI probability density about the mean value is small and a_1 can be well approximated as

$$a_1 = \langle \exp(-I_1/\tau_a) \rangle \simeq \exp(-\langle I_1 \rangle/\tau_a) \tag{3.12}$$

However if there is any significant spread of the ISI probability density about its mean, then values of I_1 smaller than $\langle I_1 \rangle$ will bias a_1 to values higher than $\exp(-\langle I_1 \rangle/\tau_a)$. This is a consequence of Jensen's inequality (90), namely that the expectation of a function of a random variable is greater or equal to that function of the expectation of the random variable if the function in question is convex (i.e. its second derivative is positive). The convex property is natural for any sort of decaying synaptic dynamics. This inequality is illustrated in Figure 3-4 comparing the mean values from a narrow versus a broad ISI probability density.

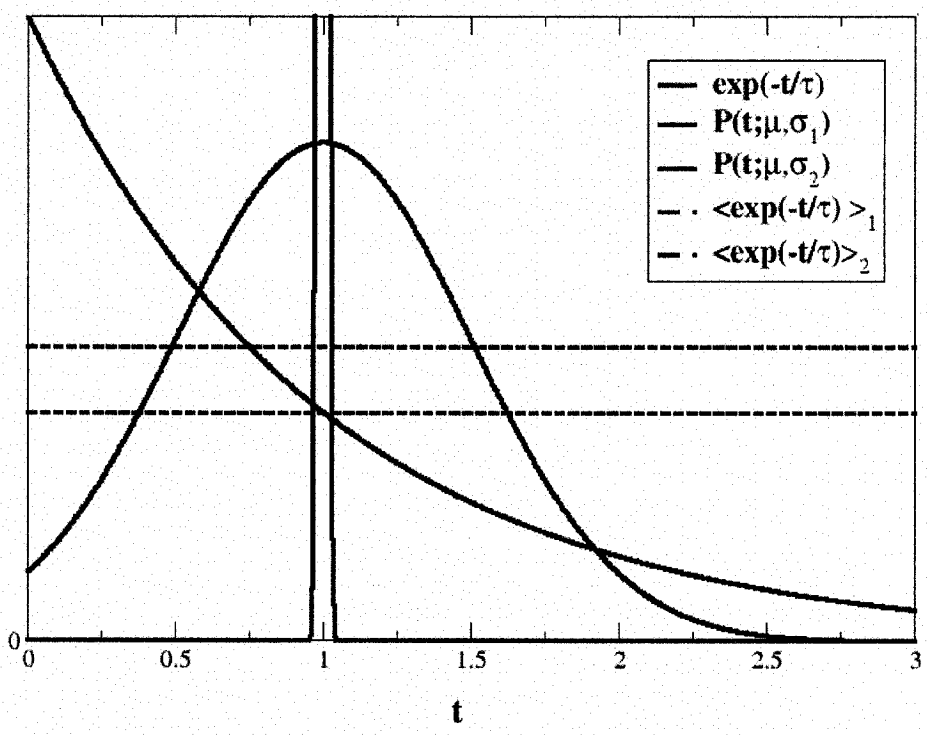

Figure 3-4. The expectation of a random variable, in this case the ISI, depends on the probability density. The black curve shows the exponential of an ISI, whose average value in the case of a narrow probability density (blue) is very close to the exponential of the mean ISI. Due to the convex nature of the exponential any probability density with moderate to large variance (green) will always increase the average value of the exponential. The blue and green dashed horizontal lines indicate the average values of the exponential for a narrow and abroad ISI probability density, respectively.

Even though ISI densities typically have complex functional forms (20, 91), in some cases approximating this density as a Gaussian is valid, particularly when a neuron is in the superthreshold firing regime (20, 91, 92). Making the ansatz that the ISI probability density is Gaussian:

$$P(I_1) \simeq \frac{e^{-(I_1-\mu)^2/2\sigma^2}}{\sqrt{2\pi\sigma^2}} \tag{3.13}$$

with mean $\mu = \langle I_1 \rangle$ and variance $\sigma^2 = \langle I_1^2 \rangle - \langle I_1 \rangle^2$, we can then obtain an analytic expression for a_1,

$$a_1 = \int_0^\infty I_1 P(I_1) dI_1 = \exp\left[-\frac{1}{\tau_a}\left(\mu - \frac{\sigma^2}{\tau_a}\right)\right] \tag{3.14}$$

We see from this closed form expression that increasing values of the ISI variance shift a_1 to larger values.

If the ISI sequence $\{I_k\}$ input to the synapse is uncorrelated then the probability density of the k^{th} order ISI density scales with k, and it is a Gaussian with $\mu_k = k\mu_1$, and $\sigma_k^2 = k\sigma_1^2$. This gives us

$$a_k = \int_0^\infty I_k P(I_k) dI_k = \exp\left[-\frac{1}{\tau_a}\left(k\mu - \frac{k\sigma^2}{\tau_a}\right)\right] \tag{3.15}$$

This allows us to obtain a simple closed form solution of the average synaptic variable a at the current spike time

$$\langle a(t_0)\rangle = \frac{\varepsilon_a}{\tau_a}\sum_{k=1}^{\infty}\left\langle \exp\left[-\frac{(t_0 - t_{-k})}{\tau_a}\right]\right\rangle = \frac{\varepsilon_a}{\tau_a}\sum_{k=1}^{\infty}\left\langle \exp\left[-\frac{T_k}{\tau_a}\right]\right\rangle$$
$$= \frac{\varepsilon_a}{\tau_a}\sum_{k=1}^{\infty}\exp\left[-\frac{k}{\tau_a}\left(\mu - \frac{\sigma^2}{\tau_a}\right)\right] = \frac{\varepsilon_a/\tau_a}{1-\exp\left[-\frac{1}{\tau_a}\left(\mu - \frac{\sigma^2}{\tau_a}\right)\right]} \qquad (3.16)$$

From this expression we can see that in order to have high levels of post-synaptic plasticity, i.e. large $\langle a(t_0)\rangle$, the condition: $(\mu - \sigma^2/\tau_a) \ll \tau_a$, must be met. This inequality can be achieved by decreasing the mean, μ, or increasing the variance, σ^2, of the ISI probability density. Otherwise the average contribution of plasticity to the PSC will be ε_a/τ_a independent of the presynaptic statistics.

3.2.2 PLASTICITY WITH PRESYNAPTIC PLASTICITY

To show the effect of ISI correlations, we will again use the approximation that the ISIs have Gaussian statistics. In this case the mean value of the k^{th} order ISI, T_i still has the same value, $\mu_k = k\mu$. However the variance of the k^{th} order ISI, σ_k^2, will be affected by correlations between ISIs. In the case of the second ISI we have (93)

$$\sigma_2^2 = 2\sigma^2 + 2\rho_1\sigma^2 = 2\sigma^2(1+\rho_1) \qquad (3.17)$$

where ρ_1 is the correlation coefficient between I_0 and I_1. For the general case of arbitrary order k, there will be contributions of the correlations between all pairs of ISIs between 0 and k. In this case we have

$$\sigma_k^2 = \sigma^2\sum_{j=0}^{k}(k-j)\rho_j \qquad (3.18)$$

where ρ_j are the serial correlation coefficients. In other words ρ_1 is the correlation coefficient between adjacent ISIs in the sequence $\{I_k\}$, ρ_2 is the correlation between all ISI pairs separated by one ISI in the sequence, and so on. The zeroeth order term $\rho_0 = 1$ is the correlation coefficient between an ISI and itself. With this correction to the variance of the ISI probability density for the case of ISI correlations Eq. (3.16) becomes

$$\langle a(t_0)\rangle = \frac{\varepsilon_a}{\tau_a}\sum_{k=1}^{\infty}\left\langle \exp\left[-\frac{T_k}{\tau_a}\right]\right\rangle = \frac{\varepsilon_a}{\tau_a}\sum_{k=1}^{\infty}\exp\left[-\frac{1}{\tau_a}\left(k\mu - \frac{\sigma^2}{\tau_a}\sum_{j=0}^{k}(k-j)\rho_j\right)\right] \quad (3.19)$$

This expression depends on the structure of the SCCs and in general cannot be further simplified analytically as in the case Eq. (3.16). However, we see that for positive correlations the average plasticity value will be larger than in the case of no ISI correlations. In the same way negatively correlated ISIs in the sequence $\{I_k\}$ will contribute in a way that decreases plasticity with respect to its baseline value.

3.3 SIMULATIONS OF SYNAPTIC PLASTICITY MODELS

To verify that ISI correlations can play a significant role at the post-synapse, we have done numerical simulations using two different simple neural models, each producing a different type of correlation structure, and fed their spike trains through the alpha function synaptic current model with plasticity, Eq. (3.3). Both are non-renewal models, the first one displaying long lasting positive correlations between ISIs, and the second one negative correlations between adjacent ISIs and zero correlations with all others.

We have shown, in chapter 2 of this thesis, that a simple integrate and fire (IF) neural model driven by bandlimited Gaussian distributed noise will have positively correlated ISIs sharing approximately the same exponentially decaying correlation structure with the

input (91). An ISI sequence from this model was generated, and for comparison, to confirm the role of correlations, a second ISI sequence was generated in which the order of ISIs was randomly shuffled, thus removing all sequential correlations. Both sequences were fed into the synaptic dynamics of equation (3.3) and the resulting post-synaptic current was temporally averaged after all transients died out. The comparison of a spike train and its corresponding shuffled surrogate should isolate the effects of correlations as the other primary ISI statistics, mean and variance, are unchanged by this operation. In the case of depression the results are displayed in Fig. 3-5, where for both ISI sequences the average PSC is plotted versus synaptic timescale. The units of the PSC are non-dimensionalized so that a value of one corresponds to the case of no plasticity. The solid curve in Fig. 3-5 shows the PSC from the original spike train, while the dotted curve shows that resulting from the shuffled presynaptic ISI sequence. We can see that the average PSC is lower for the original spike train as predicted by Eq. (3.19) in the case of depression for all synaptic timescales. The dashed curve shows the relative difference between these two PSCs and it can be seen that the position of the minima in PSC for both spike trains also corresponds to the maximal relative differences in the PSCs. When the plasticity timescale is zero there is no difference between these two cases as the plasticity decays much faster than the average ISI. As the timescale becomes arbitrarily large these two curves also converge since the synaptic variable just becomes a constant, independent of the correlations in presynaptic ISI sequence. In this limit the only factor determining the average PSC level is the mean ISI, μ.

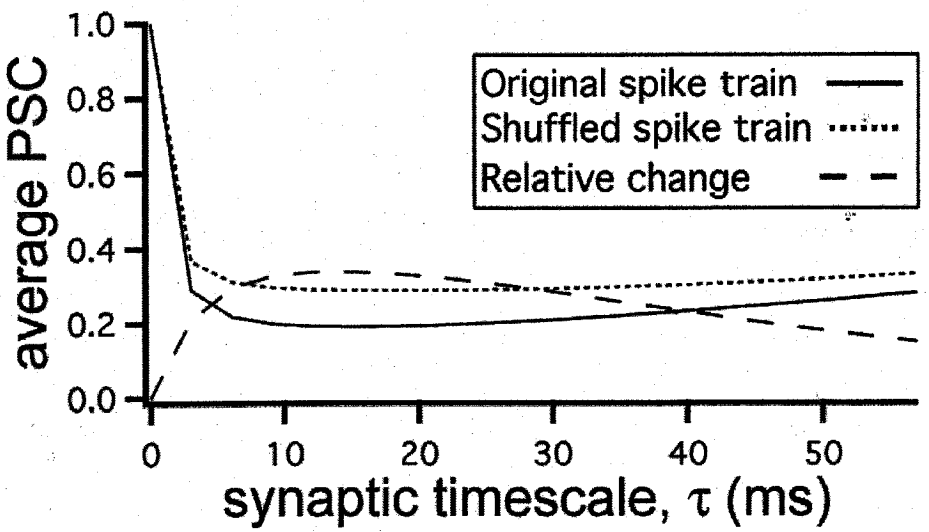

Figure 3-5. Simulation results for the mean level of the PSC from a presynaptic neural model with positive correlations. The solid line shows the average PSC as a function of synapse timescale when the presynaptic correlations are left intact. When spike train shuffling removes the presynaptic correlations, the average PSC is closer to its baseline value (dotted line). The dashed line shows the relative change between the two cases.

Another form of ISI correlation observed in primary sensory neurons (56) consists of a negative correlation at lag zero and no correlations for all other lags. This form of correlation arises from a dynamic spike threshold and has been shown to increase information transfer at low frequencies (94, 95). A simple phenomenological model reproducing these ISI statistics consists of a linearly increasing voltage, with rate μ, that generates spikes when a uniformly distributed random threshold, $\theta \in [\theta_0 - D, \theta_0 + D]$, is reached. The voltage is then reset by a fixed decrement, θ_0. To test the impact that this form of correlation, fed into plastic synapses, has on the PSC we drove the dynamics in Eq. (3.3) with spike trains generated by the dynamic threshold model as well as with surrogate spike trains with their intervals shuffled to remove correlations. We would expect that the negative ISI correlations would cause a decrease in the k^{th} order ISI variance and that the average plasticity due the original spike train would be less than for the shuffled spike train. The results are shown in Figure 3-6 where the average PSC, as a function of synaptic timescale, τ_a, is plotted for the original spike train (solid line) and the shuffled spike train (dotted line), as well as their relative change (dashed line). It can be immediately seen that there is very little difference between the cases of shuffled and unshuffled spike trains. The parameter space was thoroughly searched and there was no regime where a significant difference in the average PSC was noticed. The reason is that the impact of ISIs further in the past are lost because the only non-zero SCC in this model is at lag one. The variance of the k^{th} order ISI density still grows linearly, whereas if we had a model that could generate long-range negative correlations (an unphysical scenario

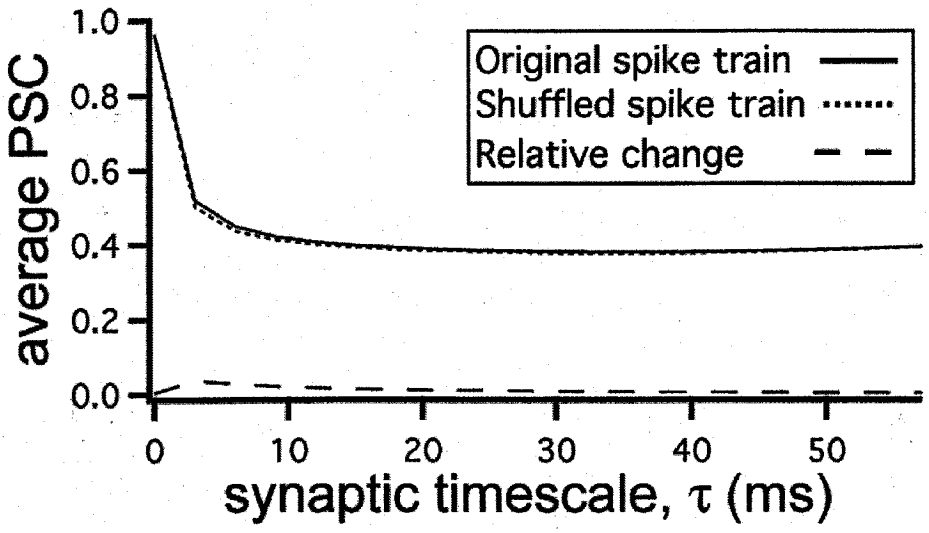

Figure 3-6. Simulation results for the mean level of the PSC from a presynaptic neural model with negative correlations. The solid line shows the average PSC as a function of synapse timescale when the presynaptic correlations are left intact. When spike train shuffling removes the presynaptic correlations, the average PSC is closer to its baseline value (dotted line). The dashed line shows the relative change between the two cases.

unless interspersed with positive correlations) the variance of the k^{th} order ISI density would grow sub-linearly and then be able to impose a significant reduction of plasticity.

3.4 TEMPORAL FILTERING OF BROADBAND NOISE BY PLASTICITY

In addition to the mean level of the PSC, we studied how the correlation structure of the presynaptic ISI sequence affects the transmission of temporal information at the plastic synapse. This was achieved by calculating the coherence between the presynaptic spike train and the postsynaptic current (PSC) to see whether or not the conventional idea of depression as a lowpass filter and facilitation as a highpass filter holds. The coherence between two stationary, time-varying signals, $x(t)$ and $y(t)$, is defined as

$$C_{xy}(f) = \frac{|S_{xy}(f)|^2}{S_{xx}(f)S_{yy}(f)} \tag{3.20}$$

where $S_{xy}(f)$ is the cross-spectral density between $x(t)$ and $y(t)$ in the frequency domain, and $S_{xx}(f)$ is the auto-spectral density of $x(t)$ and likewise for $y(t)$. This measure of information transfer can obtain values between zero and one, with zero indicating no linear correlations between the two signals at a certain frequency and a value of one indicating perfect linear correlation.

Figure 3-7 shows the coherence between presynaptic spike train and PSC using the neural model with long-range positive correlations described above in the case where the plasticity is depression. The coherences from 10 realizations of 10 s long trials were averaged to reduce statistical fluctuations. The dotted curve shows the resulting coherence using the original spike train and the solid curve shows the coherence using the corresponding shuffled spike train. In the lower frequency range (<50 Hz) we can see

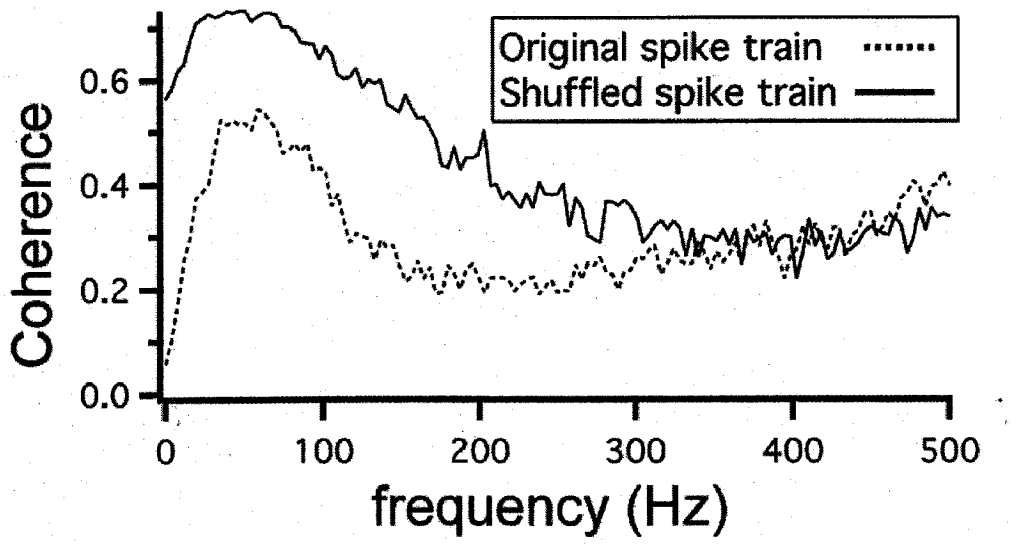

Figure 3-7. The coherence between pre- and postsynaptic neural spike trains when the intervening plasticity is depression. The dotted line shows the coherence for the original pre-synaptic spike train and the solid line for its corresponding shuffled surrogate. The original spike train coherence is highpass with respect to the shuffled spike train whose correlations have been removed. The parameters used in the model of Eq. (3.3) are $\alpha = 1\,\text{ms}$, $\tau_a = 15\,\text{ms}$ and $\varepsilon_a = -0.8$.

that the coherence with the unshuffled spike train drops off faster as frequency goes to zero. This result confirms that for superthreshold presynaptic spike trains synaptic depression acts as a highpass temporal filter. Figure 3-9 shows the difference of the coherences in Fig. 3-7 for the depressing synapses (solid line). This difference is representative of the extra information filtered out at the synapse. In this case there is more information filtered out in the low frequency range (<50 Hz) as is the case for a highpass filter.

Figure 3-8 shows the coherence between presynaptic spike train and PSC using the neural model with long-range positive correlations described above in the case where the plasticity is facilitation. The dotted curve shows the resulting coherence using the original spike train and the solid curve shows the coherence using the corresponding shuffled spike train. With increasing frequency we can see that the coherence with the unshuffled spike train drops off faster. This result confirms that in the case of superthreshold spike trains the role of synaptic facilitation is as a lowpass temporal filter. Figure 3-9 shows the difference of the coherences in Fig. 3-8 for the facilitating synapses (dotted line). This difference is representative of the extra information filtered out at the synapse. In this case there is more information filtered out in the high frequency range (>50 Hz) as is the case for a lowpass filter.

The same protocol was applied with negative correlations. We were interested to see if there were differences in the filtering properties despite the fact that the mean level of plasticity was practically unchanged by shuffling the pre-synaptic spike train. The results (not shown) were inconclusive as the noise shaping effect (94, 96)

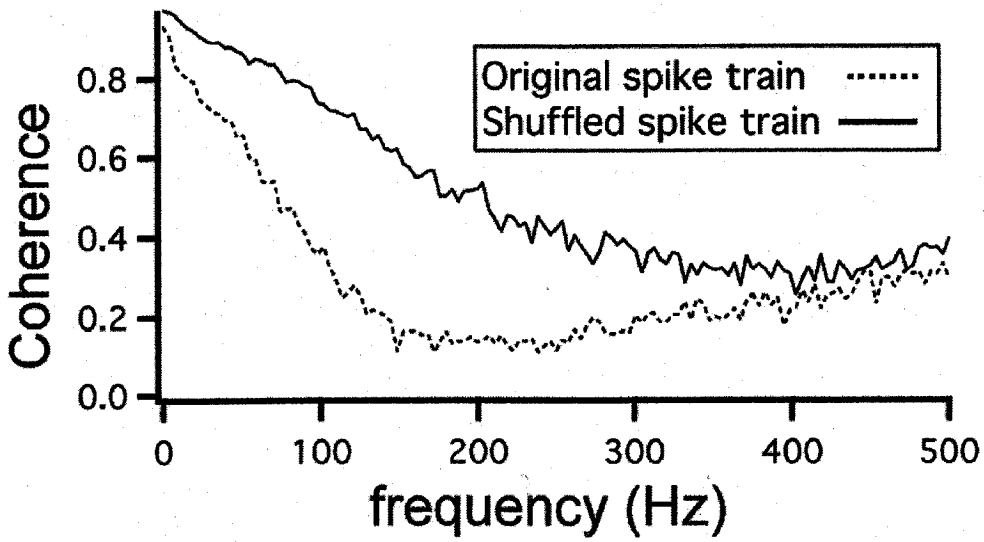

Figure 3-8. The coherence between pre- and postsynaptic neural spike trains when the intervening plasticity is facilitation. The dotted line shows the coherence for the original pre-synaptic spike train and the solid line for its corresponding shuffled surrogate. The original spike train coherence is lowpass with respect to the shuffled spike train whose correlations have been removed. The parameters used in the model of Eq. (3.3) are $\alpha = 1\,\text{ms}$, $\tau_a = 15\,\text{ms}$ and $\varepsilon_a = 2.0$.

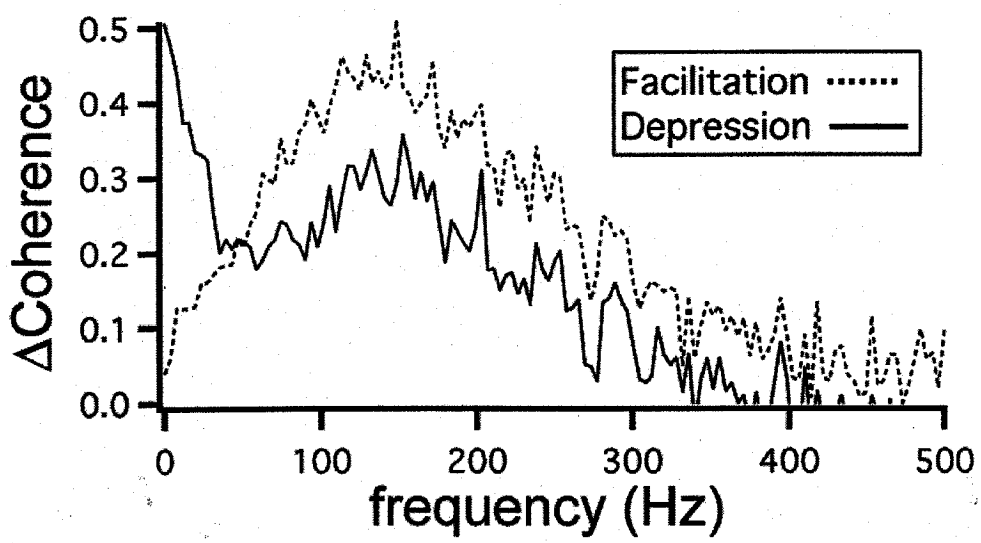

Figure 3-9. The difference in coherence of the original spike trains in Figs. 3-7 and 3-8 and their respective shuffled surrogate spike trains. This solid line is representative of the extra information filtered out by depressing synapses; the extra information filtered at low frequencies indicates a highpass filter. This dotted line is representative of the extra information filtered out by facilitating synapses; the extra information filtered at higher frequencies indicates a lowpass filter.

seen in neurons with negative ISI correlations greatly reduces power at low frequencies (94) and interferes with any type of filtering going on at the synapse.

3.5 PLASTICITY IN BIAS CODING VERSUS NOISE CODING

As shown in the previous section, the time averaged plasticity contributing to the post-synaptic current depends on the relationship between the ISI statistics and the synaptic timescale; namely significant contributions from synaptic plasticity can occur only if $(\mu - \sigma^2/\tau_a) \ll \tau_a$. It was also shown that ISI correlations are important in determining the effect of plasticity on the PSC and the filtering properties of the post-synaptic neuron. Positive ISI correlations increase the magnitude of plasticity while negative ISI correlations contribute to a decrease.

It is interesting to consider how choosing different models and how placing them in different contexts lead to ISI sequences with different correlation structure. However, here we will only study a single neural model and place it in two different contexts to show how different levels of average post-synaptic plasticity arise. It will then become apparent how these two different contexts are relevant for simple neural coding tasks that this model may represent.

It was previously shown how the statistics of a simple neural model were modified by introducing an input with long lasting correlations in the time domain (91). In that case the input was given as a slowly varying current injection. The dynamics of that model is described by:

$$\begin{aligned} \dot{v}(t) &= \mu + \eta(t) \\ \tau\dot{\eta}(t) &= -\eta(t) + \sqrt{2D\tau}\xi(t) \end{aligned} \tag{3.21}$$

supplemented with the condition that once the membrane voltage reaches a threshold level, v_T, it is instantaneously reset to a reference value, v_R. Here, μ is the mean input current, η is the slow noise process, τ and D are the timescale and variance of this noise, respectively. With this model it was shown that the serial correlation coefficients (SCCs) of the ISI sequence, for small noise variance, take the form

$$\rho_j \simeq \exp\left[-j\frac{\langle I\rangle}{\tau}\right] \tag{3.22}$$

The small variance condition was used to match the analytical results to simulations, however, the decaying exponential form still holds for larger noise variance but scale with a constant of proportionality less than one. The work in chapter 2 of this thesis was done in the spirit of determining the type of statistical context where a neuron with a correlated intrinsic noise source could process signals. Instead of η being an intrinsic noise source, it could also be treated as a signal and add an uncorrelated intrinsic noise into the neural dynamics, i.e.,

$$\dot{v} = \mu + \eta + \sqrt{2D_0}\xi \tag{3.23}$$

With this description the intrinsic background noise should decrease the absolute value of the SCCs, but the relative slowly decaying form will still hold.

With the results of the previous section we can see that the slowly decaying positive correlations arising from the slow fluctuations in the bias current of the model will, on average, cause a strong buildup of the synaptic plasticity, primarily due to long sequences of successive short ISIs. If the plasticity variable is, for example, depression ($\varepsilon_a < 0$) then the average value of the postsynaptic current that this neural model causes will be

strongly attenuated, and the synapse will also be lowpass. If the purpose of this neuron is to transmit, an accuratea copy of this signal to the post-synaptic cell then the ISI correlations caused by the signal would be detrimental.

Instead of giving the time-varying signal, η, into the neural model as a bias current, we can deliver it as a time varying component of the noise intensity,

$$\dot{v} = \mu + \sqrt{2(D_0 + \eta)}\xi_i \tag{3.24}$$

This may be realized in a biophysically plausible manner by having populations of Poisson spike trains whose mean rate varies with η and whose inputs onto the neuron have balanced inhibition and excitation. This type of signal transmission in single neurons has been shown to allow fast transmission of time varying signals between populations of neurons (97). It will be shown below that noise coding of slow signals will allow the signal to be passed through a plastic synapse and escape the detrimental effects of plasticity.

In order to assess the benefit of noise coding on plasticity we must determine the form of the correlation that a noise-coded signal creates in the presynaptic spike train. Using the quasi-static noise approximation, presented in chapter 2, also see ref. (91), it was shown how the correlations in the driving Ornstein-Uhlenbeck process passed through to the ISI correlation. Using the conditional probability density in Eq. (2.6) the correlation between I_k and I_{k+l} becomes:

$$\begin{aligned}\langle I_k I_{k+l}\rangle &= \left\langle \frac{v_{th}^2}{(\mu+\eta_k)(\mu+\eta_{k+l})}\right\rangle \simeq \frac{v_{th}^2}{\mu^2}\left\langle \left(1-\frac{\eta_k}{\mu}\right)\left(1-\frac{\eta_{k+l}}{\mu}\right)\right\rangle \\ &\simeq \frac{v_{th}^2}{\mu^2}\left(1-2\frac{\langle\eta_k\rangle}{\mu}+\frac{\langle\eta_k\eta_{k+l}\rangle}{\mu^2}\right).\end{aligned} \tag{3.25}$$

The mean ISI can be calculated in the same using the conditional probability density, Eq. (2.6):

$$\langle I_k \rangle = \left\langle \frac{v_{th}}{\mu + \eta_k} \right\rangle \simeq \frac{v_{th}}{\mu}\left(1 - \frac{\langle \eta_k \rangle}{\mu}\right) \tag{3.26}$$

With the previous two results, we see that the serial covariance of the ISIs is the same as the covariance for the discretely sampled OU process

$$\langle I_k I_{k+l} \rangle - \langle I_k \rangle^2 = \langle \eta_k \eta_{k+l} \rangle - \langle \eta_k \rangle^2 \tag{3.27}$$

so that the serial correlation coefficients of the two random variables are the same:

$$C_{I_k}(l) = C_{\eta_k}(l) \tag{3.28}$$

as shown in chapter 2. For the noise-coded signal we can use the same quasi-static approximation to express I_k in terms of η_k. The difference now is that the mean is independent of the noise intensity in the perfect integrate-and-fire neuron giving:

$$\langle I_k I_{k+l} \rangle = \left\langle \frac{v_{th}^2}{\mu^2} \right\rangle = \frac{v_{th}^2}{\mu^2}. \tag{3.29}$$

From this it is easy to see that the serial correlations in the noise-coded case are zero, for all lags greater than or equal to one. This is only the case for the simple dynamics we have chosen, namely the perfect integrate and fire. The average firing rate does not depend on the driving noise intensity, and consequently neither does the mean ISI. For the case of a leaky integrate-and-fire model, the mean ISI does depend on the noise intensity, though not as strongly as it does on the driving bias. We would expect that for this model, the serial correlations induced by a slowly varying driving noise intensity would be non-zero, but much smaller than for the case of a slowly varying bias current.

3.6 DISCUSSION

Plasticity has been shown to play a role in temporal filtering of sensory stimuli, in the steady state. The prevailing belief is that the roles of depression and facilitation are as low and high pass filters respectively. We show here that these roles are dependent on the mode that the neuron is firing in, i.e. subthreshold or superthreshold. In the subthreshold case, when a single cycle of input generates approximately one spike, the signal is coded for by the rate of firing. In the superthreshold case, when the neuron is spontaneously active, the mean firing can remain unchanged while the temporal modulation of the firing rate tracks the input signal. We have presented a simple linear model for synaptic plasticity and then showed simulation and analytic results confirming the proposed roles of plasticity for both rate and modulation coded single harmonic signals, namely that in the modulation coded case the roles of depression and facilitation are reversed. These results should apply qualitatively to more detailed synaptic models containing nonlinearities. The analytics in the first half of this chapter will not be applicable to nonlinear models although the numerics, which followed should, as the essential element for this effect to occur is the statistics of the presynaptic neuron spike train.

CHAPTER 4: THE CELLULAR BASIS FOR PARALLEL NEURAL TRANSMISSION OF A HIGH-FREQUENCY STIMULUS AND ITS LOW-FREQUENCY ENVELOPE

4.0 ABSTRACT

Sensory stimuli often have rich temporal and spatial structure. One class of stimuli common to visual and auditory systems and, as we show, the electrosensory system, are signals that contain power in a narrow range of temporal (or spatial) frequencies. Characteristic of this class of signals is a slower variation in their amplitude, otherwise known as an envelope. There is evidence suggesting that, in visual cortex, both narrowband stimuli and their envelopes are coded for in separate and parallel streams. The implementation of this parallel transmission is not well understood at the cellular level. We have identified the cellular basis for the parallel transmission of signal and envelope in the electrosensory system: a two-cell network consisting of an interneuron connected to a pyramidal cell via a slow synapse. This circuit could, in principle, be implemented in auditory or visual cortex by the already identified biophysics of cortical interneurons.

4.1 INTRODUCTION

Narrowband signals (i.e., containing power in a narrow range of frequencies) are an important class of naturalistic stimuli for visual and auditory systems and have associated with them a stimulus envelope, a slow, time-varying contrast or modulation of a sinusoidal carrier arising naturally from, for example, interference between two or more sinusoidal oscillations with similar frequencies. Amplitude modulated signals have no power at the frequencies of the modulation, but instead have power centered on the carrier frequency with side-bands whose structure depends on the frequency content of the modulation, or envelope (89). Since the actual signal contains no power at the

envelope frequencies a system that can extract information about the envelope must utilize non-linear processing. An asymmetry in the single neuron input-output transfer, such as rectification (89), will generate power at the envelope frequencies (98, 99). Recent studies show that visual cortical neurons in cat respond to both low spatial frequency signals and to the low frequency spatial envelopes of high frequency signals, and also suggest that information about stimuli and their envelopes take separate and mutually exclusive, linear and non-linear pathways to reach these cortical neurons (48, 100-106). The cellular and network basis of these parallel cortical computations is not, however, understood.

A. leptorhynchus generates a sinusoidal electric organ discharge (EOD) that produces an electric field around its body. Recent field studies have shown that *A. leptorhynchus* and related species forage in groups (107). Although individual *A. leptorhynchus* maintain a stable EOD frequency (108), the species has a frequency range of about 700-1000 Hz. Two fish with widely spaced EOD frequencies will generate a high frequency envelope of their EOD referred to as an amplitude modulation (AM) or beat. Additional fish can superimpose a slowly varying contrast on this high frequency AM (an envelope of the envelope of the EOD) (107) (Fig. 4-1 A). To avoid confusion we will henceforth refer to the AM of the EOD as the *stimulus*, and the modulation of the AM as the *envelope*. Thus envelopes are a natural component of the electrosensory environment of an aggregation of wave-type electric fish.

Electroreceptors (P-units) are sensitive to the AMs induced by conspecifics (communication signals) and project to the electrosensory lateral line lobe (ELL). Here

we study the response of ELL neurons to the envelope of these signals. We demonstrate that a two-cell network, consisting of: (a) a direct P-unit synaptic input to a pyramidal (projection) cell and (b) a high-frequency tuned interneuron projecting onto the pyramidal cell via slow GABA-B mediated inhibition, is responsible for parallel transmission of the AM stimulus (direct input) and the corresponding stimulus envelope (interneuron mediated input) in separate channels.

4.2 MATERIALS AND METHODS

Electrophysiological Recording. Data from 32 adult *A. leptorhynchus* are used in this study. For surgical exposure of the electrosensory lateral line lobe (ELL), fish were anesthetized (Tricane-S, Western Chemical Inc. Ferndale, WA). After surgery fish were immobilized (Pancuronium Bromide, Sabex, Bouchervillee, Quebec) and transferred into a tank (28^0c) where they were respired by a constant flow of oxygenated water through their mouth. Intracellular and extracellular recordings from ELL neurons and axons were routinely made with borosilicate microelectrodes (70-140 MΩ), filled with 3M KAc (intracellular) or tungsten wire electrodes (extracellular, TM33C10, WPI, Saratosa, FL); the recording electrodes were advanced into ELL with a piezoelectric microdrive (Inchworm, IW-711, Burleigh, Fishers, NY) in the ELL. Electroreceptor afferents (P-units), pyramidal cells, one class of ELL interneuron (ovoid cells) and feedback inputs to ELL were identified based on electrode depth, baseline discharge statistics and by responses to step changes in the EOD amplitude, sinusoidal and random EOD amplitude modulations; these responses are well characterized and successfully discriminate cell types (9, 109-111). Recorded signals were amplified (Axoprobe, Axon Intruments, Union

City, CA for intracellular, N=43, and for extracellular recording, N=9) and stored on a desktop personal computer. Analysis was performed offline using Matlab (Mathworks, Matick, MA) software. All experimental and surgical protocols were approved by the University of Ottawa Animal Care Committee.

The EOD unperturbed by the stimulus was recorded between the head and tail of the fish using two vertical carbon rods (11cm long, 8mm diameter). Two chloridized silver wires, insulted except at the tips and spaced 2 mm apart were placed approximately 1 mm away from, and at right angles to, the fish's body; these electrodes were used to record the stimulus induced EOD amplitude modulations.

The membrane potentials, the unperturbed EOD, the modulated EOD transverse to the fish and the attenuated stimulus were digitized at 20 kHz with a Multi-IO board (PCI-MIO-16E-4; National Instruments, Austin, TX) on an Intel Pentium IV 1.8 GHz Linux personal computer. Spike and EOD detection, stimulus generation and attenuation, preanalysis of the data were performed online during the experiment within Online Electrophysiology Laboratory (OEL) software (112).

Stimulation. Amplitude modulations of the EOD were created by sampling the head-tail carbon electrodes, multiplying this EOD with the desired modulation. This signal was delivered in phase with the fish's own EOD, via stimulation electrodes placed over the cell's receptive field center (local geometry) or across the fish's body (global geometry) as previously described (79, 113, 114). The output of the stimulation electrodes was attenuated so that, when combined with the fish's own EOD, the correct signal contrast was produced. The stimulation electrodes in global geometry consisted of two carbon

rods (20 cm long, 8 mm diameter) parallel to the rostral-caudal axis placed either side 10 cm away. In local stimulus geometry, two thin tungsten wires, insulated except at the tips, with a spacing of 2 mm were placed 5 mm away from the surface of the fish perpendicular to the body axis.

There were two classes of stimuli used: broadband and narrowband Gaussian distributed noise. Both were derived from Gaussian white noise by applying a low pass filter (100 Hz cutoff frequency) or a band pass filter (20 Hz bandwidth with center frequencies ranging from 30 Hz to 290 Hz), respectively. Narrowband signals are a convenient representation of the types of signals electric fish would see while aggregating with a population of conspecifics. Wave type weakly electric fish have a natural distribution of EOD frequencies (107). In a population of 3 or more the types of EOD modulations they would experience are neither broadband, nor pure tones, therefore we chose narrowband Gaussian noise as a mimic of this kind of electrosensory signal.

Extracting the stimulus envelope. The Hilbert transform is a useful tool in the analysis of time-varying stationary signals with oscillatory components. A harmonic oscillation, $x(t)$, can be represented geometrically as a limit cycle in the complex plane by creating the analytic signal, $z(t) = x(t) + iy(t)$, whose imaginary part is composed of the real frequency components phase shifted by 90 degrees, i.e. $y(t) = H[x](t)$, where H is the Hilbert transform:

$$H[x](t) = \frac{1}{\pi} P \int_{-\infty}^{\infty} \frac{x(\tau)}{t-\tau} d\tau . \qquad (4.1)$$

In the case of the narrowband signals that we used the radial component of the corresponding analytic signal has an intuitive interpretation. The radial component,

$$A(t)=\sqrt{x^2(t)+y^2(t)} \tag{4.2}$$

represents the instantaneous amplitude, or signal envelope, arising due to interference of spectral components of the signal having similar frequencies.

Data analysis. The coherence between two stationary signals, $x(t)$ and $y(t)$, is defined as:

$$C_{XY}(f)=\frac{|S_{XY}(f)|^2}{S_{XX}(f)S_{YY}(f)} \tag{4.3}$$

where $S_{XY}(f)$ is the cross-spectral density between x and y, and S_{XX} and S_{YY} are the auto-spectral densities of x and y respectively. It measures the correlations of phase and amplitude of oscillations between the two signals as a function of their frequency. The coherence gives a measure of the filtering properties of a transfer system if $x(t)$ and $y(t)$ refer to the input and output. We are interested in the response, $R(t)$, of a given neuron in the form of an action potential sequence, or spike train, to a given stimulus, $S(t)$, at the sensory periphery. The spike train response can be defined mathematically as a series of delta functions centered at the spike times: $R(t)=\sum_i \delta(t-t_i)$. We will use the notation $C_{SR}(f)$, or equivalently S-R coherence, to refer to the coherence between stimulus and response, in the form of a spike train. We also use the notation S-R coherence to denote the response between subthreshold membrane voltage and the stimulus, but we explicitly state this where used. The coherence between two responses to the same signal is denoted $C_{RR}(f)$, and in general the inequality $C_{SR}(f)\leq\sqrt{C_{RR}(f)}$ holds, so that the responses are at least linearly related to one another via the stimulus (47); the stimulus-response and

response-response coherence are lower (linear) and upper bounds respectively on the information that can be transmitted by a neuron about a signal (47). Throughout, we compare S-R coherence to the square root of R-R coherence but denote it as simply R-R coherence, for brevity. A more formal connection to mutual information has been established using these measures but will not be used here (46). The notation E-R coherence is used to represent the response of the spike train (or subthreshold voltage where stated) to the stimulus envelope calculated via the Hilbert transform. The subthreshold membrane voltage was obtained from the intracellular voltage recording by using a spike removal algorithm. This algorithm detected spikes by using voltage and voltage derivative threshold conditions, and removed them by replacing the voltage trajectory during a spike by the average of the values immediately before and after the spike. Significance of coherence responses in the populations of different cells was done by comparison to a numerically simulated Poisson spike train with a firing rate equal to the average rate of E type pyramidal cells. A one-way ANOVA was performed between the distribution of average coherence values in the stimulus bandwidth and the envelope bandwidth and the distribution of coherence values in the respective bandwidths from the Poisson spike trains.

4.3 RESULTS

P-units and ELL pyramidal cells can respond to the wide range of frequencies present in communication and prey signals (95, 115, 116). Here we investigate their response to the low frequency envelope signals expected to arise during foraging behaviour. Since the particular range of EOD frequencies varies considerably in natural fish groupings (107),

we chose to mimic the sensory signals present during foraging by using narrow (frequency) band Gaussian noise stimuli. The analytic signal, extracted via the Hilbert transform (117), can be used to estimate the envelope of these stimuli (Fig. 4-1 B); the mapping of stimulus to envelope is non-linear (see methods). A signal, amplitude modulated by a 20 Hz bandwidth, will have an envelope with power in the 0-20 Hz range (Fig. 4-1 B). Basilar pyramidal cells (E cells) are high pass in response to global communication-like signals (95, 116) (Fig. 4-2 A, upper) and, as expected, these cells also respond well to 20 Hz band pass noise with center frequencies ranging from 50-90 Hz (Fig. 4-2 A). To quantify the response to the stimulus we use the coherence function (see methods), which is the linear correlation coefficient between stimulus and response (S-R coherence) as a function of frequency. The S-R coherence does not account for

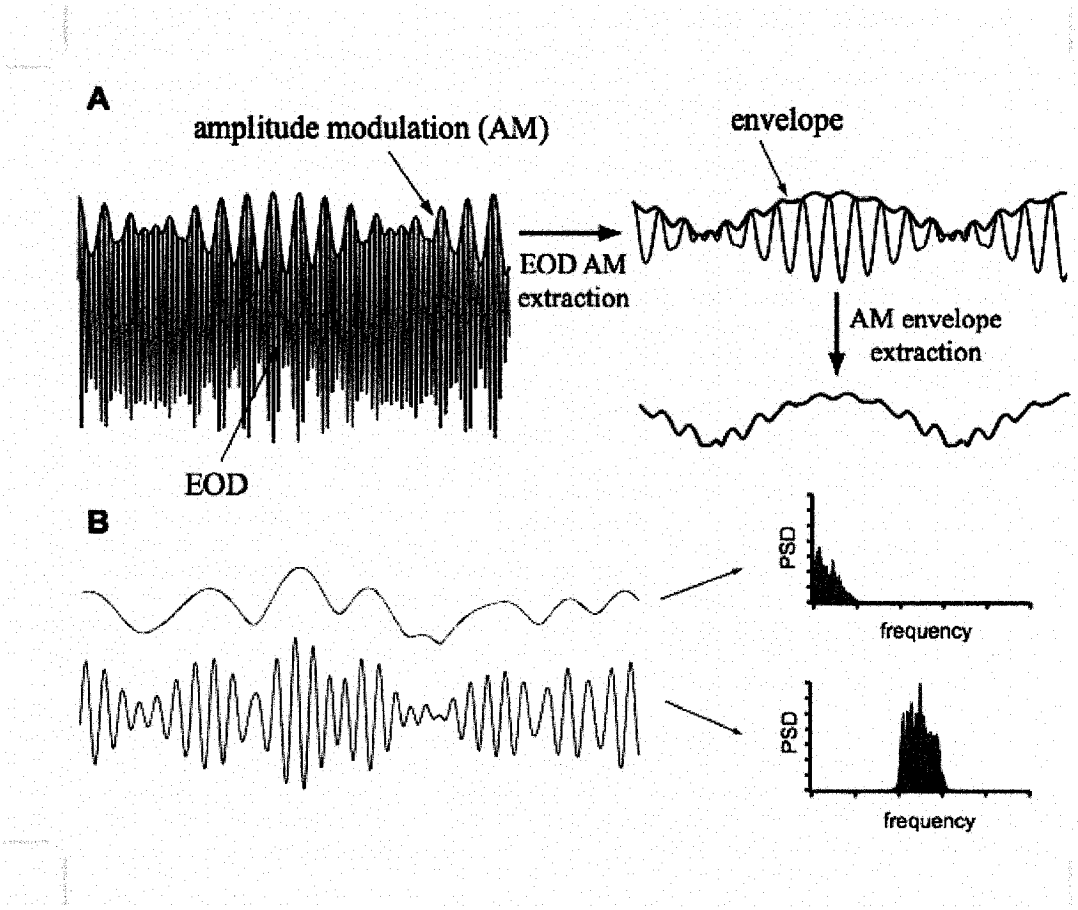

Figure 4-1: A mixture of three or more EODs gives rise to narrowband amplitude modulations. **A.** An example of a fish's EOD mixing with nearby conspecifics with frequency differences of +40 Hz and –50Hz (green). The amplitude modulation it creates has a 45 Hz oscillatory component (blue) with a slowly (10 Hz) varying contrast (red). **B.** To simultaneously test a broad range of EOD frequency differences we used narrowband Gaussian random amplitude modulations (RAMs) with 20 Hz bandwidth and center frequencies ranging from 30-90 Hz. This distribution of frequencies is expected based on the EODs of members of foraging groups (107). A sample realization of 40-60 Hz Gaussian noise (blue) will give an envelope (red) with power in the 0-20 Hz range. Their power spectral densities are shown on the right in the bottom and top panels, respectively.

signal transfer when there are non-linear mappings between the stimulus and the spike train response. The presence of non-linear mappings can be revealed by the R-R coherence. The R-R coherence is the coherence function between two different spike train responses given identical stimuli; discrepancies between S-R coherence and R-R coherence indicate a non-linear mapping (47). For example, the R-R coherence may reveal a response at frequencies not present in the stimulus.

E-R coherence can also be computed; this is the coherence between the stimulus envelope and the spike train response. The R-R coherence of E type pyramidal cells, under global stimulus geometry (see methods) was similar to the S-R coherence over the narrowband stimulus frequency range (in this case 40-60 Hz; Fig. 4-2 A) demonstrating that the signal transfer in this range is linear. However the R-R coherence also had power in the 0-20 Hz range indicating the presence of a non-linear transformation since the signal has no power in that frequency range. Further, at the 0-20 Hz range the E-R coherence was very similar to the R-R coherence demonstrating that pyramidal cells can respond to the envelope of a complex signal. Since there is no stimulus power in the 0-20 Hz range, this response must be due to a non-linear operation. To quantify the significance of these results we compared pyramidal cell E-R coherence to that of several other types of upstream neurons, downstream neurons, and interneurons, as well as to the E-R coherence from homogenous Poisson spike trains (as a control) using a one-way ANOVA; there were highly significant differences across these populations ($p<10^{-35}$). Multiple comparisons were made (Tukey HSD test) in order to determine the relative

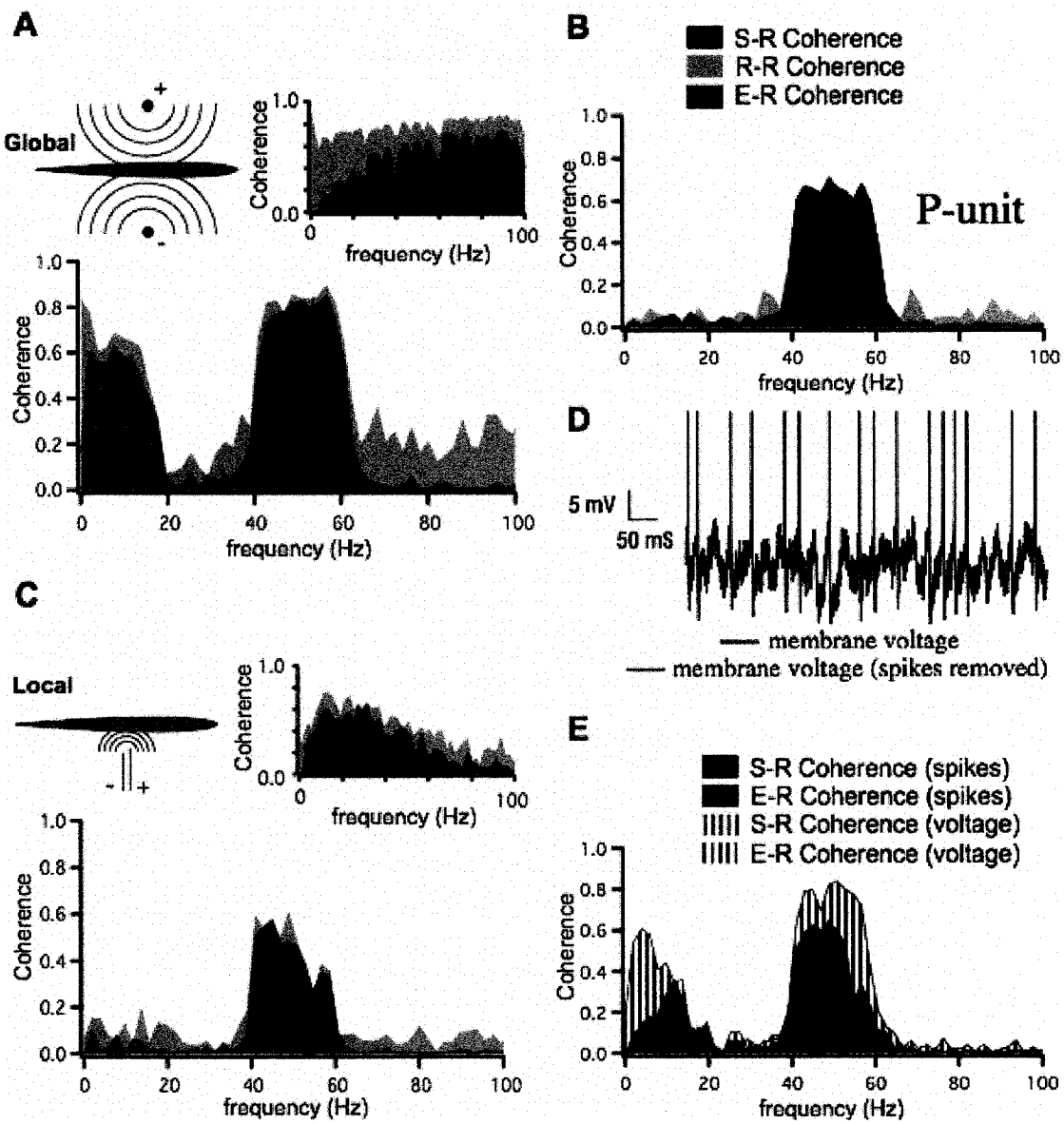
A
Global
Coherence
frequency (Hz)
B
S-R Coherence
R-R Coherence
E-R Coherence
P-unit
C
Local
D
5 mV
50 mS
membrane voltage
membrane voltage (spikes removed)
E
S-R Coherence (spikes)
E-R Coherence (spikes)
S-R Coherence (voltage)
E-R Coherence (voltage)

Figure 4-2: Pyramidal cells respond to narrowband envelope signals, whereas their afferent inputs do not. **A.** In global stimulus geometry an E type pyramidal cell, as expected (79), has high pass filtering characteristics when stimulated with broadband, 0-100 Hz, Gaussian noise (inset). The color-coding is according to the legend shown in panel **B**. When given narrowband, 40-60 Hz, stimulation, the same pyramidal cell responds linearly to that range of frequencies, shown by the S-R coherence (blue) and R-R coherence (grey), but responds non-linearly to the stimulus envelope, as shown by the R-R (grey) and E-R (red) coherence in the 0-20 Hz range. **B.** Primary sensory afferent fiber (P-unit) spike trains are good linear encoders, showing response in the stimulus range, 40-60 Hz (S-R (blue) and R-R (grey) coherence), yet show no response to the stimulus envelope. **C.** The same pyramidal cell (as in **A**) under spatially local dipole stimulation has low pass filtering characteristics, as expected (79), when stimulated with 0-100 Hz noise (inset). When given a saturating local 40-60 Hz RAM the cell responds linearly to the input signal, since R-R coherence (grey) and S-R coherence (blue) agree, but not to the stimulus envelope in the 0-20 Hz range. **D.** A sample (E type) pyramidal cell membrane voltage trace (black, spikes truncated) and subthreshold voltage trace (spikes removed, red). **E.** The S-R and E-R coherence between stimulus and both the spike train and subthreshold membrane voltage for the cell shown in **D**. The S-R and E-R coherence (red and blue, respectively) of the spike train with respect to the stimulus and envelope are shown with solid fills. The S-R and E-R coherence (red and blue, respectively) of the subthreshold voltage with respect to the stimulus and envelope are shown with vertical bar fills. In this case the spike train coherences were plotted over top of the voltage traces coherences because they have smaller values.

response in these different cell types in comparison to Poisson spike trains and each other.

For all classes of pyramidal cells (116) in the centrolateral and lateral segments of the ELL; the E-R coherence, averaged over the 0-20 Hz bandwidth, had a mean value (0.29 ± 0.14 S.D., N=52 units) that was significantly different from that of homogenous Poisson spike trains (0.01108 ± 10^{-5}, $p<10^{-3}$). In the following, unless otherwise stated, all significance comparisons are between a Poisson spike train and the cell's response to a global 40-60 Hz stimulus.

We then demonstrated that the source of the response to the stimulus envelope does not arise from P-unit input to the pyramidal cells, or from a non-linear operation intrinsic to the pyramidal cell. P-units are known to respond linearly to a broad range of frequencies of EOD amplitude modulation (>200 Hz, data not shown) (95, 118), yet when stimulated by a signal in the 40-60 Hz range they show little E-R coherence (0.034 ± 0.001, N=52, not significant). Stimulation that saturates only the receptive field center of E type cells (local stimulus geometry, see methods) removes the non-linear effects of the non-classical receptive field present under global stimulation, and reveals the isolated processing capabilities of the pyramidal cell (79, 116). Under saturating (79) local stimulus geometry (stimulus intensity matched to the global case) E type pyramidal cells respond to the 40-60 Hz signal yet fail to produce significant E-R coherence (0.026 ± 0.001, N=16, Fig. 4-2 C). The direct synaptic input from electroreceptor afferents and the synaptic input from locally projecting interneurons (119) are therefore not able to generate the envelope response.

As a check that the envelope response in the pyramidal cell spike train did not arise from the pyramidal cell spike generation mechanism under global stimulation, we examined the subthreshold membrane potential and calculated both the mean S-R (0.67 ± 0.16, 40-60 Hz range, N=11) and E-R (0.42 ± 0.19, 0-20 Hz range, N=11) coherence with the stimulus. Figure 4-2 D shows a sample spike train and the subthreshold voltage, low pass filtered (cutoff 200 Hz) to remove the EOD artefact (small amplitude potential coming directly from the electric organ), for an E type pyramidal cell. Figure 4-2 E shows the S-R and E-R coherence between the stimulus and both the spike train and membrane potential. As expected both responses were greater for membrane potential than the spike train confirming that the envelope arises from global synaptic inputs to the pyramidal cells and not the spiking non-linearity.

Given that the source of the envelope to the pyramidal cell is global we decided to examine ovoid cells, which provide global input to pyramidal cells (119, 120), as a candidate source of their envelope response. As previously reported (110) ovoid cells responded very strongly in a high pass fashion to broadband global signals (Fig. 4-3 A), but not local signals (data not shown); these responses are expected from the anatomy of ovoid cells (119) (i.e. extensive dendritic arborizations receiving P-unit inputs from a large fraction of the body surface) (109, 120, 121) and their receipt of gap junction input from P-units (41, 121). Ovoid cells also responded strongly to the signal envelope with a mean E-R coherence of 0.58 ± 0.23 (Fig. 4-3 B; N=11; $p<10^{-3}$). Furthermore, unlike pyramidal cells, they also responded to very high frequency noise signals (up to 180-200 Hz) and exhibit response to envelopes when presented these stimuli as well (data not

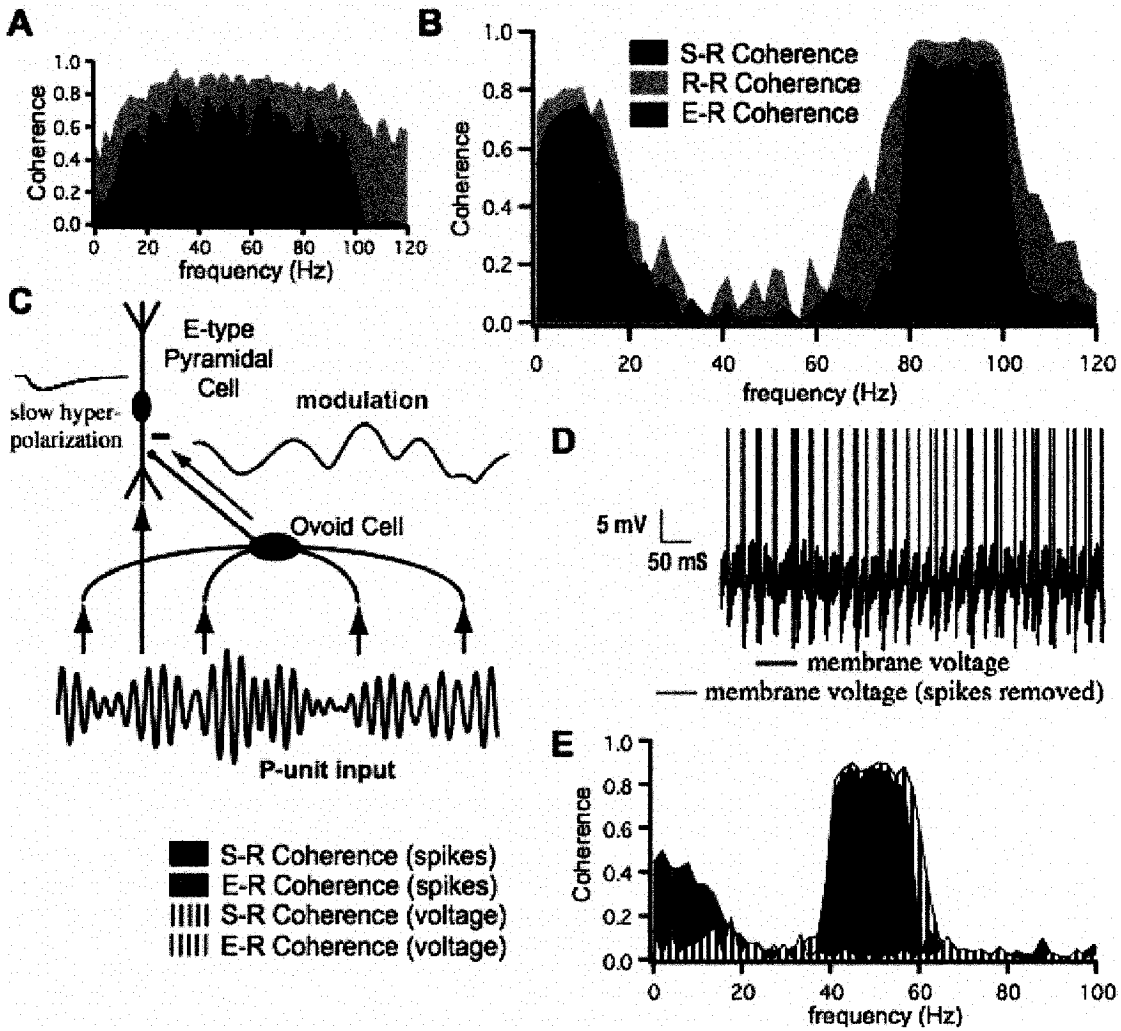
A
Coherence
frequency (Hz)
B
S-R Coherence
R-R Coherence
E-R Coherence
Coherence
frequency (Hz)
C
E-type
Pyramidal
Cell
slow hyper-
polarization
modulation
Ovoid Cell
P-unit input
S-R Coherence (spikes)
E-R Coherence (spikes)
S-R Coherence (voltage)
E-R Coherence (voltage)
D
5 mV
50 mS
membrane voltage
membrane voltage (spikes removed)
E
Coherence
frequency (Hz)

Figure 4-3: The spiking mechanism of ovoid cells generates narrowband envelope response that is transmitted to pyramidal cells through slow synapses. **A.** Ovoid cells are high pass when given global, broadband (0-100 Hz shown) Gaussian RAMs. **B.** In response to global, narrowband (80-100 Hz shown, similar results were obtained for center frequencies ranging from 30 to 190 Hz) stimulation they respond linearly to the signal (S-R coherence in blue and R-R coherence in grey), and also respond in a non-linear fashion to the stimulus envelope (R-R coherence (grey) and E-R coherence (red)) in the 0-20 Hz range. **C.** Under global stimulus geometry the E type pyramidal cells receive the stimulus directly through fast glutamatergic synapses from P-units (blue arrows), and the stimulus envelope indirectly through GABA-B-like synapses from the ovoid cell (red arrows). The ovoid cell is high frequency tuned so that it will respond well to 'carrier' frequencies, extracting the slower envelope and exclusively passing it to pyramidal cells, filtering out the 'carrier' with a slow synapse. **D.** A sample voltage trace from a somatic intracellular recording of an ovoid cell (spikes truncated, black). Superposed on this trace is the same trace with spikes removed (see methods) and low-pass filtered to remove the EOD artefact. The artefact is a small portion of the EOD being picked up directly by the intracellular electrode, which is caused by electrical activity of the cell. **E.** S-R and E-R coherence between stimulus and both the spike train and subthreshold membrane voltage for the cell shown in **D**. The S-R and E-R coherence (red and blue, respectively) of the spike train with respect to the stimulus and envelope are shown with solid fills. The S-R and E-R coherence (red and blue, respectively) of the subthreshold voltage with respect to the stimulus and envelope are shown with vertical bar fills. In this case the spike train S-R coherence and the voltage trace E-R coherence were plotted on top since they have smaller values.

shown). Ovoid cells receive only P-unit input (122) and, since P-units do not themselves extract the envelope, it appeared likely that the envelope must first be extracted by a non-linearity associated with ovoid cell spiking. Preliminary data suggests that envelope extraction requires low membrane noise and the spiking threshold nonlinearity (J.W.M, E. Harvey-Girard, A.L., and L.M. (123)). Most recordings from ovoid cells were made from their thick axons as previously reported (110), and their membrane potential did not reflect the stimulus (data not shown). In one case, however, we achieved an intracellular somatic recording from an ovoid cell. In this case the membrane clearly tracked the stimulus (Fig. 4-3 D) so that the S-R was very high and similar to that of the spike train (Fig. 4-3 E). The membrane potential of this cell showed no E-R coherence although its spike train clearly did (Fig. 4-3 E, average E-R coherence of 0.37, 0-20 Hz, average S-R coherence of 0.86, 40-60 Hz range). This suggests that the ovoid cell is the first site where a non-linearity associated with the spike threshold extracts the signal envelope associated with bandpass Gaussian stimuli.

It appeared puzzling that the strong linear response of ovoid cells to the high frequency signal was not also transmitted to its pyramidal cell targets. Ovoid cells are GABAergic (119) and their stimulation *in vivo* (110) or *in vitro* (41) causes a slow inhibitory postsynaptic potential (IPSP) in E-type pyramidal cells that appears to be mediated solely by GABA-B like receptors (41). We propose that these slow IPSPs will act as a low pass filter of the ovoid cell output, removing the high frequency content and transmitting only its envelope response.

As an additional test of our hypotheses we also examined envelope extraction in nonbasilar pyramidal cells (I cells). I cells are a morphologically and functionally distinct population that receives indirect P-unit input (via locally projecting interneurons) and are low pass (116, 120, 122). As expected, these cells responded at best weakly to a global bandpass signal when its center frequency was >30 Hz; however they still produced E-R coherence comparable to that of E cells. This response is illustrated in Fig. 4-4 A where an I cell given 80-100 Hz stimulation showed no response to the signal while still responding to its envelope (E-R: 0.20 ± 0.09; S-R: 0.029 ± 0.021, N=8; Fig. 4-4 A). We conclude that the I type pyramidal cell is not responsible for generating the envelope response as it shows no response to the narrowband signal from which to extract the envelope (48, 124). This form of processing is similar to neurons in the visual or auditory systems showing no linear response to a high-frequency signal, but instead responding to its envelope (48, 100, 101, 103-105, 125-129). Extraction of the signal envelope is therefore not due to the intrinsic dynamics of pyramidal cells or input from electroreceptors (directly or via local granular interneurons). With these sources eliminated we conclude that the envelope response requires input with global stimulus geometry, presumably the ovoid cell (see methods).

Ovoid cells project indirectly to I-type pyramidal cells via local granular interneurons (119) and the resulting responses are also slow (110); because the ovoid cell input to I cells is via an inhibitory interneuron, it is sign inverted and appears as a slow depolarizing potential (110). Thus we propose that the envelope response of I-type

pyramidal cells is also generated by the ovoid cells but via slow modulation of the response of local interneurons (41, 110).

Our model for the parallel transmission of the envelope along with the signal to E type ELL pyramidal cells is illustrated in Fig. 4-3 C; ovoid cells respond to the high frequency signals and generate a response to its envelope via a non-linearity such as half-wave rectification (89), possibly implemented by the thresholding spiking non-linearity (130); they transmit the response to the stimulus envelope to the pyramidal cells via a slow synapse, while information about the stimulus (to E cells) comes via fast glutamatergic P-unit synapse on their basilar bush (41). Figure 4-4 B shows a model to explain the I cell envelope response: the ovoid cell passes on the envelope signal to another local interneuron with the net result being depolarization at the I type pyramidal cell. Since for a narrowband stimulus the envelope is the same whether or not the stimulus is inverted it does not matter whether the slow signal is passed via inhibitory or excitatory synaptic input as long as they have a slow time course.

In addition to the ovoid cell global feedforward input, the ELL pyramidal cells receive extensive global feedback input (111, 116) and the envelope response might therefore also be generated or modified via a feedback mechanism. Feedback input to ELL emanates mainly and perhaps exclusively from one class of pyramidal cells: the deep pyramidal cells (DBP) (111). Previous studies have shown that DBP cells fail to respond to very high frequency AMs (116). However, global stimulation of deep pyramidal cells with 180-200 Hz stimuli generated an envelope response without any response (S-R or R-R) to the signal itself (E-R: 0.17 ± 0.07; S-R: 0.006 ± 0.002, N=5,

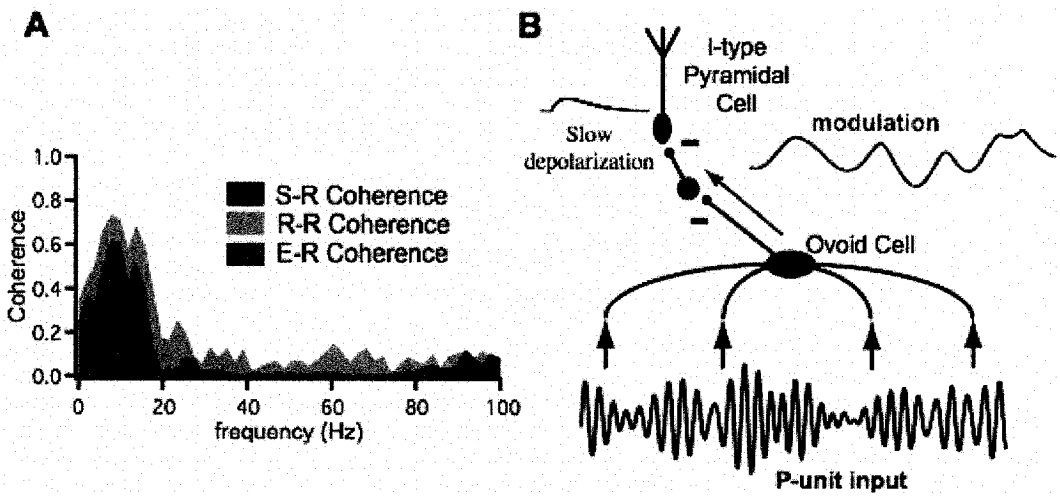

Figure 4-4: The envelope response generated by ovoid cells can also be transmitted to principal cells via intermediate neurons. **A.** Under global stimulus configuration some non-basilar, or I-type, pyramidal cells fail to respond to the AM signal yet show strong response to the stimulus envelope as shown by the R-R (grey) and E-R (red) coherence in the 0-20 Hz range. **B.** The response in I type cells is mediated by an additional inverting local interneuron, showing that the envelope response may be hyperpolarizing or depolarizing in nature.

Fig. 4-5 A). Ovoid cells are the only ELL neurons able to respond to AMs with frequencies >180 Hz (data not shown); they are therefore the sole source of DBP input capable of generating envelope power.

Furthermore, under these conditions there should be no source of narrowband, high frequency (>180 Hz) input available to higher brain feedback circuitry from which to extract the envelope. To investigate whether the global feedback pathway driven by the DBPs (111) might still influence the envelope response of pyramidal cells, we have recorded from feedback (nucleus praeminentialis, nP) afferent fibers in the eminentia granularis posterioris (EGp), a cerebellar-like structure shown to be responsible for global gain control and adaptive sensory cancellation (111). Consistent with earlier reports (111) we found that nP afferents were high pass (Fig. 4-5 B, inset) and also responded well to narrowband frequencies. These afferents did not, however, respond to the envelope in their spike train response, having a mean E-R coherence of 0.049 ± 0.001 (Fig. 4-5 B; N=16, not significant). It is therefore unlikely that feedback input contributes to or modifies the pyramidal cells' envelope response. Since the DBPs did respond to the stimulus envelope but nP afferents did not; these results imply that the envelope response is filtered out within nP and, unlike direct low frequency input (79, 111, 115), is therefore not available as a cancellation signal to ELL.

The E-R coherence (global stimulation) of E and I type pyramidal cells were not significantly different ($p=0.1482$) and so the responses of these populations were pooled. The E-R coherence of pyramidal cells is significantly greater than P-units, pyramidal cells with local stimulation and nP afferents ($p<10^{-3}$). The E-R coherences of these last

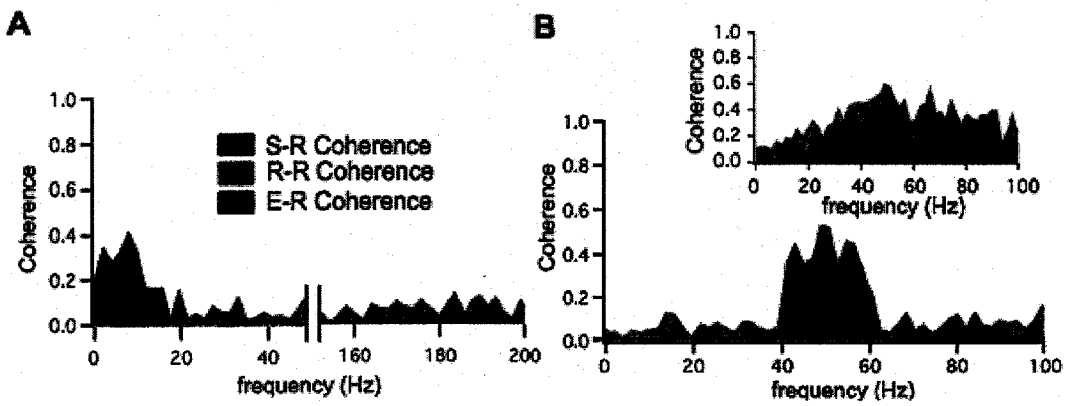

Figure 4-5: Feedback inputs are not responsible for generating the envelope response. **A.** When given high frequency, global, stimulation outside of their range of sensitivity (180-200 Hz shown), deep pyramidal cells, the sole source of inputs to higher feedback centers (116), show envelope response (R-R coherence (grey) and E-R coherence (red)) in the 0-20 Hz while showing no response in the 180-200 Hz range. This also rules out the role of feedback pathways in the generation of the stimulus envelope to the pyramidal cells since, for the neurons responsible for the feedback signal, the narrowband signal is unavailable (blue) for the extraction of the envelope under this stimulus condition. **B.** The majority of Pd afferent axons in the EGp are high pass in response to broadband, 0-100 Hz, stimulation (inset). When given narrowband, high frequency (80-100 Hz shown, similar results were obtained for center frequencies ranging from 30 to 90 Hz) stimulation, their spike trains show good response to the direct stimulus (S-R coherence (blue), R-R coherence (red)) and no response to the envelope. This rules out the transmission of the envelope signal to the pyramidal cell apical dendrite via the indirect feedback pathway.

three populations were not significantly different from each other, nor from the Poisson spike train. The mean E-R coherence of the ovoid cells is about double that of pyramidal cells (0.58 vs 0.29, $p<10^{-5}$) further suggesting that the ovoid cells are the source of envelope response in pyramidal cells.

4.4 DISCUSSION

We have shown that parallel pathways transmit the electrosensory narrowband signal and their envelopes from P-unit electroreceptors to pyramidal cells. The direct projection from P-units to pyramidal cells conveys the narrowband signal. An indirect pathway from P-units to pyramidal cells via a fast interneuron with slow output synaptic kinetics extracts the envelope of the narrowband signal.

Similar processes may be operative in the auditory and visual system. The spectrotemporal structure of communication vocalizations reveals modulations at different carrier frequencies (131, 132). The relationship between envelope and carrier frequencies determines the perception of pitch fluctuation, pitch roughness, and subharmonic, or residue pitches (45, 98, 133). In visual scenes, envelopes (spatial contrast modulations) are responsible for groupings of objects and illusory contour perception (100, 102, 103). There is mounting evidence that the invariant response to object groupings arise from parallel network structure consisting of separate linear (first order) and non-linear (higher order) channels. This parallel transmission supports the idea of cue invariance in the visual system, where objects are perceived similarly if they are delineated by either intensity or contrast boundaries (48, 100-105). It has also been shown that cells in the inferior colliculus (IC) respond to interaural time differences

(ITDs) of low frequency pure tones and low frequency modulations of high frequency carrier tones (126, 129). This response to low frequency signals and envelopes of high frequency narrowband signals can be thought of as another form of cue invariance except in this case pertaining to sound localization, not object perception. Observations of independence between optimal carrier and envelope frequencies in the auditory cortex also support the idea of parallel transmission of signal and envelope (125, 127, 128).

Electric fish may require separate responses to both the envelope and direct electrosensory signals to distinguish the frequencies, and therefore the identities, of the other fish within a foraging group. EOD frequency differences between fish are detected as direct inputs to the ELL. At very high EOD frequency differences (>200 Hz) the P-units and thus the pyramidal cells can no longer reliably track the stimulus (Benda, Longtin and Maler, unpublished results); further, midbrain neurons in receipt of ELL input respond mostly to lower frequencies in a related wave type gymnotiform fish (134).

In auditory and visual systems it is observed that the envelope generating mechanism does not interfere with response to direct, low frequency stimulation (48, 100, 101, 103-105, 125-129). In fact when first order and higher order stimuli represent the same cues they can actually interact constructively as was recently shown in stereopsis (106). The magnitude of response to envelopes is dependent on the carrier frequency, which is typically much higher than envelope frequencies. A result of this design is that information typically takes one of two parallel pathways, i.e. linear or non-linear. The direct P-unit synapses onto pyramidal cells (linear) in parallel with the ovoid cell synaptic input to pyramidal cells (non-linear) satisfies this design criteria (Fig. 4-3 D). A low

frequency signal delivered to the cell's receptive field center will pass through the P-unit synapses to the pyramidal cell (linear pathway, Fig. 4-2 C inset), while being filtered out in the ovoid cell due to its high pass frequency response (Fig. 4-3 A). In contrast, ovoid cells respond to even very high frequency narrowband signals (180-200 Hz, data not shown), extracting the low frequency envelope and passing to the pyramidal cell (non-linear pathway); I type pyramidal cells have a low pass frequency response (116) and thus do not respond directly to the very high frequency signals.

The two-cell network we have identified, consisting of a high pass interneuron that can extract the envelope and that connects to the output cells via slow inhibitory synapses, is a simple way of extracting and separately transmitting linear and non-linear (slower) stimulus features. The types of stimuli used in this study are relevant to visual and auditory systems as well (45, 98, 100, 103, 131, 132). Response to the signal envelope is seen up to cortical levels of both auditory and visual systems. The basic building blocks of our simple network, high pass interneurons (135) and interneurons that utilize GABA-B receptors on pyramidal cells (136-139) are present at cortical levels, suggesting that this simple neural implementation of parallel linear and non-linear information streams might be widespread.

CHAPTER 5: ENVELOPE GATING AND NOISE SHAPING IN POPULATIONS OF NOISY NEURONS

5.0 ABSTRACT

We show conditions where the response of real and model neurons is linearly correlated with narrowband signals and the slower envelope of such signals. Power at the envelope frequencies will act as a noise background when the neurons must respond to other signals in that band. We further show that a novel form of noise-shaping can increase the signal-to-noise ratio in the envelope band. The effect, based on uncorrelated intrinsic additive noise in neurons followed by averaging, is expected to apply to a broad class of nonlinear threshold systems.

5.1 INTRODUCTION

Nonlinear dynamical systems driven by noise and harmonic signals can display a range of interesting phenomena. This is particularly the case for excitable "threshold" systems in e.g. biology and laser physics (140-143). In physical systems, harmonic signals are often more of a narrowband nature, with power over a finite bandwidth. This class of signals, with statistical properties intermediate to those of harmonics and broadband noise has been studied in bi-stable systems (144, 145), charge density waves in semiconductors (146) and in coupled Josephson junctions (147). In the field of neuroscience narrowband signals occur in natural stimuli (44, 127, 148) and are commonly found in large-scale cortical activity (50, 149). Narrowband signals have multiple associated timescales: one related to a fast oscillation, or carrier, and a longer one related to the slow modulation, or envelope, of the carrier.

In this Letter we first show, using experiments and theory, how the spike generation threshold is a sufficient non-linearity for envelope response generation that is universal to

all spiking neurons. Using these results we show how populations of neurons can transmit small amplitude signals in the presence of ongoing background rhythmic inputs. This leads to a new form of noise shaping to enhance population signal-to-noise ratio (SNR), which paradoxically arises from the addition of intrinsic uncorrelated noise, with subsequent population averaging, in contrast to previous mechanisms resulting from reciprocal feedback in a network (96) or single cell negative interspike interval correlations (94).

5.2 METHODS

The model neuron used in this study is the leaky integrate-and-fire (LIF) neuron (19), with dynamics:

$$\frac{dv}{dt} = -\frac{v}{\tau} + \mu + \sqrt{\frac{2D}{\tau}}\xi(t) + S(t) \tag{5.1}$$

where v is the trans-membrane voltage, τ is the membrane time constant, μ is the stationary input bias, and $S(t)$ is an input signal. For all following results $S(t)$ is a narrowband Gaussian process with power in the 40-60 Hz range. The stimulus envelope, $E(t)$, is computed with a non-linear transformation, i.e. taking the time-varying amplitude of the analytic signal via the Hilbert transform (117), and in this case gives a signal with power in the 0-20 Hz range. The intrinsic membrane noise, $\xi(t)$, is a Gaussian white noise process, i.e. $\langle \xi(t)\xi(t') \rangle = \delta(t-t')$, and has an intensity D. This dynamics is supplemented with absorbing and reset boundaries at v_R and v_T, respectively. The times at which the voltage process is absorbed and reset represent spike times.

The stationary mean rate of firing for the noisy LIF is given by (150):

$$r_0 = \left(\tau\sqrt{\pi} \int_{-(v_R-\mu\tau)/\sqrt{2D\tau}}^{-(v_R-\mu\tau)/\sqrt{2D\tau}} dz e^{z^2} \mathrm{erfc}(z) \right)^{-1}. \quad (5.2)$$

The stationary rate plotted as a function of input bias is also known as the frequency-input (F-I) curve. Except for comparison with experiments this model will be kept in the non-dimensionalized form, with the exception of the time constant, $\tau = 10\,\mathrm{ms}$, to preserve firing rate in units of Hz.

We make the ansatz that the response of the LIF to the envelope will be in the form of a time-varying modulation of the firing rate. This approach is similar to that used in linear response theory for LIFs, where the response to weak signals is in the form of a time-varying deviation in the firing rate from the stationary value (151, 152). We hypothesize that the instantaneous firing rate is determined by Eq. (5.2) where the input current, μ, is replaced by the time-dependent form $\mu(t) = \mu + a(\omega) \cdot S(t)$. The scale factor, $a(\omega)$, depends largely on the sub-threshold membrane dynamics and could be an attenuating factor ($a(\omega)<1$) in the case of low-pass filtering or an amplifying factor ($a(\omega)>1$) if the membrane dynamics has resonant properties (153). The factor $a(\omega)$ should be approximately the susceptibility averaged over the narrow frequency band of the input signal, but as we are using large amplitude inputs we fit this as a free scalar parameter for simplicity in exposing the effects of interest. The model parameter, $a(\omega)$, was fit to match the numerical simulation results with all other parameters fixed.

The rate transfer model thus consists of Eq. (5.2) supplemented with subthreshold, frequency dependent filtering. The response to the carrier signal may be removed by averaging the output rate over a timescale larger than that of the carrier. Figure 5-1 is an

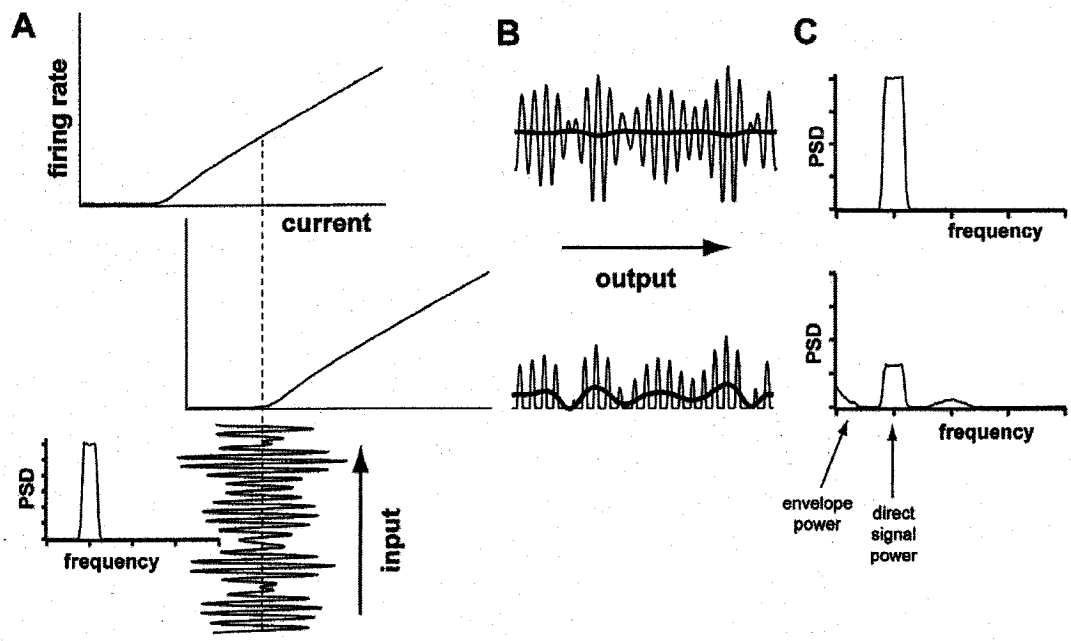

Figure 5-1: **A** When the average value of the input current (power spectral density shown on left) is superthreshold (top), the signal transfer is linear, leading to low signal distortion in the output firing rate (**B**, top), and output power in the signal bandwidth (**C**, top). The lack of slow drifts in the output firing rate is visible in the temporal domain when the rate is averaged over the timescale of the fast carrier oscillation (**B**, top, thick line). When the average value of the input is near the firing threshold (**A**, bottom) the output firing rate is a rectified version of the input (**B**, bottom). The slow modulations become apparent in the temporal domain (**B**, thick line), and in the frequency domain (**C**, bottom) by the presence of low frequency output power.

illustration of this form of transfer function. In Fig. 5-1 A (bottom) the average input current is at the rheobase (i.e. the value of current at which the firing rate becomes non-zero) of the F-I curve. During positive phases of the input signal the output firing rate varies proportionally to $\mu(t)$, while for the duration of the negative signal phase the firing rate remains at zero. An average of the firing rate over one fast cycle of the input current will vary proportionally to the signal envelope (Fig. 5-1 B, bottom, thick line). When the average input current is far above rheobase (Fig. 5-1 A, top) the corresponding output rate is linearly related to the input (Fig. 5-1 B, top) and has no slow drifts (thick line). The power spectral densities (PSDs) in Fig. 5-1 C illustrate the lack (top) or presence (bottom) of envelope power.

The measure of linear signal transfer we use between the original stimulus, $S(t)$, and the spike train response, $R(t)$, is the frequency dependent coherence function, $C_{SR}(f) = |S_{SR}(f)|^2 / (S_{SS}(f) S_{RR}(f))$. $S_{SR}(f)$ is the cross-spectral density between the stimulus and the spike train response and $S_{SS}(f)$ and $S_{RR}(f)$ are the auto-spectral densities of the stimulus and response, respectively. The coherence function, $C_{SR}(f)$, is also used as a measure of linear signal transfer, treating the envelope as an input signal.

5.3 RESULTS

The model based on the firing rate transfer function for the stimulus envelope predicts that neurons with average current near the rheobase would respond to the stimulus envelope better than neurons far into the superthreshold regime (i.e. average input current far above rheobase). Figure 5-2 A compares the stimulus driven average F-I curve from the firing rate model (5.2) (circles) and from numerical simulations of the LIF (5.1) (line).

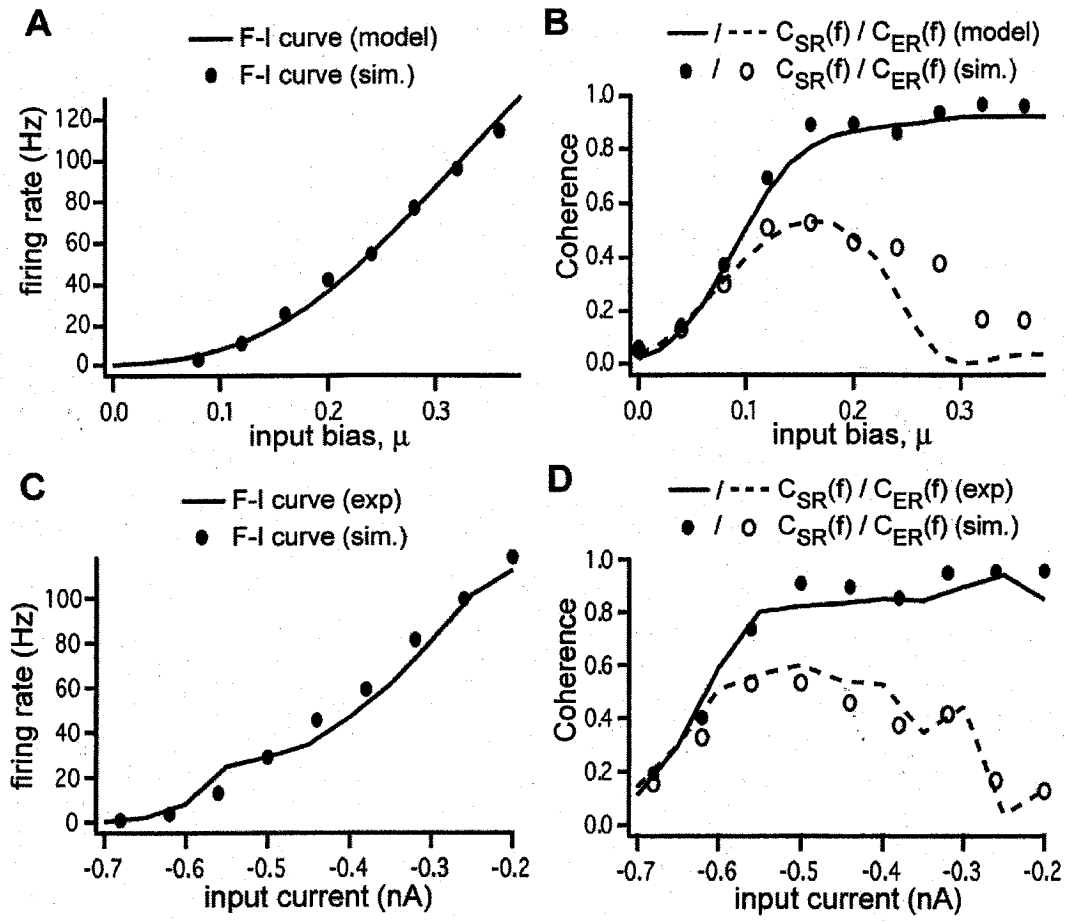

Figure 5-2: **A** the comparison of the firing rate versus input current curve for the rate transfer model and a numerical simulation of a LIF model neuron. **B** Comparison of the coherence predicted by the rate transfer model and that obtained by numerical simulation of Eq. (5.1). The solid line and filled circles show the values of coherence between a 40-60 Hz Gaussian stimulus and the response spike trains (SR coherence), averaged over the stimulus bandwidth and shown as a function of input current. The dashed line and open circles show the values of coherence between the envelope of the same signal and the spike trains (ER coherence), averaged over the 0-20 Hz range of the envelope power. The current rheobase in this case is $\mu = 0.1$. **C,D** Comparison the results of LIF simulations to pyramidal cell spike train responses *in vitro*. A constant depolarizing current of 0.7 nA was added to the model to account for depolarizing leak current from the impaling electrode in this recording. Preparation of ELL slices and electrophysiology techniques were as previously described (154). All experimental protocols were approved by the University of Ottawa Animal Care Committee.

Figure 5-2 B compares $C_{SR}(f)$ and $C_{ER}(f)$ calculated from the firing rate model (filled and open circles, respectively) and from numerical simulations of the LIF neuron (solid and dashed lines, respectively). Note that the response of the corresponding LIF simulation was in the form of a spike train, not a continuous firing rate variable. For the rate transfer function model two free parameters were used to account for the background noise power in the 0-20 Hz and 40-60 Hz bandwidths expected for spike trains. $C_{SR}(f)$ increases with input current and saturates for input currents corresponding to very high firing rates as a consequence of the general dependence of information transfer on firing rate (155). $C_{ER}(f)$ increases with current near the rheobase (0.1 in this example) but decreases for higher currents, where the F-I curve is more linear.

Figure 5-2 C and D compare a numerical simulation of the LIF model neuron and an *in vitro* recording made from a sample pyramidal cell. The input current for the model neuron was re-dimensionalized and rescaled in units of (nA) to match the injected current levels of the real neuron. This same qualitative result was found in a total of $N = 9$ cells. It has been previously shown that LIF neuron models can effectively reproduce first order firing statistics of real neurons, and also good qualitative fit to second order statistics with parameter fit to the first order (156); we also show good agreement between real and simulated neurons using coherence as a higher order statistic. The real neurons show the predicted dependence of coherence on input current - saturation of $C_{SR}(f)$), and a non-monotonic dependence for $C_{ER}(f)$. Higher μ values bring on a more linear regime and thus $C_{ER}(f)$ drops. Together, these results confirm the validity of the rate transfer model in describing the response of LIF neurons or real neurons to narrowband signals.

The previous results were obtained in scenarios with relatively low levels of intrinsic noise. By and large, intrinsic membrane noise has a deleterious effect on the extraction and transmission of the signal envelope. Figure 5-3 A shows the $C_{SR}(f)$ as a function of mean input current from the rate transfer model for different values of noise intensity. The standard deviation of the narrowband signal added was 0.8. $C_{SR}(f)$ decreases with increasing intrinsic noise, but the fractional decrease is relatively small considering the noise is increased three orders of magnitude. In the subthreshold regime $C_{SR}(f)$ actually increases; this is due to stochastic resonance. $C_{ER}(f)$ is not as robust against the influence of noise as $C_{SR}(f)$. For the same range of noise intensities Fig. 5-3 B shows the peak of the ER coherence decreasing at least three-fold. The main effect of intrinsic noise is to wash out (i.e. linearize) the effective current threshold responsible for rectifying the input signal (150).

Figure 5-3 C shows the effect of intrinsic noise on the power spectrum of a single simulated spike train. When intrinsic membrane noise is increased from $D = 0.005$ to $D = 0.5$ the entire broadband spectrum increases. The shape of the power spectrum is changed as well: the narrowband power at envelope frequencies (0-20 Hz) and higher harmonics of the fundamental frequency range are washed out relative to the background. *We may then ask what effect this noise-dependent spectral shaping may have on signal transmission in neurons driven by narrowband rhythms.* The answer may be pertinent to neurons in different cortical areas that are subject to large spatial scale narrowband rhythms; these do not correspond to sensory stimuli but are often related to other tasks such

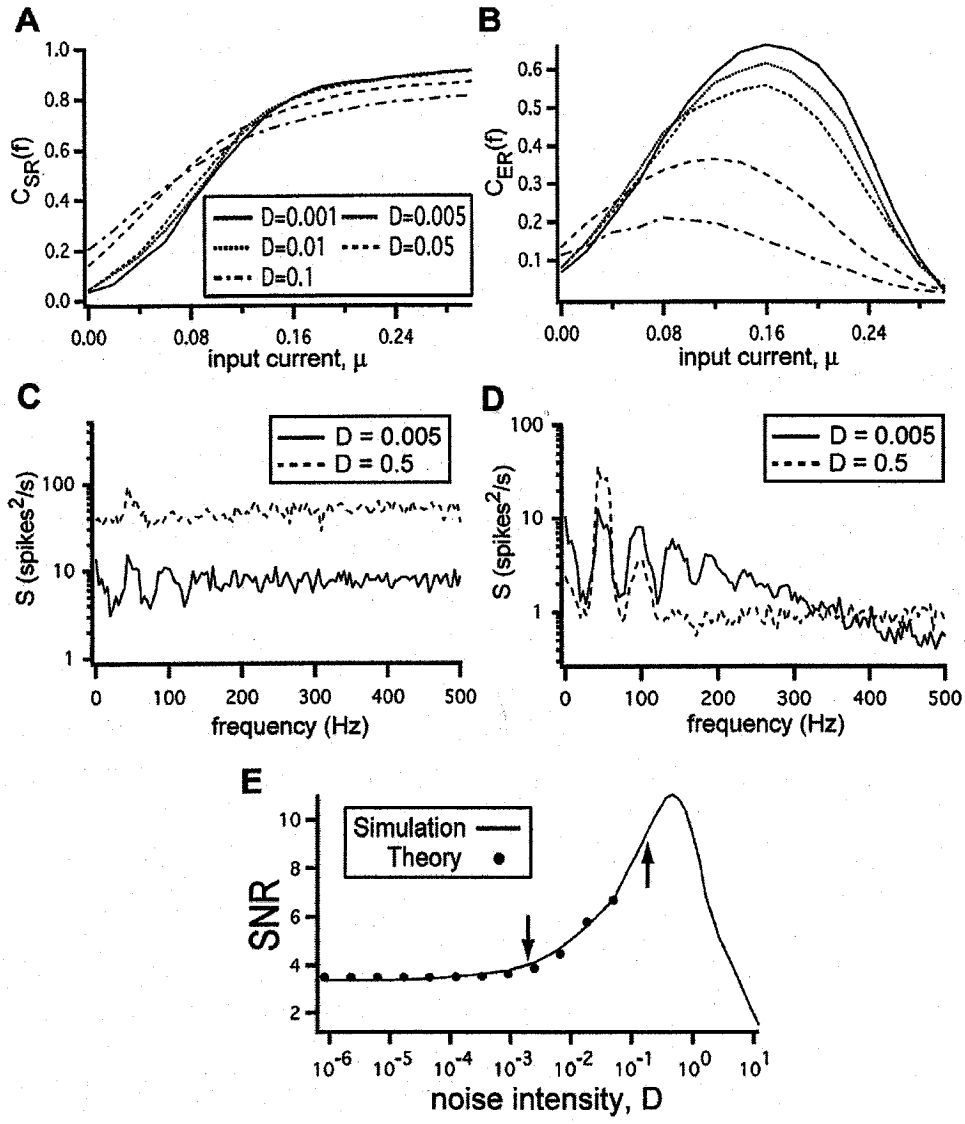

Figure 5-3: **A,B** The averaged values of $C_{SR}(f)$ and $C_{ER}(f)$, respectively, as a function of input current, for different values of noise intensity in the rate transfer model Eq. (5.2). **C** Power spectra of the spike train of a simulated neuron, Eq. (5.1) with 40-60 Hz Gaussian input for two different noise intensities with $\mu = 0.12$ and $\tau = 10$ ms. **D** The power spectra of the average spike trains of $N = 50$ identical neurons with common narrowband input and independent membrane noise sources. **E** When a small amplitude, low frequency $f = 10$, sinusoidal input is added to the simulated network the SNR of the averaged spike train shows a non-monotonic behavior as a function of noise intensity, D (line). A noise-dependent rheobase shift predicts the low frequency behavior of the SNR in the small noise limit (circles). The arrows indicate the SNR for noise values used in **C** and **D**.

as directing attention (50, 149, 157). In this scenario, low-frequency envelope power would interfere with other signals being transmitted in the same envelope bandwidth. The addition of noise to a single cell removes the envelope power by linearizing the F-I curve, but in doing so adds extra broadband power (Fig. 5-3 C). If the spike trains from a population of N identical neurons with independent intrinsic noise are averaged, the extra broadband power can be reduced as it varies as $1/N$. Figure 5-3 D (dashed, $D = 0.5$) shows the power spectrum of the average spike train in a population of $N = 50$ simulated neurons displaying reduced envelope power relative to the power in the fundamental range. In the low noise case the envelope component, common to all neurons, cannot be effectively averaged out (Fig. 5-3 D, solid, $D = 0.005$).

Figure 5-3 E shows the effects of this form of noise shaping on signal transmission. When a small amplitude sinusoidal current is introduced whose frequency, ω_o, is in the envelope bandwidth is added to the scenario in Fig. 5-3 D, the signal-to-noise ratio ($\text{SNR} = \lim_{\varepsilon \to 0} 2S(\omega_o)/[S(\omega_o - \varepsilon) + S(\omega_o + \varepsilon)]$) is dependent on D. The SNR with respect to this signal increases with increasing noise intensity up to a point and then decreases when the single cells can no longer respond coherently with the sinusoidal current in the very high noise environment. The increase in SNR can be understood when one considers that the envelope power is extracted from rectification by the F-I transfer function in Eq. (5.2). A general, biased rectifying device results in total envelope power proportional to $A^2 - B^2$ where A^2 is the signal variance and B is the bias (89). Increasing noise has the effect of shifting the rheobase leftwards. With this in mind we can make a first-order approximation that increasing the noise shifts the bias, i.e. $B \propto k - D$ where k is an

arbitrary constant. A small noise expansion of the SNR gives a second order polynomial, $\mathrm{SNR} \approx a - bD + cD^2$ which we have fit (circles) to the numerical simulation results (lines) in Fig. 5-3 E to show that changing the bias in rectification predicts the small noise regime of the SNR in this system. The arrows indicate the SNR at the noise values used in Fig. 5-3 C and D. Even though stochastic resonance (SR) is visible in Fig. 5-3 A and B for very low input currents (increasing $C_{SR}(f)$ and $C_{ER}(f)$ with D), it does not play a role in this form of noise shaping as the bias, μ, used for Fig. 5-3 C, D and E is superthreshold. This effect also differs from superthreshold stochastic resonance (SSR) (158). In SSR the addition of noise increases the SNR by increasing the effective sampling rate of a high frequency signal. Here we remove extra "background" low frequency power, by linearizing and then averaging, thus increasing SNR.

5.4 DISCUSSION

We have examined the nature of envelope extraction in biophysical spiking neurons and confirmed the validity of the underlying mechanism in pyramidal cell recordings *in vitro*. The envelope-response coherence, $C_{ER}(f)$, shows a strong dependence on average current inputs as well as on intrinsic membrane noise. This mechanism could play a role in gating the flow of envelope information in sensory systems where the envelope represents a pertinent cue (45, 127, 148). Also, with these results we may hypothesize that a novel form of noise shaping could take place in cortical areas where macroscopic rhythms (50, 149, 157) and neurons with high degrees of variability (37) are found. This form of noise shaping is mediated by an increase in intrinsic noise as opposed to network connectivity (96) or intrinsic single cell temporal correlations (94). Experimental validation of this

hypothesis may be difficult *in vivo*, although we predict this form of noise shaping could be observed in iterated network experiments (159) *in vivo*. We predict that the envelope response described here is a general property of non-linear threshold devices and thus our proposed form of noise shaping could be more generally applied to signal transmission in arrays of generic threshold devices.

CHAPTER 6: ENVELOPE CODING THROUGH PHASE DIFFERENCE IN POPULATIONS OF COUPLED OSCILLATORS WITH ANTI-SYNCHRONOUS DYNAMICS

6.1 INTRODUCTION

In the study of neuronal dynamics and information processing there are many questions pertaining to the nature of the signal, or information being encoded, and the representation of this information in terms of neural activity. The problem of optimally encoding stimulus through linear means has been well characterized (118, 160-162). Here the output spike train fires with a probability that is a linear function of its input. The input, in turn, can be "decoded" from the spike train by linear, reverse correlation techniques. The stimuli in question are oscillatory signals with narrowband spectral content. In general these signals can be decomposed into a carrier signal and a time-varying contrast, or envelope. The signal envelope has been shown to be crucial for stimulus perception in visual (48, 101, 124) and auditory systems (45, 126, 163), and based on electrophysiological results it has been recently speculated that this type of feature is important for properly identifying conspecifics within a population of weakly electric fish (44).

Although there has been growing interest in non-linear signal representations the number of possible representations and mechanisms for creating them becomes daunting. Here we focus on a specific non-linear representation of signal envelope in model neurons and explain the mechanism responsible for this transformation with analytic and simulation results. We understand these results in terms of a geometrical picture of the phase space of the dynamical system describing these model neurons. The mechanism described involves the interplay between synaptic dynamics of coupled cells and the dynamics of signal integration from a common external source, which results in a

representation of the envelope as a time-varying phase difference between superthreshold spiking neurons.

This type of stimulus encoding has not been observed in peripheral sensory systems, however it has been observed that relative spike timing between neurons is of importance in different cortical areas and in the hippocampus. What is more is that the areas in which these observations have been made typically exhibit global oscillations themselves or receive global oscillations from other areas in the brain occupying different frequency ranges. Thus the representation of a signal as phase differences is possible as the two necessary ingredients, global narrowband oscillations (50, 149) and mutual synaptic coupling (164, 165), have been observed in higher brain centers.

This chapter follows from the study of single cell envelope processing in chapter 5 and shows that under certain circumstances cells that could not generate envelopes *can* do so when coupled with similar neurons. In that chapter we showed that a sufficient non-linearity for envelope extraction is signal rectification via a spike threshold non-linearity (123). This transformation results in a linear, or first-order, representation of the envelope as slow variations in the average firing rate. This representation of the envelope may then be decoded further on by linear means. Here we present a review of a phenomenological model of an oscillatory neuron, the phase oscillator (29), and of how to describe their intrinsic dynamics and the dynamics arising from coupling. We also describe the transformation of general time-varying inputs in the phase oscillator picture. The interaction of coupling dynamics and stimulus evoked dynamics leads to higher order temporal relationships between oscillators, namely stimulus-specific relative phase values. In addition, we show analytically and numerically that the dynamics we have

qualitatively described in the phase oscillator picture exists in certain parameter regimes in more realistic biophysical, coupled models. Extending work by Chow and Kopell (166) using the spike response method (SRM) (167) we show the same interplay between mutual phase coupling and stimulus-induced synchrony, leading to a stimulus-specific fixed point (i.e. a stable equilibrium point of the system dynamics) of the phase difference between two identical biophysical spiking neural models. Finally, using the same parameters shown by the theory to exhibit this effect, we quantify information transmission in the coupled neural models using the coherence, $C(f)$, function as a measure.

6.2 MODELS

6.2.1 LEAKY INTEGRATE-AND-FIRE (LIF) NEURON MODEL

The networks we are studying have membrane voltage dynamics, for the i^{th} neuron, of the form:

$$\dot{v}_i = F(v_i) + \sum_j^N G(v_i, v_j) + S(v_i, t) \tag{6.1}$$

where $F(v)$ is the intrinsic dynamics of a single neuron in the network describing both the subthreshold evolution of the membrane voltage and the spike-generating mechanism. The function $G(v_i, v_j)$ describes the coupling between i^{th} and j^{th} neurons in the network, assuming pair-wise interactions that can involve both subthreshold voltage coupling and spike coupling and $S(v_i, t)$ is the external time-dependent input signal. $S(v_i, t)$ typically describes a time-varying synaptic input driven by a voltage-dependent reversal potential However in the following study we will use simply a time-dependent input signal for

analytic tractability. In general, more detailed models have companion equations describing the dynamics of ion channels, contained in $F(v)$, which contribute to spike generation, such as in the Hodgkin-Huxley conductance based model (168). A simpler model, and one used in this study, accounts for spike generations by an explicit voltage reset once it has crossed a threshold value. In this way the neuron can display linear subthreshold dynamics and still produce spikes, qualitatively reproducing input-output firing relationships. The leaky integrate-and-fire neuron is the most common form of simplified thresholding neuron (19). Its dynamics are:

$$\dot{v} = -\frac{v}{\tau} + \mu + S(t) \tag{6.2}$$

where τ is the membrane time constant and μ is the current driving the voltage towards threshold. Every time the voltage reaches the threshold value v_{th} it is explicitly reset to another given value v_r. The first two terms in Eq. (6.2) along with the voltage reset correspond to $F(v)$ in Eq. (6.1).

6.2.2 PHASE OSCILLATOR MODEL

The dynamics in Eq (6.2) are more tractable than a general conductance based model, but often further simplifications can be made given certain assumptions about the firing patterns. The trajectory in the state space of the neuron from reset, through the characterized action potential and back to reset, can be transformed to a scalar variable, θ (29). With superthreshold dynamics a transformation that gives θ as a linear function of time, e.g. $\dot{\theta} = \omega t$, essentially maps the attracting limit cycle in the state space of the neuron onto a circle with uniform rotation. If the neuron is subthreshold or near a

bifurcation point, more care has to be taken to express the dynamics, as a phase variable usually involves transforming the normal form dynamics near the bifurcation (28). With this method the neuron can be represented as a phase oscillator even though a strong limit cycle may not be present.

Given the simple mapping of the limit cycle onto a phase variable the corresponding transformation of coupling terms between similar neurons into the phase state space are not necessarily as simple. A perturbative approach to the coupling dynamics may be used if the limit cycle of the individual neurons is strong and the mutual coupling is weak, giving corrections to the limit cycle due to small input currents averaged over time.

For the case of two mutually coupled neural oscillators we wish to obtain the transformation from the system

$$\begin{aligned} \dot{v}_1 &= F(v_1) + \varepsilon G(v_1, v_2) \\ \dot{v}_2 &= F(v_2) + \varepsilon G(v_2, v_1) \end{aligned} \tag{6.3}$$

to the system (29)

$$\begin{aligned} \dot{\theta}_1 &= \omega_1 + \varepsilon H(\theta_1, \theta_2) \\ \dot{\theta}_2 &= \omega_2 + \varepsilon H(\theta_2, \theta_1), \quad -\pi < \theta \leq \pi \end{aligned} \tag{6.4}$$

First we need to introduce the concept of a phase resetting curve (PRC). The PRC gives the linear response of the phase to brief weak input current pulses, namely the constant of proportionality between an infinitesimal input current pulse and the advance or delay of phase, θ. The PRC, or $P(t)$ to explicitly show the dependence on the relative time in the cycle, can have positive (phase advance) or negative (phase delay) values. For a continuous time current, $S(t)$, the instantaneous infinitesimal phase shift is given by

$$d\theta(t) = P(t)S(t)dt \tag{6.5}$$

so that the accumulated phase shift over a given period of time is given by

$$\Delta\theta = \int_t^{t+\Delta t} P(t')S(t')dt' . \tag{6.6}$$

If the phase shifts over this period of time are relatively small we associate the average value of this integral with a rate of change of phase due to the input $S(t)$:

$$\frac{d\theta}{dt} \simeq \frac{\Delta\theta}{\Delta t} = \frac{1}{T}\int_t^{t+T} P(t')S(t')dt' \tag{6.7}$$

where T is the period of the limit cycle. Note that this average is done over one period of the limit cycle, so that in this approximation $\Delta t \simeq T$.

Given a well defined attracting limit cycle, $v_o(t)$, with period T we can look at the relative phase shift that occurs at the end of one cycle due to the weak coupling $\varepsilon G(v_1, v_2)$. If v_2 starts ahead of v_1 by an amount $\phi = \theta_2 - \theta_1$ on the limit cycle $v_o(t)$ then the phase coupling term becomes:

$$\varepsilon H(\theta_1, \theta_2) \equiv \frac{d\theta}{dt} = \frac{\varepsilon}{T}\int_0^T P(t')G\big(v_o(t'), v_o(t' + \phi T/2\pi)\big)dt' \equiv \varepsilon H(\phi) \tag{6.8}$$

so that in this perturbative approach the coupling terms only come in through the difference of phases, ϕ, not their absolute values. In this way we can take the difference of the individual phase dynamics of Eqs. (6.4) to obtain the phase difference dynamics:

$$\dot{\phi} = \omega_2 - \omega_1 + \varepsilon H(-\phi) - \varepsilon H(\phi) \tag{6.9}$$

which can be re-written as

$$\dot{\phi} = \Omega - 2\varepsilon H_o(\phi), \quad -\pi < \phi \leq \pi \tag{6.10}$$

where $\Omega = \omega_2 - \omega_1$ is the frequency detuning between the two oscillators and $H_O(\phi)$ is the odd part of $H(\phi)$.

6.2.3 EFFECT OF TIME-VARYING SIGNALS

It then remains to be seen how time-varying inputs to the two neurons will affect the dynamics in the phase oscillator picture. If the signal is periodic, then the same method as used above can be applied, where the averaging is done over the larger of the two cycles. If there is a great disparity in the period of the signal and that of the intrinsic limit cycle then this method will not be as accurate a representation, as it requires that the phase difference does not change much over the period of integration. With this in mind we will assume that the periods of both the signals and the oscillators are similar. Given the input signal, $A(t)$, Eq. (6.6) can be used to determine the form of the coupling given a knowledge of the PRC. In this case however, the signal can be viewed as an autonomous oscillator and the argument of the coupling term gives the difference of the oscillator phase with respect to some absolute reference point.

We first present here a specific example of a PRC that will motivate the general form of the phase oscillator dynamics examined in the following section. For a leaky integrate-and-fire neuron with the dynamics in Eq. (6.2) the general solution of $v(t)$ is

$$v(t) = v_o e^{-t/\tau} + v^*(1 - e^{-t/\tau}) \tag{6.11}$$

where $v^* = \tau\mu$ is the equilibrium in the absence of a threshold. Given a threshold, v_{th}, and the initial condition at reset, $v_o = v_r$, Eq. (6.11) can be inverted to find the period of oscillation

$$T = -\tau \ln\left(\frac{\tau\mu - v_{th}}{\tau\mu - v_r}\right). \tag{6.12}$$

The effect that the infinitesimal current pulse, ε, has is to cause a jump in the voltage of height ε. The time it would have taken the system to reach that level naturally is the phase advance when expressed as a fraction of the entire period, T. Using Eq. (6.11) and given the endpoints v and $v+\varepsilon$ we can obtain the advance in time

$$\Delta t = -\tau \ln\left(1 - \frac{\varepsilon}{\tau\mu - v(t)}\right) \tag{6.13}$$

which can be expanded in small ε, resulting in

$$\Delta t \cong -\frac{\tau\varepsilon}{\tau\mu - v(t)}. \tag{6.14}$$

Inserting the time dependent solution for the voltage and dividing by the total current in the pulse we have the PRC

$$P(t) = \begin{cases} 2\pi \dfrac{\tau e^{t/\tau}}{T\left(\tau\mu - v_r\right)}, & 0 \le t \le T \\ 0, & t = 0, T \end{cases} \tag{6.15}$$

with the condition that $P(0)$ and $P(T)$ are both zero. This LIF PRC could be classified as being a type I PRC, i.e. one where positive inputs can cause only advances in phase, not delays. However, it differs from the type I PRCs of more realistic neuron models because of the discontinuity at $t = 0, T$.

We wish to show how the PRC can be used to describe the phenomenon of synchronization. Frequency synchronization is the process of locking the frequency of an oscillator to that of the driving signal, or an integer multiple thereof (169), while phase

synchronization occurs if additionally there is a fixed relative phase relationship that occurs (170). Synchronization is naturally described in the phase oscillator picture, so we will show how a transformation of the PRC to the phase oscillator picture leads to synchronization, given similar intrinsic and driving frequencies, as well as a PRC with functional dependence on ϕ. Synchronization is theoretically possible with any rational relationship between driving and entraining frequencies, but we will restrict ourselves to the simplest form, 1:1 synchronization. *For this reason we first examine the case when the external signal has the same frequency as the phase oscillators,* $\omega \simeq \omega_s$. Taking the case of the LIF and a sinusoidal input $S(t) = \varepsilon \sin(\omega_s t)$, where ε is assumed to be small, we can express the dynamics of the oscillator-signal pair as:

$$\begin{aligned} \dot{\theta} &= \omega + \varepsilon J(\theta_s - \theta) \\ \dot{\theta}_s &= \omega \end{aligned} \tag{6.16}$$

where θ_s is the phase of the input signal and the coupling can be expressed by substituting the PRC of the LIF, Eq. (6.15), in Eq. (6.7):

$$J(\theta_s - \theta) = \frac{2\pi\tau}{T^2(\tau\mu - v_r)} \int_0^T e^{t'/\tau} \sin(\omega_s t' + \theta_s - \theta) dt'. \tag{6.17}$$

Solving explicitly we have:

$$\frac{2\pi\tau^3\left(e^{T/\tau} - 1\right)}{T^3\left(\tau\mu - v_r\right)\left(1 + (2\pi\tau/T)^2\right)} \left(2\tau\pi \cos(\theta_s - \theta) - (T/\tau)\sin(\theta_s - \theta)\right). \tag{6.18}$$

Without loss of generality we can absorb the entire pre-factor into the impulse constant, ε, and use only a single oscillatory function (this simply requires a re-definition of the signal phase origin), giving a simple harmonic functional form.

The next step is to include a second phase oscillator in order to study the interplay between mutual coupling and signal forcing. The system of interest then has the form

$$\begin{aligned}\dot{\theta}_1 &= \omega_1 + \varepsilon_o H(\theta_2 - \theta_1) + \varepsilon_s J(\theta_s - \theta_1)\\ \dot{\theta}_2 &= \omega_2 + \varepsilon_o H(\theta_1 - \theta_2) + \varepsilon_s J(\theta_s - \theta_2)\\ \dot{\theta}_s &= \omega_s\end{aligned} \qquad (6.19)$$

Since we are now both describing inputs from mutual coupling and external signals, we henceforth us the subscripts 'o' and 's' to distinguish the amplitudes of these two sources, respectively.

6.3 RESULTS

6.3.1 PHASE OSCILLATOR ANALYTICS

In the previous section we reviewed how a neural oscillator can be mapped into a phase representation and how input from either coupled oscillators or external signals, provided they are weak enough, can be described by series of phase-difference dependent coupling terms. Assuming that this transformation is possible for an arbitrary neural model we will study the generic dynamics of the simplest forms of coupled phase oscillators receiving inputs. More specifically, we look at the interplay between input currents arising from mutual coupling and external signals and how the resultant dynamics affect the capability of these simple networks to process and transmit information in different forms.

It was shown (29) that only odd components in mutual coupling terms lead to phase synchronization, so for the phase coupling term we use the simplest anti-symmetric coupling term $H(\phi) = \varepsilon_o \sin(\phi)$ that leads to the dynamics $\dot{\phi} = 2\varepsilon_o \sin(\phi)$. This dynamics has stable fixed points at $\phi^* = 0, \pm 2\pi, \pm 4\pi, \ldots$ the stability of which is determined by the

sign of ε. As shown in the previous section, if the stimulus has a fundamental harmonic component at the same frequency of the neural oscillators, then it is possible to represent the input current in terms of a phase and time-dependent term. Adding the phase of the signal into the dynamics we have a 3-dimensional system where the oscillators are bi-directionally coupled and the signal is an extraneous oscillator unidirectionally coupled onto the oscillators. The absolute phase of the signal is irrelevant; this will only change the reference point of the relative phase between signal and oscillator. A signal term expressed as a difference of phases will only arise if there is some contracting region (i.e. a region in state space in which all initial conditions are attracted to a stable fixed point) in the vector field of the independent neural dynamics. In this case, we expect locking of the neural firing pattern to the stimulus (171-174).

Since the dynamics of θ_s is independent of the other phase variables, the state space of the system is effectively two-dimensional. The first change of variables, already presented, forms the phase difference $\phi = \theta_2 - \theta_1$. A second convenient state variable to introduce is $\alpha = \theta_s - (\theta_1 + \theta_2)/2$, which can be viewed as centre-of-mass-like coordinate which gives the mean value of the first two phases with respect to the autonomous signal phase. With this change of variables the dynamics becomes:

$$\dot{\phi} = \dot{\theta}_2 - \dot{\theta}_1 = \omega_2 - \omega_1 + 2\varepsilon_o \sin(\phi) + \varepsilon_s \left(\cos(\alpha - \frac{\phi}{2}) - \cos(\alpha + \frac{\phi}{2}) \right) \qquad (6.20)$$

and

$$\dot{\alpha} = \dot{\theta}_s - \frac{\dot{\theta}_1}{2} - \frac{\dot{\theta}_2}{2} = \omega_3 - \frac{\omega_1 + \omega_2}{2} - \varepsilon_s \left(\cos(\alpha - \frac{\phi}{2}) + \cos(\alpha + \frac{\phi}{2}) \right). \qquad (6.21)$$

Using trigonometric summation relationships the dynamics can be expressed as

$$\begin{aligned}\dot{\phi} &= \Omega_o + 2\varepsilon_o \sin(\phi) + \varepsilon_s \sin(\alpha)\, \sin\left(\frac{\phi}{2}\right) \\ \dot{\alpha} &= \Omega_s - \varepsilon_s \cos(\alpha)\, \cos\left(\frac{\phi}{2}\right)\end{aligned} \tag{6.22}$$

where $\Omega_o = \omega_2 - \omega_1$ is the detuning between the oscillators and $\Omega_s = \omega_s - (\omega_1 + \omega_2)/2$ is a measure of detuning between the signal and the oscillators.

Figure 6-1 A. shows the effective phase-difference potential, $V(\phi) = -\int \dot{\phi}(\phi) d\phi$, in the absence of stimulus, ε_s, showing a fixed point at $\phi^* = \pi$, the anti-synchronous state. Figure 6-1 B shows the effective potential in the absence of mutual coupling, but with stimulus present; here the stable fixed point is at $\phi^* = 0$. Because each neuron gets locked to the same phase with respect to the stimulus, provided the parameters are in the 1:1 mode-locking regime, the stable fixed point due to the stimulus will always be at zero.

Because these mutual coupling and stimulus coupling terms are additive terms in the dynamics, we can simply add the potentials together to see that the new fixed point in the mixed potential will be an intermediate value of phase difference illustrated in Fig. 6-1 C as the linear sum of the potentials in Fig. 6-1 A and B. It should be pointed out that, because of the common signal, the potential in phase difference is 4π periodic, not 2π periodic as in the case of only mutual coupling. This is because for a fixed phase center-of-mass the states $\phi^* = 0$ and $\phi^* = 2\pi$ represent different states: for every increment of ϕ, each oscillator phase increments by only $\pm\phi/2$ and thus after a phase difference shift

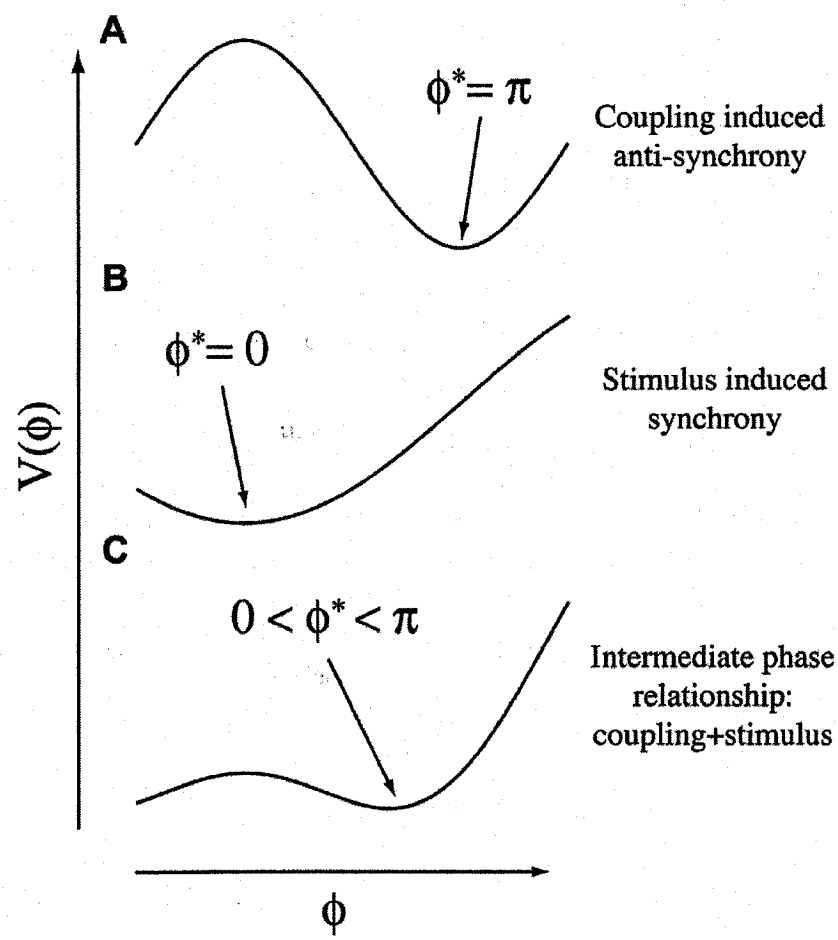

Figure 6-1: **A** The potential [from the anti-derivative of Eq. (6.22)]as a function of phase difference, ϕ, for coupled phase oscillators. For this particular coupling form the stable fixed point is at $\phi = \pi$, the out-of-phase solution. **B** In the absence of mutual coupling and with a common driving signal both neurons get locked to the same stimulus-relative phase, thus making the synchronous solution, $\phi = 0$ stable. **C** In the presence of both mutual coupling, leading to anti-synchronous oscillation, and common stimulus driving the stable fixed point will lie at some intermediate value.

of 2π each have moved π with respect to the external signal. This point is illustrated in Figs. 6-2 A and B. The value of the fixed point will depend on both coupling strength and the magnitude of the signal. In the context of narrowband signal processing, this result is important as it shows that for a given value of the envelope signal of a carrier, anti-synchronously coupled neurons will have a specific phase difference. This one-to-one correspondence of signal amplitude to phase difference can form the basis of a neural code. The input signal being coded for is the instantaneous value of the amplitude modulation of a fast carrier (the carrier frequency is entraining the neurons), and the output of the neural pair is their phase difference ϕ.

The transfer function for this input/output relationship can be obtained by solving the dynamics (6.22) for the fixed point of phase as a function of the signal amplitude. The stable fixed point of the center-of-mass variable, independent of phase difference is $\alpha^* = -\pi/2$. Substituting this into the first of equations (6.22) we can solve for, ϕ^*, to obtain

$$\phi^* = \cos^{-1}\left(\frac{a^2}{4} \pm \frac{1}{2}\sqrt{\frac{a^4}{4} - 2a^2 + 4}\right) \tag{6.23}$$

where the bifurcation parameter is the ratio of signal to coupling strength, $a = \varepsilon_s / \varepsilon_o$. Figure 6-3 shows a fixed point diagram where we see that the stable fixed point of the phase, ϕ^*, decreases in a monotonic fashion from $\phi^* = \pi$ to $\phi^* = 0$. In the full 2-dimensional phase space there are multiple allowable fixed points due to the periodicity

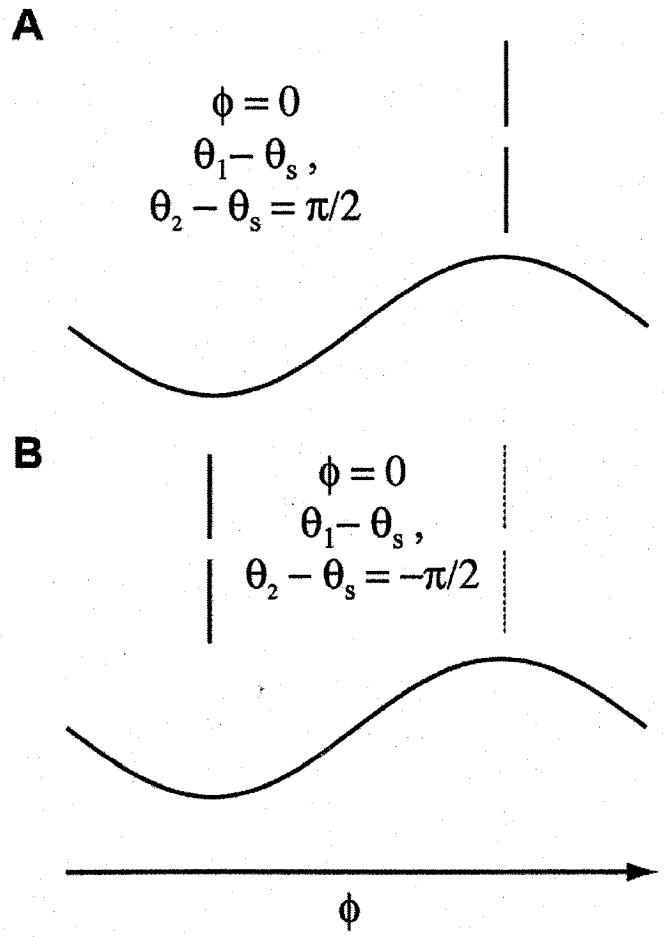

Figure 6-2: The fixed points for phase difference are degenerate with respect to the stimulus-relative phase. **A** The stable fixed point $\phi = 0$ with both oscillators being at the stimulus-relative phase $\theta_{1,2} - \theta_S = \pi / 2$. **B** The unstable fixed point $\phi = 0$ with both oscillators being at the stimulus-relative phase $\theta_{1,2} - \theta_S = -\pi / 2$.

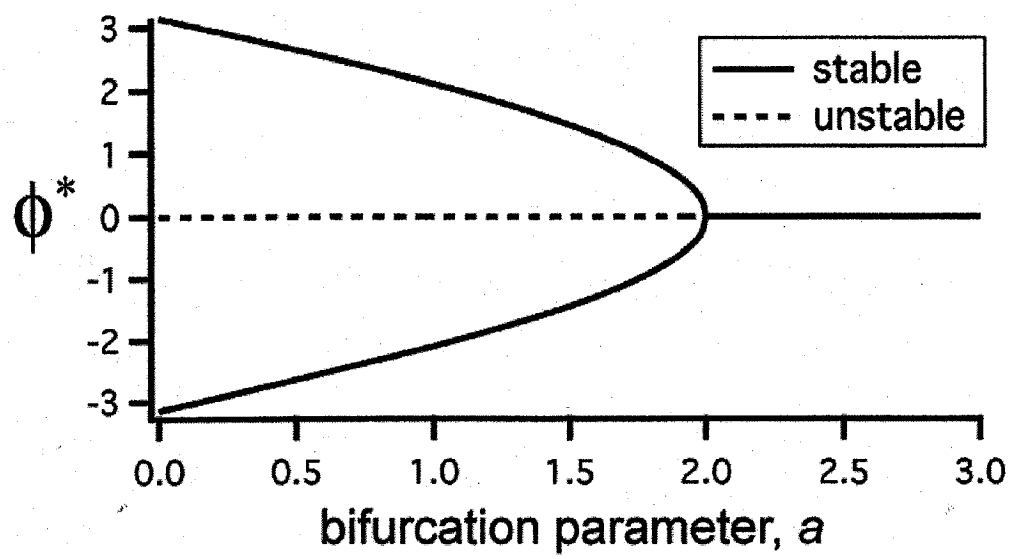

Figure 6-3: The fixed point diagram showing the dependence of the fixed points ϕ^* on the bifurcation parameter, $\varepsilon_s/\varepsilon_o$, which is the ratio of external signal strength to mutual coupling strength. The solid and dashed lines indicate stable and unstable fixed points respectively. From $|\phi^*| = \pi$ the magnitude of the stable fixed point decreases monotonically with increasing signal-to-coupling ratio. Past a pitchfork bifurcation (175) there is only a stable fixed point at $\phi^* = 0$. The detuning was set to zero, $\Omega = 0$.

of the dynamics. Figure 6-4 shows the 2-dimensional potential where the grayscale "dark to light" represents "low to high" values of the potential. The light coloured areas are basins of attractions with the minima being stable fixed points, while the maxima of the dark coloured areas are unstable fixed points.

6.3.2 LIF COUPLING WITH SPIKE RESPONSE METHOD (SRM)

Given that we have just shown that coupled phase oscillators and common inputs can influence the dynamics in such a way as to transmit information in higher order statistics of population firing, namely the signal dependent phase difference, it remains to be seen whether this type of phenomena exists in more biophysical neural models. To answer this question we will again return to the LIF. This model is still phenomenological in the sense that it accounts for action potential related currents in an artificial manner (19), but still retains the synaptic integration dynamics and spike timing. To study phase locking in LIFs we will build on the approach of Chow and Kopell (166), based on the spike response method (SRM) (167).

The SRM is a phenomenological, non-dynamical description of neural membrane that takes into account two important properties of neural activity: spiking and synaptic integration. The membrane voltage is determined by a kernel response to unitary events: synaptic inputs and voltage threshold crossings. In a network of coupled neurons the SRM equation describing the i^{th} membrane voltage is

$$v_i(t) = \eta(t-\hat{t}_i) + \sum_j \omega_{ij} \sum_f \varepsilon_{ij}\left(t-\hat{t}_i, t-t^{(f)}{}_j\right) + \int_0^\infty \kappa(t-\hat{t}_i, s) I^{\text{ext}}(t-s)ds. \qquad (6.24)$$

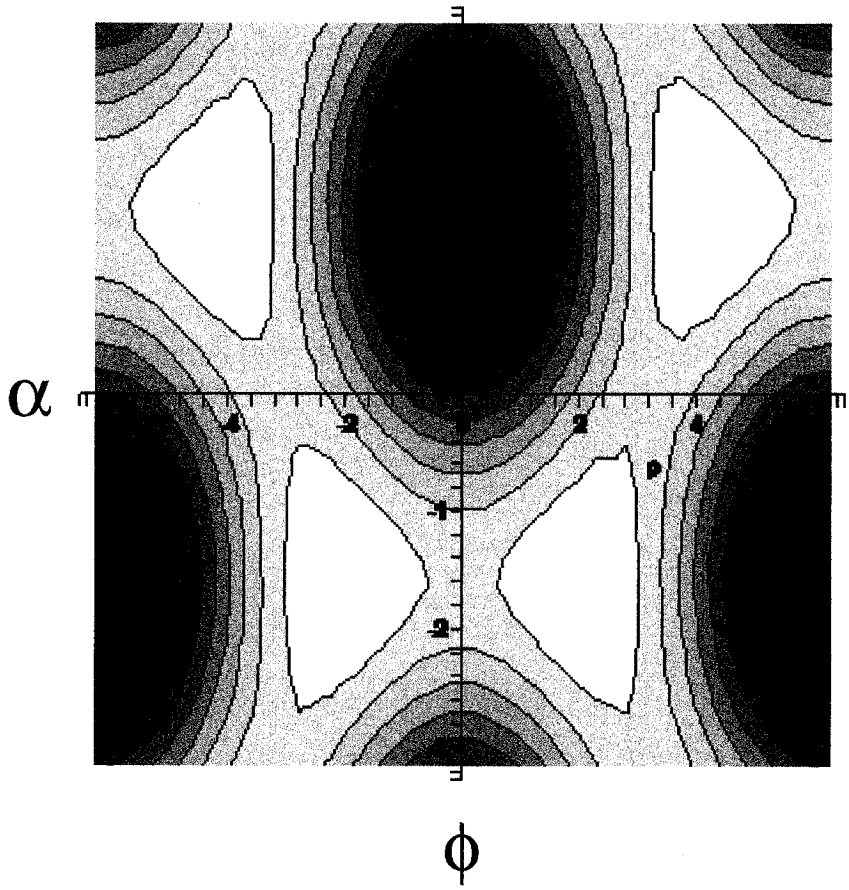

Figure 6-4: A contour plot of the potential landscape of the coupled phase oscillators in the reduced variable space (ϕ, α). The grayscale from white to black corresponds to the transition from high to low values of the potential.

where $\hat{t}_i$ is the previous spike time for the i^{th} neuron. Here $\varepsilon_{ij}\left(t-\hat{t}_i, t-t^{(f)}{}_j\right)$ is the kernel that determines the voltage resulting from a synaptic input from the f^{th} spike of the j^{th} neuron. In general the response to external inputs can depend on the neuron's own spiking memory; this is taken into account by the dependence on the relative time since the neuron's last spike time $t-\hat{t}_i$. The kernel $\kappa(t-\hat{t}_i, s)$, describes the effect of a generalized continuous-time input signal coming from sources other than neighbouring neurons. The function $\eta(t-\hat{t}_i)$ describes the excursion of the voltage during a spike, the after-hyperpolarization and the recovery to rest following a threshold crossing.

In the case of a sinusoidally driven LIF, we can obtain the SRM kernels and resultant voltage equations by integrating the dynamics to obtain formal solutions. Important for the subsequent discussion of driven, coupled neurons is the solution for the fixed point in relative phase between the input signal and the threshold crossing times, namely to show that the proposed form of neural coding in phase oscillators holds for coupled spiking neurons as well. For the LIF we have, for the dynamics

$$\dot{v} = -v/\tau + \mu + \varepsilon_s \cos(2\pi t/T + \psi) \tag{6.25}$$

where a is the signal amplitude, ψ is the relative phase between the external signal and the oscillation of the neuron (defined by the spike times), and T is the signal period. As in section 6.2, we choose a signal with the same frequency of oscillation as the neuron, i.e. $T = 2\pi/\omega_s$. Integrating this equation we have

$$v(t,\psi) = \mu\tau(1-e^{-t/\tau}) + \varepsilon_s \int_0^t e^{-(t-s)/\tau} \cos(2\pi s/T + \psi) ds \tag{6.26}$$

where the first term on the right hand side is the familiar spike recovery kernel, $\eta(t)$, and the exponential being convolved with the stimulus is the signal response kernel, $\kappa(t-s)$. The integral can be evaluated to obtain a tractable expression coupled with the condition that the period of forcing is the same, or near the spontaneous period of firing, allowing us to solve for the fixed relative phase of input to threshold crossing. Given that the neuron spiked at $t=0$, it should also spike one period later

$$v(0,\psi)=1=v(T,\psi) \tag{6.27}$$

The roots to the equation $v(0,\psi)-v(T,\psi)=0$ in term of ψ can be numerically obtained. In general for periodic forcing there will be two roots to this equation, the physical one being the phase that gives threshold crossings from below, i.e. $v'(0,\psi)>0$.

The following solution of the stable phase difference between two coupled LIF neurons in the absence of an external signal consisting of Eqs. (6.28)-(6.37) is reproduced from reference (166) for completeness. After these results are reviewed we will then combine them with the results of stimulus-induced synchrony as we did with the phase oscillators in section 6.2. A network of two LIF neurons coupled via gap junctions, i.e. electrically coupled can be described by the equations:

$$\begin{aligned}\dot{v}_2(t)&=I_1-v_1-g(v_1-v_2)+\sum_l A(t-t_1^l)\\ \dot{v}_1(t)&=I_2-v_2-g(v_2-v_1)+\sum_l A(t-t_2^l)\end{aligned} \tag{6.28}$$

where $A(t)$ is the derivative of the spike response kernel, $\eta(t)$, introduced above. This description is not completely in the SRM formalism as the RHS of equation (6.28) still depends explicitly on voltage. In order to make this dependence implicit and obtain

kernels based in the SRM formalism and describing the electrical coupling terms, a change of coordinates transformation into normal modes, $v_+ = v_1 + v_2$ and $v_- = v_1 - v_2$, must be performed. The system dynamics then becomes:

$$\begin{aligned} \dot{v}_+(t) &= I_+ - v_+ + \sum_l A(t - t_1^l) + \sum_m A(t - t_2^m) \\ \dot{v}_-(t) &= I_- - rv_- + \sum_l A(t - t_1^l) - \sum_m A(t - t_2^m) \end{aligned} \tag{6.29}$$

where $r = 1 + 2g$, $I_+ = I_1 + I_2$ and $I_- = I_1 - I_2$. Integrating Eq. (6.29) to obtain formal solutions to the normal mode variables:

$$\begin{aligned} v_+(t) &= I_+\left(1 - e^{-t}\right) + \sum_l \eta_+\left(t - t_1^l\right) + \sum_m \eta_+\left(t - t_1^m\right) \\ v_-(t) &= \frac{I_-}{r}\left(1 - e^{-rt}\right) + \sum_l \eta_-\left(t - t_1^l\right) - \sum_m \eta_-\left(t - t_1^m\right) \end{aligned} \tag{6.30}$$

and transforming back into the original coordinate system, the SRM equations for gap junction-coupled neural voltage membranes become:

$$\begin{aligned} v_1(t) &= \hat{I}_1 + \sum_l \gamma_s(t - t_1^l) + \sum_m \gamma_c(t - t_2^m) \\ v_2(t) &= \hat{I}_2 + \sum_l \gamma_s(t - t_2^l) + \sum_m \gamma_c(t - t_1^m) \end{aligned} \tag{6.31}$$

where

$$\begin{aligned} \hat{I}_1 &= \frac{1}{2}\left[\left(1 + \frac{1}{r}\right)I_1 + \left(1 - \frac{1}{r}\right)I_2\right] \\ \hat{I}_2 &= \frac{1}{2}\left[\left(1 - \frac{1}{r}\right)I_1 + \left(1 + \frac{1}{r}\right)I_2\right] \end{aligned} \tag{6.32}$$

and

$$\gamma_s = \frac{1}{2}[\eta_+(t) + \eta_-(t)]$$
$$\gamma_c = \frac{1}{2}[\eta_+(t) - \eta_-(t)] \tag{6.33}$$

To assess whether or not the neurons will display stable phase locking, the first neuron is assumed to fire, without loss of generality, ahead of the second neuron. If the first neuron fires at time zero, it is at the threshold, and a fixed time later, $t = \phi T$, the second neuron will fire. Given these conditions, the difference of the two voltages gives equations whose roots, if they exist, are the stable phase differences between the two cells. We have:

$$v_1(0) - v_2(\phi T) = 0 = \hat{I}_1 - \hat{I}_2 - G(\phi, T) \tag{6.34}$$

with

$$G(\phi, T) = \gamma_c(\phi T) + \sum_{l \geq 1}[\gamma_c(lT + \phi T) - \gamma_c(lT - \phi T)]. \tag{6.35}$$

This gives the condition for a stable phase difference given a period of oscillation, T. The complementary equation, obtained by taking the arithmetic mean of the two voltages, gives a solution for the period of firing, for a given phase difference. The two equations, solved self-consistently allow a solution for both phase difference and period. Eq. (6.35) can be summed to obtain a closed form solution for the LIF model

$$G(\phi, T) = \gamma_c(\phi T) - \frac{1}{2}\left[\frac{e^{-(T+\phi T-\Delta)} - e^{-(T-\phi T-\Delta)}}{1-e^{-T}} - \delta_c \frac{e^{-r(T+\phi T-\Delta)} - e^{-r(T-\phi T-\Delta)}}{1-e^{-rT}}\right], \quad \phi T \leq \Delta \tag{6.36}$$

$$G(\phi,T) = -\frac{1}{2}\left[\frac{e^{-(\phi T-\Delta)} - e^{-(T-\phi T-\Delta)}}{1-e^{-T}} - \delta_c \frac{e^{-r(\phi T-\Delta)} - e^{-r(T-\phi T-\Delta)}}{1-e^{-rT}}\right], \quad \Delta < \phi T \le T \tag{6.37}$$

The roots to these equations, for specific values of T, give the solutions to fixed points of phase difference. Zero crossings of this function with positive slopes are stable fixed points, and it can be shown that this function is equivalent to a phase coupling term (176).

The fixed-point diagram shows complicated behaviour with different parameter regimes displaying stable synchrony, anti-synchrony, bi-stability or even phase-locking with intermediate phases; for more examples see Chow and Kopell (166). We are interested in the dynamics of anti-synchronously coupled cells, motivated by the results with phase oscillators in section 6.3 of this thesis, so we will use the parameter regime where the width of the spike, and thus the influence it has on the subthreshold dynamics, vanishes. In this regime where spike width is very small compared to the period of oscillation, the anti-synchronous state was predominantly attracting.

To incorporate the effects of stimulus-induced synchrony, we extend the same approach as Chow and Kopell but add the contribution to the voltage from the stimulus given by the stimulus response term in Eq. (6.26). Taking the difference in voltages again to obtain a phase coupling term, also dependent on relative stimulus phase ψ, we obtain a new phase coupling function (not shown due to its lengthiness). This is a first order correction to the case of isolated, coupled neurons. Ideally one would take into account the stimulus terms when obtaining the SRM kernels $\gamma_c(t)$ and $\gamma_s(t)$ of Eq. (6.33). Here we make the ansatz that one of the neurons will be at the preferred phase relative to the

stimulus, ψ, in the absence of coupling, given by the positive going root of (6.26), and the other at ϕ away from this phase. Numerically solving for the roots of the corrected phase coupling function we obtain fixed phase differences for the neurons.

In Fig. 6-5 we show the results from the analytic expression of fixed phase difference as a function of stimulus amplitude plotted (solid line), with good agreement, to the results of numerical simulations of coupled LIFs with the same parameters. This curve shows the competing effects of stimulus induced synchrony and coupling induced anti-synchrony; for smaller signal strengths the phase difference is closer to 0.5 (here the domain of the phase has been normalized from $[0,2\pi]$ to [0,1]), decreasing with increasing stimulus amplitude as the signal entrains the neurons and pushes them closer into synchrony. This shows that a biophysical, spiking neuronal model can exhibit this phenomenon as well as the phenomenological coupled phase oscillator model in Eq. (6.19).

This result was obtained in a deterministic setting, which leads to the question of the effects of noise on the stability of the phase difference fixed point. The brain is a noisy environment and thus for the amplitude-phase relationship to constitute a useful neural code it must be somewhat robust to the effects of noise. We show this qualitatively in Fig. 6-6 where the panels display the time sequence of phase differences (evaluated at the spike times of a single reference neuron) as well as the amplitude of the entraining harmonic signal, for increasing values of noise. Since noise induced phase slippings are possible we use a wrapped phase [i.e. $\mathrm{mod}(\theta,2\pi)$]. We see that after 2 orders of magnitude when the noise intensity reaches $D=10^{-3}$ the correlation starts to degrade. In

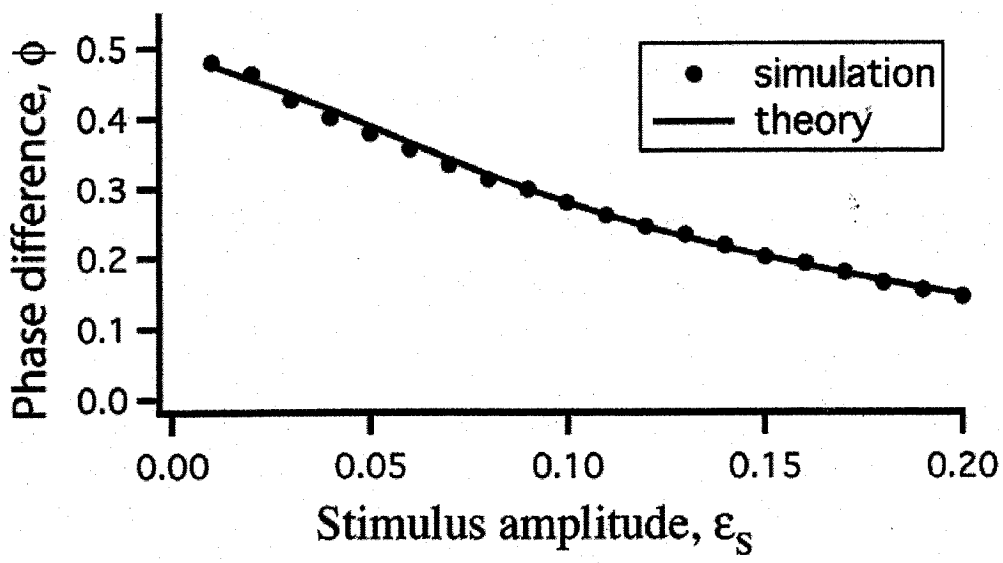

Figure 6-5: The stable fixed point in phase difference, ϕ, of two electrically coupled LIF neurons with common stimulus, at their resonant frequency, as a function of stimulus amplitude, ε_S. The analytic solution from SRM (6.36) and (6.37) taking into account mutual stimulus-induced synchronization is shown in the solid line. This shows good agreement to results from numerical simulations (circles) of the LIF neuron. The monotonic relationship between stimulus amplitude and phase difference indicates that this could be a useful variable to transmit information on the stimulus amplitude.

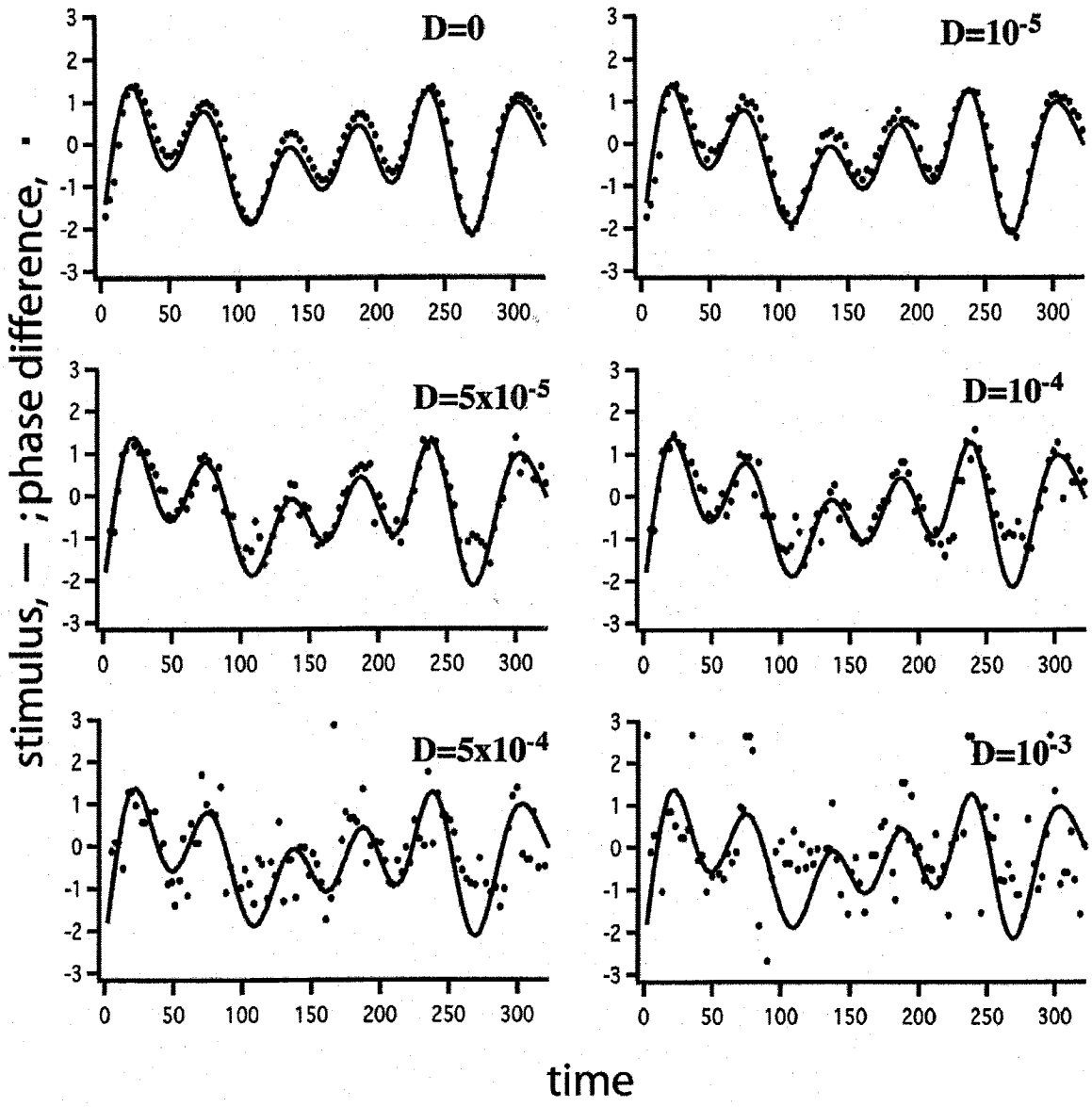

Figure 6-6: The effects of independent internal additive noise on phase difference coding in coupled LIF neurons. Two LIF neurons are receiving a common amplitude modulated sinusoidal forcing. These plots show the stimulus (solid line) and the sequence of instantaneous phase differences (dots), observed at the spiking times of one neuron. As the intrinsic noise intensity is increased (left to right, top to bottom) the representation of the modulation by phase difference is gradually degraded. The parameters used are $\mu = 0.1$ and $\tau = 10$.

higher noise settings, population averaging of coupled cells may be required to maintain lower signal-to-noise ratio.

We can also examine the effect the coupling strength, g, has on input/output relationship between signal amplitude, A, and phase difference, ϕ. For noise intensity, $D = 10^{-5}$, Figs. 6-7 A-C show scatter plots for phase difference versus instantaneous signal amplitude from numerical simulations for electrical coupling strengths $g = 0.0,\ 0.4,$ and 1.5 respectively. In the case of no coupling (Fig. 6-7 A) we can see that there is no effective input/output relationship in terms of the phase difference. This makes sense as the two neurons are independent of each other except via the stimulus; with respect to the phase potential picture of Fig. 6-1, the anti-synchronous attractor is removed. For an intermediate coupling strength ($g = 0.4$, Fig. 6-7 B) we can see that the points collapse onto an amplitude dependent phase difference allowing for a one-to-one input output relationship. For even higher coupling strengths ($g = 1.5$, Fig. 6-7 C) a larger fraction of the points fall along the $\phi = 0$ line. It has been shown that strong gap junction coupling promotes synchrony in theory, simulations and experiments (164, 165, 176). For larger coupling strengths the graded one-to-one relationship we see between phase difference and amplitude is removed because the phase difference goes to zero. To quantify the efficiency of the phase difference code, we calculated the correlation coefficient between the signal amplitude and phase difference,

$$C_{\varepsilon_S \phi} = \frac{\langle \varepsilon_S \phi \rangle}{\sqrt{\langle \varepsilon_S \rangle} \sqrt{\phi}} \tag{6.38}$$

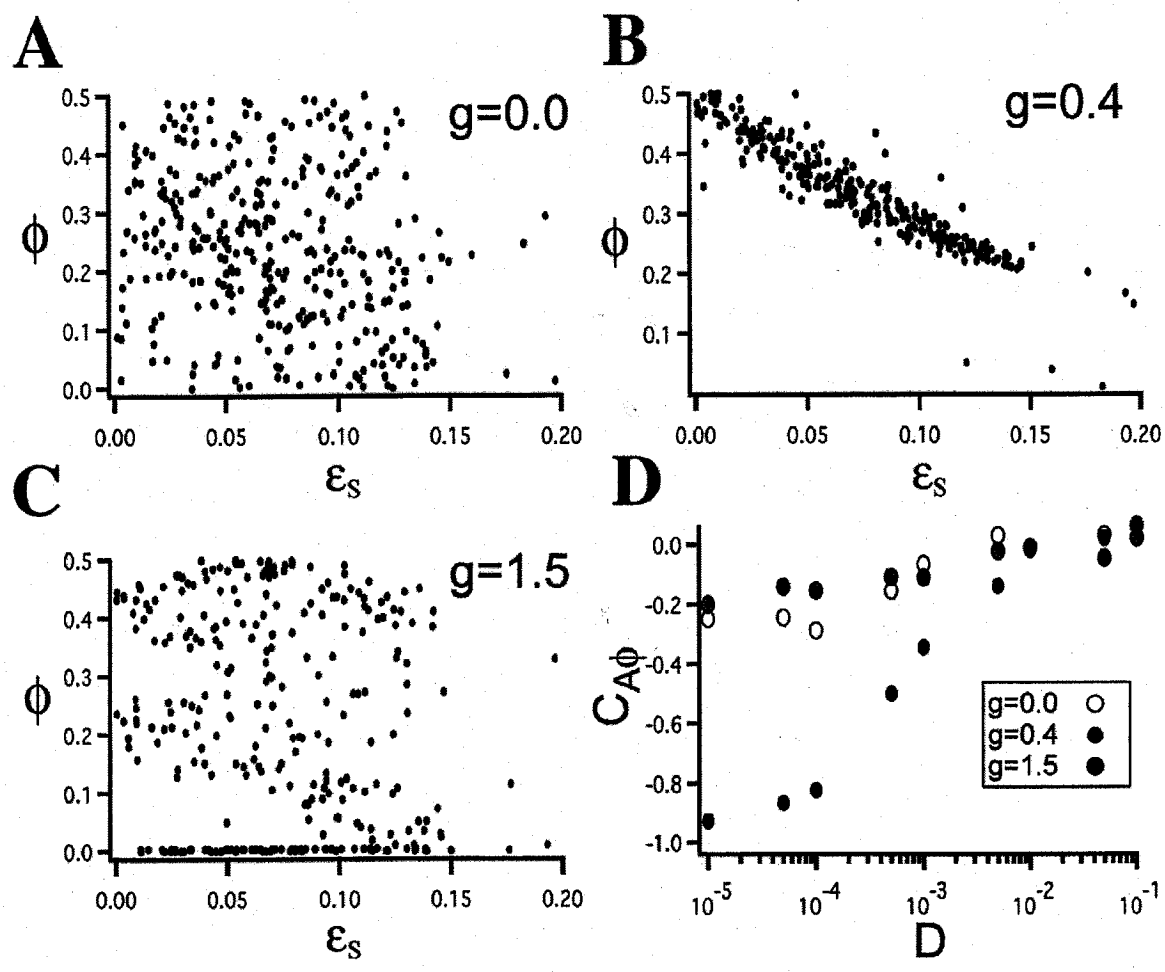

Figure 6-7: The effects of coupling strength on phase-difference coding of an input signal in LIF neurons. **A** In the absence of coupling there is no preferred phase difference between the neurons with weak internal noise. **B** For an intermediate value of coupling (one that allows stability of the anti-synchronous solution) there is a well-defined one-to-one relationship between phase difference and stimulus amplitude. **C** Large electrical coupling promotes synchrony (165, 176) and thus more sampled phase differences are at zero independent of the instantaneous stimulus amplitude. **D** The correlation coefficient between phase difference and stimulus amplitude for the coupling strengths shown in **A, B, C**. Strong anti-correlation only occurs for intermediate coupling strengths with lower levels of noise. Only under these conditions is phase-difference coding of the stimulus amplitude feasible, i.e. when $\left|C_{\varepsilon_S\phi}\right|$ is large.

where the brackets indicate a double average over both ε_s and ϕ. Figure 6-7 D shows the correlation coefficient for coupling strengths in Fig. 6-7 A-C as a function of noise intensity. For the high and low coupling cases, the correlation starts from a low magnitude level and decreases even further with increasing noise. For the intermediate coupling case, the input-output correlation is very good (close to -1) for vanishing noise intensities and decreases in magnitude with noise becoming indistinguishable from the other coupling scenarios past $D = 10^{-2}$. The noise does not change the effective phase potential, but does increase the spread of the probability density around the minimum, decrease the magnitude of correlation.

We have shown that coupled neurons in the superthreshold (oscillatory) regime are able to code for stimulus envelope through their phase differences. This differs from subthreshold or perithreshold neurons coding for narrowband stimulus envelopes with slowly time varying firing rates, as we have shown in chapter 5. In the coupled superthreshold this amounts to a novel form of parallel transmission of linear and non-linear stimulus features. We previously showed how separate channels consisting of physically distinct neurons transmit a stimulus and its envelope through a network (44), which ultimately arose from linear coding of envelope and direct signal in different frequency bands of the neural firing rate (44).

Here we have displayed the potential for parallel transmission of first and higher order features of the stimulus in parallel channels of a different nature; instead of the parallel channels being distinct cells, or different frequency bandwidths of the firing rate power spectral density, the channels are different order statistics of the spike train, i.e.

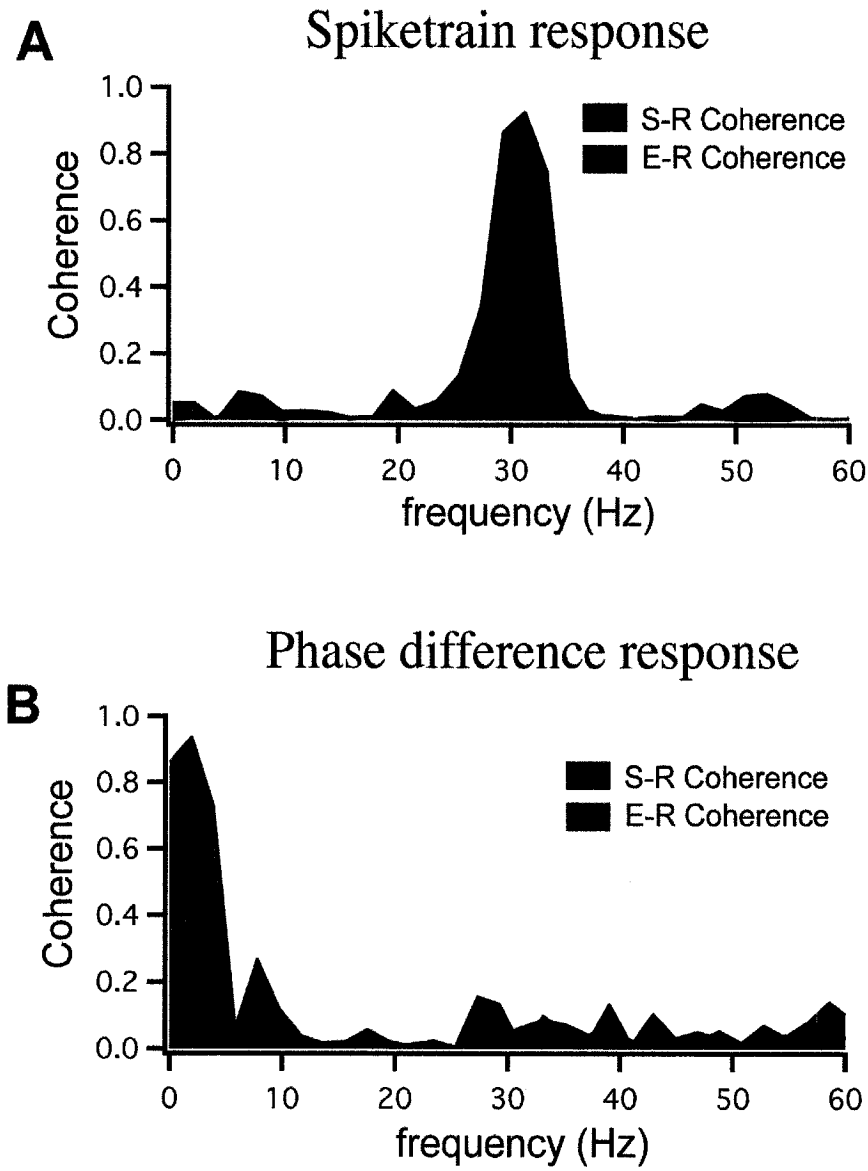

Figure 6-8: Coding of coupled LIF neurons for a 25-35 Hz narrowband signal and its envelope, with $D = 10^{-5}$ and $g = 0.4$. **A** The response of the summed spike train of the coupled neurons as measured by the coherence function. The spike trains do not significantly code for the stimulus envelope (red), while they do code for the stimulus itself (blue). **B** The response of the phase-difference between the coupled neurons as measured by the coherence function. The phase difference responds well to the stimulus envelope (red), while it does not code for the stimulus itself (blue).

first order statistics of the firing rate versus second order statistics of the relative spike times, which may be then separately decoded by different mechanisms. To illustrate this Fig. 6-8 A shows the coherence between the summed spike trains of the two neurons and a carrier input at 30 Hz modulated with a 0-5 Hz stimulus. In blue is the coherence between the direct signal and the summed spike train and in red is the coherence between the stimulus envelope and the summed spike train. Figure 6-8 B shows the same response functions but now with respect to the instantaneous, time-varying phase difference signals: spike times and relative spike time. We see distinct signals being transmitted through these channels: linear stimulus and stimulus envelope.

6.4 DISCUSSION

We have shown how cells, which by themselves have no capability to convey direct information about higher order stimulus features due to their non-excitability (123), can convey this information through precise relative timing of spikes with respect to those of cells they are coupled to. This effect arises due to the competing effects of stimulus-induced synchrony and a tendency for anti-synchrony arising from precisely tuned coupling. The stimuli leading to the synchronization of the coupled cells is narrowband in nature, a characteristic of many oscillations observed in the brain (50, 149, 177). These theories would have to be tested by multiple unit recordings in coupled cells *in vivo*. Another possibility would be to do simulate networks *in vitro* with iterated recordings and stimulation on a single cell (159).

CHAPTER 7: CONCLUSION

This thesis has two distinct sections:

I. Chapters 2 and 3 study how correlations in neural inputs shape output spike train correlations and furthermore how this affects signal transmission at plastic synapses.

II. Chapters 4-6 study the processing of envelopes of narrowband signals in the context of networks and single cells, both in the excitable and non-excitable firing regimes.

I will discuss how the results within each section relate to one another and end with some final thoughts on the representation of temporal stimulus features in neural spike trains and their decoding.

7.1 ISI STATISTICS AND TEMPORAL FILTERING

Temporal correlations are widely observed in signals throughout the brain, whether they are single neuron spike trains, synaptic currents, or more macroscopic signals such as field potentials, electroencephalograms (EEGs) or magnetoencephalograms (MEGs). The OU process is widely used as a starting point in studying the influence of temporally structured signals (20) because it is defined by a single time constant. In chapter 2 we developed analytical expressions describing how temporal correlations in neural inputs translate into output spike train statistics. Using a quasistatic approximation of the input noise, contingent on the separation of timescales of input signal and output firing rate, we can use conditional probability densities to obtain approximations for the stationary probability densities of ISIs, and serial correlations in ISI sequences.

Information is transmitted from one neuron to another through synapses. The dynamics of synaptic transmission determine the amount of information passed on to the

postsynaptic neuron. Plasticity, a property whereby repeated synaptic transmissions caused a change in the efficacy of the synaptic transmission itself, is common to many synapses. Facilitation and depression are forms of plasticity where repeated transmission of events causes an increase in the magnitude of currents through the post-synaptic membrane. In chapter 3 we show that if sensory signals are conveyed as modulations of the firing rate around a constant mean value, the roles of depression and facilitation are reversed. Analytic expressions are developed showing that the mean level of plasticity is dependent on the frequency of rate modulation coming from the pre-synaptic spike train. We then use numerical simulations of two LIF neurons connected by a plastic synapse to show that in addition to the mean level of post-synaptic current, there is also additional frequency dependent filtering present.

The results from chapter 2 directly motivate the study of temporal filtering in chapter 3. The representation of temporally correlated inputs by spike trains with highly correlated ISI sequences will determine the time varying inputs to successive neurons. In the context studied, i.e. superthreshold neurons driven by slow noise, depression and facilitation filter out low frequency and high frequency information, respectively. This type of processing may have important implications for guiding behaviour or perception, as it has been shown in several systems how behaviourally distinct natural stimuli occupy different bandwidths (42, 44, 178, 179).

7.2 NARROWBAND ENVELOPES: SINGLE CELL AND NETWORK PROCESSING

In the latter part of the thesis (chapters 4, 5 and 6) we uncovered single cell properties and network structure leading to the processing of the temporal envelopes of narrowband signals.

In chapter 4 we obtain single neuron recordings *in vivo* in weakly electric fish from multiple cell types in the ELL and associated feedback structures. We uncovered the cell type responsible for the extraction of signal envelopes from narrowband sensory stimuli. The network structure proved interesting, as it was a single inhibitory interneuron responsible for the envelope extraction, and transmitting it to primary neurons, parallel to the original signal itself. This form of parallel processing has been speculated to be responsible for cue-invariant responses in cortical neurons (103). This discovery led to the work in chapter 5 where we study the biophysical, single cell, mechanism responsible for envelope extraction. The nonlinearity in the F-I curve transfer function was shown to be sufficient for this task. We then hypothesized a novel form of noise shaping whereby increasing the level of independent uncorrelated noise in a population of neurons with ongoing background, narrowband inputs can increase the signal-to-noise ratio of additional harmonic inputs in the envelope frequency range.

These findings support that idea that neurons with average input currents that position them near the rheosbase of their F-I curve would be well suited to take the envelope from a narrowband input and represent the envelope of this signal directly in its time-varying firing rate. Primary cortical neurons seem to have the appropriate firing characteristics

(37); as well, they have been shown to respond to the envelopes of narrowband sensory stimuli (48, 127). One may then ask what role fast spiking neurons with regular ISI statistics (i.e. well above rheobase) might play in the transmission of envelope signals. Cortical interneurons often fire at fast rates, and are also coupled with gap junctions (164). This motivated the study in chapter 6 where we examined how coupling between superthreshold spiking neurons could modulate the statistics of their relative spike times.

Using a phase oscillator description of oscillating neurons and then a more biophysical neural model, the LIF, we show how coupled neurons can represent the envelope of a common narrowband input in their phase difference, when their coupling led to anti-synchronous firing in the absence of inputs. It is interesting to think of this result in terms of parallel transmission of stimulus features through different orders of spike train statistics. In chapter 4 we had the transmission of a narrowband signal and its envelope through two distinct neural pathways. Here we have shown that the narrowband signal and its envelope can be represented through the average instantaneous firing rate of the coupled cells and their time-varying phase difference, respectively. It would be interesting, as a further study, to see what types of decoding mechanisms can be used to exclusively draw information from one of these signals only.

Chapter 6 presents a speculative form of envelope coding that motivates a closer examination of the role of higher-order spiking statistics in conveying information about stimulus envelopes in the cortex.

7.3 FINAL THOUGHTS

This thesis dealt with the representation of signals and stimulus features in the spiking output of real neurons. Through a combination of statistical and mathematical theory, numerical simulations and electrophysiology experiments we look at how the output spike sequences, or spike trains, are influenced by the temporal structure of the different types of inputs. We further showed in a specific case how a behaviourally relevant temporal feature was expressed in the spiking activity in networks of neurons in the ELL in chapter 4. Temporally precise patterns of spike trains has been observed in binaural sound localization (180), and in stimulus specific spike patterns in auditory cortex (43, 181, 182) in response to same-species vocalizations. Neurons in the visual cortex also respond to visual stimuli with precisely timed spikes (183). Using RR-coherence it can be shown that temporally precise spikes can be used to transmit more information about the stimulus than firing rates alone, even when the spike precision time scales differ from those of the stimulus. It is an interesting question to ask what stimulus features are related to spike train properties. We have shown how envelopes of narrowband signals lead to slow variations in firing frequency of neurons that encode them under certain circumstances. We also develop a potential coding mechanism whereby the precise temporal relationship between spike times, in particular their phase difference, in coupled neurons can be used to code for the same information without it being represented in the averaged firing rate.

We have dealt with the encoding of signals in spike trains throughout this thesis; how statistical and temporal properties of inputs shape output spike trains and affect information transmission. Further work must be done to understand how the information transmitted

can be decoded by higher brain centers. This is the ultimate goal if one wishes to understand how these stimulus features and their specific representation in spike trains of intermediate neurons guide behavioural output. Recent work has shown how specific models of synaptic plasticity can respond to and classify a wide range of temporally precise multi-neuronal spike patterns (184). An emerging theme in the study of noisy neural dynamics is how noise can gate the flow of information in the brain (185). The work presented here fits in that framework, as we have characterized the effects of noise on several neural models, and shown how they influence information flow. Potential future work may involve integrating these separate components together. Eventually this may ultimately help in understanding stimulus-driven behavioral output; this thesis is a modest step towards that exciting goal.

REFERENCES

1. Cajal, S. R. y. (1911) *Histologie du système nerveux de l'homme et des vertébrés.* (Maloine, Paris).

2. Kandel, E. R., Schwartz, J. H. & Jessel, T. M. (2000) *Principles of Neural Science* (McGraw-Hill, New York).

3. Nicholls, J. G., Martin, A. R. & Wallace, B. G. (1992) *From neuron to brain* (Sinauer Associates, Inc., Sunderland, Mass.).

4. Laurent, G. (2002) *Nat Rev Neurosci* **3,** 884-95.

5. Singer, W. & Gray, C. M. (1995) *Annu Rev Neurosci* **18,** 555-86.

6. Heilengenberg, W. (1991) *Neural nets in electric fish* (MIT Press, Cambridge MA).

7. Lissmann, H. W. (1951) *Nature* **167,** 201-202.

8. Hopkins, C. D. (1999) *J Exp Biol* **202,** 1217-28.

9. Saunders, J. & Bastian, J. (1984) *J Comp Physiol [A]* **154,** 199-209.

10. Lissmann, H. W. (1958) *J Exp Biol* **35.**

11. Lissmann, H. W. & Machin, K. E. (1958) *J Exp Biol* **35,** 457-486.

12. Krahe, R. & Gabbiani, F. (2004) *Nat Rev Neurosci* **5,** 13-23.

13. Hodgkin, A. L. & Huxley, A. F. (1952) *J Physiol* **117,** 500-44.

14. Fatt, P. & Katz, B. (1952) *J Physiol* **117,** 109-28.

15. Katz, B. & Miledi, R. (1972) *J Physiol* **224,** 665-99.

16. Hille, B. (1992) *Ionic channels of excitable membranes* (Sinauer Associates, Sunderlan MA).

17. Koch, C. (1999) *Biophysics of computation* (Oxford UP, New York).

18. Wang, X. J. & Buzsaki, G. (1996) *J Neurosci* **16,** 6402-13.

19. Lapicque, L. (1907) *J Physiol Pathol Gen* **9,** 620-635.

20. Tuckwell, H. C. (1989) *Stochastic processes in the neurosciences* (SIAM, Philadelpia, PA).

21. Diba, K., Lester, H. A. & Koch, C. (2004) *J Neurosci* **24,** 9723-33.

22. Capocelli, R. M. & Ricciardi, L. M. (1971) *Kybernetik* **8,** 214-23.

23. Stein, R. B. (1965) *Biophys J* **5,** 173-94.

24. Papoulis, A. & Pillai, S. U. (2002) *Probability, random variables and stochastic processes* (McGraw-Hill, New York).

25. Lindner, B. (2006) *Phys Rev E Stat Nonlin Soft Matter Phys* **73,** 022901.

26. Gardiner, C. W. (1985) *Handbook of stochastic methods: for physics, chemistry and the natural sciences* (Springer-Verlag, Berlin).

27. Risken, H. (1996) *The Fokker-Planck Equation: Methods of solutions and applications* (Springer-Verlag, Berlin).

28. Ermentrout, B. (1996) *Neural Comput* **8,** 979-1001.

29. Kopell, N. & Ermentrout, B. (2002) in *Handbook on dynamical systems: toward applications*, ed. Fiedler, B. (Elsevier, pp. 3-54.

30. Gutkin, B. S. & Ermentrout, G. B. (1998) *Neural Comput* **10,** 1047-65.

31. Lindner, B., Longtin, A. & Bulsara, A. (2003) *Neural Comput* **15,** 1760-87.

32. Destexhe, A. & Marder, E. (2004) *Nature* **431,** 789-95.

33. Varela, J. A., Sen, K., Gibson, J., Fost, J., Abbott, L. F. & Nelson, S. B. (1997) *J Neurosci* **17,** 7926-40.

34. Auld, D. S. & Robitaille, R. (2003) *Neuron* **40,** 389-400.

35. Bullock, T. H., Bennett, M. V., Johnston, D., Josephson, R., Marder, E. & Fields, R. D. (2005) *Science* **310,** 791-3.

36. Fields, R. D. & Stevens-Graham, B. (2002) *Science* **298,** 556-62.

37. Shadlen, M. N. & Newsome, W. T. (1998) *J Neurosci* **18,** 3870-96.

38. Rieke, F., Warland, D., e Ruyter van Steveninck, R. & Bialek, W. (1999) *Spikes: exploring the neural code* (MIT Press, Cambridge).

39. Softky, W. R. (1995) *Curr Opin Neurobiol* **5,** 239-47.

40. Shannon, C. E. (1948) *Bell System Technical Journal* **27.**

41. Berman, N. J. & Maler, L. (1998) *J Neurophysiol* **80,** 3173-96.

42. Chacron, M. J., Doiron, B., Maler, L., Longtin, A. & Bastian, J. (2003) *Nature* **423,** 77-81.

43. Elhilali, M., Fritz, J. B., Klein, D. J., Simon, J. Z. & Shamma, S. A. (2004) *J Neurosci* **24,** 1159-72.

44. Middleton, J. W., Benda, J., Longtin, A. & Maler, L. (2006) *Proc Natl Acad Sci U S A* **103,** 14596-14601.

45. Schouten, J. F., Ritsma, R. J. & Cardozo, B. L. (1962) *J Acoust Soc Am* **34,** 1418-1424.

46. Borst, A. & Theunissen, F. E. (1999) *Nat Neurosci* **2,** 947-57.

47. Roddey, J. C., Girish, B. & Miller, J. P. (2000) *J Comput Neurosci* **8,** 95-112.

48. Baker, C. L., Jr. (1999) *Curr Opin Neurobiol* **9,** 461-6.

49. Andermann, M. L., Ritt, J., Neimark, M. A. & Moore, C. I. (2004) *Neuron* **42,** 451-63.

50. Buzsaki, G. & Draguhn, A. (2004) *Science* **304,** 1926-9.

51. Rangarajan, G. & Ding, M. (2003) in *Lecture notes in physics* (Springer-Verlag, Berlin), Vol. 621.

52. Simoncelli, E. P. & Olshausen, B. A. (2001) *Annu Rev Neurosci* **24,** 1193-216.

53. Voss, R. F. & Clarke, J. (1978) *J Acoust Soc Am* **63,** 258-63.

54. Teich, M. C. (1992) in *Single neuron computation*, eds. McKenna, J. D. T. & Zornetzer, S. F. (Academic, San Diego), pp. 589-622.

55. Teich, M. C. (1989) *IEEE Trans Biomed Eng* **36,** 150-60.

56. Chacron, M. J., Longtin, A. & Maler, L. (2001) *J Neurosci* **21,** 5328-43.

57. Ratnam, R. & Nelson, M. E. (2000) *J Neurosci* **20,** 6672-83.

58. Bahar, S., Kantelhardt, J. W., Neiman, A., Rego, H. H. A., Russell, D. F., Wilkens, L., Bunde, A. & Moss, F. (2001) *Europhys Lett* **56,** 454-60.

59. Cox, D. R. & Lewis, P. A. W. (1966) *The statistical analysis of series of events* (Methun, London).

60. Racicot, D. M. & Longtin, A. (1997) *Physica D* **104,** 184-204.

61. note, p.

62. Fano, U. (1947) *Phys Rev* **72,** 26-9.

63. Risken, H. (1996) *The Fokker-Planck equation* (Springer, Berlin).

64. Longtin, A., Laing, C. & Chacron, M. J. (2003) in *Processes with long-range correlations: theory and applications*, eds. Rangarajan, G. & Ding, M. (Springer-Verlag, Berlin), Vol. 621, pp. 286-306.

65. Denisov, S. I. & Horsthemke, W. (2002) *Phys Rev E Stat Nonlin Soft Matter Phys* **65,** 031105.

66. Dialynas, T. E., Lindenberg, K. & Tsironis, G. P. (1997) *Phys Rev E* **56,** 3976-85.

67. Linkenkaer-Hansen, K., Nikouline, V. V., Palva, J. M. & Ilmoniemi, R. J. (2001) *J Neurosci* **21,** 1370-7.

68. Salinas, E. & Sejnowski, T. J. (2002) *Neural Comput* **14,** 2111-55.

69. Sompolinsky, H., Yoon, H., Kang, K. & Shamir, M. (2001) *Phys Rev E Stat Nonlin Soft Matter Phys* **64,** 051904.

70. Rangarajan, G. & Ding, M. (2000) *Phys Rev E Stat Phys Plasmas Fluids Relat Interdiscip Topics* **61,** 4991-5001.

71. Lowen, S. B., Cash, S. S., Poo, M. & Teich, M. C. (1997) *J Neurosci* **17,** 5666-77.

72. Lowen, S. B. & Teich, M. C. (1992) *J Acoust Soc Am* **92,** 803-6.

73. Lowen, S. B. & Teich, M. C. (1996) *J Acoust Soc Am* **99,** 3585-91.

74. Teich, M. C., Heneghan, C., Lowen, S. B., Ozaki, T. & Kaplan, E. (1997) *J Opt Soc Am A Opt Image Sci Vis* **14,** 529-46.

75. Teich, M. C., Turcott, R. G. & Siegel, R. M. (1996) *IEEE Eng Med Biol Mag* **15,** 79-87.

76. Turcott, R. G. & Teich, M. C. (1996) *Ann Biomed Eng* **24,** 269-93.

77. Nelson, M. E. & Maciver, M. A. (1999) *J Exp Biol* **202,** 1195-203.

78. Chacron, M. J., Longtin, A., St-Hilaire, M. & Maler, L. (2000) *Phys Rev Lett* **85,** 1576-9.

79. Chacron, M. J., Pakdaman, K. & Longtin, A. (2003) *Neural Comput* **15,** 253-78.

80. Abbott, L. F. & Regehr, W. G. (2004) *Nature* **431,** 796-803.

81. Abbott, L. F., Varela, J. A., Sen, K. & Nelson, S. B. (1997) *Science* **275,** 220-4.

82. Fuhrmann, G., Segev, I., Markram, H. & Tsodyks, M. (2002) *J Neurophysiol* **87,** 140-8.

83. Goldman, M. S. (2004) *Neural Comput* **16,** 1137-62.

84. Goldman, M. S., Maldonado, P. & Abbott, L. F. (2002) *J Neurosci* **22,** 584-91.

85. Fortune, E. S. & Rose, G. J. (2000) *J Neurosci* **20,** 7122-30.

86. Fortune, E. S. & Rose, G. J. (2002) *J Physiol Paris* **96,** 539-45.

87. Fortune, E. S. & Rose, G. J. (2001) *Trends Neurosci* **24,** 381-5.

88. Lewis, J. E. & Maler, L. (2004) *J Neurophysiol* **91,** 1064-70.

89. Rice, S. O. (1954) *Mathematical analysis of random noise* (Dover, New York, NY).

90. Cover, T. M. & Thomas, J. A. (1991) *Elements of information theory* (John Wiley & Sons, Inc., New York).

91. Middleton, J. W., Chacron, M. J., Lindner, B. & Longtin, A. (2003) *Phys Rev E Stat Nonlin Soft Matter Phys* **68,** 021920.

92. Gabbiani, F. & Koch, C. (1998) in *Methods in neuronal modelling: from ions to networks*, eds. Koch, C. & Segev, I. (MIT Press, Cambridge).

93. Cox, D. R. & Lewis, P. A. W. (1978) *The statistical analysis of series of events* (Chapman and Hall, London).

94. Chacron, M. J., Lindner, B. & Longtin, A. (2004) *Phys Rev Lett* **92,** 080601.

95. Chacron, M. J., Maler, L. & Bastian, J. (2005) *Nat Neurosci* **8,** 673-8.

96. Mar, D. J., Chow, C. C., Gerstner, W., Adams, R. W. & Collins, J. J. (1999) *Proc Natl Acad Sci U S A* **96,** 10450-5.

97. Silberberg, G., Bethge, M., Markram, H., Pawelzik, K. & Tsodyks, M. (2004) *J Neurophysiol* **91,** 704-9.

98. Burns, E. M. & Viemeister, N. F. (1976) *J Acoust Soc Am* **60,** 863-9.

99. Viemeister, N. F. (1979) *J Acoust Soc Am* **66,** 1364-80.

100. Grosof, D. H., Shapley, R. M. & Hawken, M. J. (1993) *Nature* **365,** 550-2.

101. Mareschal, I. & Baker, C. L., Jr. (1998) *Nat Neurosci* **1,** 150-4.

102. McGraw, P. V., Levi, D. M. & Whitaker, D. (1999) *Nat Neurosci* **2,** 479-84.

103. Shapley, R. (1998) *Nat Neurosci* **1,** 95-6.

104. Zhou, Y. X. & Baker, C. L., Jr. (1993) *Science* **261,** 98-101.

105. Zhou, Y. X. & Baker, C. L., Jr. (1996) *J Neurophysiol* **75,** 1038-50.

106. Tanaka, H. & Ohzawa, I. (2006) *J Neurosci* **26,** 4370-82.

107. Tan, E. W., Nizar, J. M., Carrera, G. E. & Fortune, E. S. (2005) *Behav Brain Res* **164,** 83-92.

108. Moortgat, K. T., Keller, C. H., Bullock, T. H. & Sejnowski, T. J. (1998) *Proc Natl Acad Sci U S A* **95,** 4684-9.

109. Bastian, J. & Courtright, J. (1991) *J Comp Physiol [A]* **168,** 393-407.

110. Bastian, J., Courtright, J. & Crawford, J. (1993) *J Comp Physiol [A]* **173,** 257-74.

111. Bastian, J. & Bratton, B. (1990) *J Neurosci* **10,** 1226-40.

112. Benda, J., Longtin, A. & Maler, L. (2005) *J Neurosci* **25,** 2312-21.

113. Bastian, J., Chacron, M. J. & Maler, L. (2002) *J Neurosci* **22,** 4577-90.

114. Doiron, B., Lindner, B., Longtin, A., Maler, L. & Bastian, J. (2004) *Phys Rev Lett* **93,** 048101.

115. Bastian, J., Chacron, M. J. & Maler, L. (2004) *Neuron* **41,** 767-79.

116. Chacron, M. J., Maler, L. & Bastian, J. (2005) *J Neurosci* **25,** 5521-32.

117. Oppenheim, A. V. & Schafer, R. W. (1999) *Discrete time signal processing* (Prentice Hall, Upper Saddle River, NJ).

118. Wessel, R., Koch, C. & Gabbiani, F. (1996) *J Neurophysiol* **75,** 2280-93.

119. Maler, L. & Mugnaini, E. (1994) *J Comp Neurol* **345,** 224-52.

120. Maler, L. (1979) *J Comp Neurol* **183,** 323-63.

121. Yamamoto, T., Maler, L., Hertzberg, E. L. & Nagy, J. I. (1989) *J Comp Neurol* **289,** 509-36.

122. Maler, L., Sas, E. K. & Rogers, J. (1981) *J Comp Neurol* **195,** 87-139.

123. Middleton, J. W., Harvey-Girard, E., Longtin, A. & Maler, L. (2006) *Phys Rev Lett* **submitted.**

124. Demb, J. B., Zaghloul, K. & Sterling, P. (2001) *Neuron* **32,** 711-21.

125. Eggermont, J. J. (1998) *J Neurophysiol* **80,** 2743-64.

126. Griffin, S. J., Bernstein, L. R., Ingham, N. J. & McAlpine, D. (2005) *J Neurophysiol* **93,** 3463-78.

127. Liang, L., Lu, T. & Wang, X. (2002) *J Neurophysiol* **87,** 2237-61.

128. Schreiner, C. E. & Urbas, J. V. (1988) *Hear Res* **32,** 49-63.

129. Shackleton, T. M., Skottun, B. C., Arnott, R. H. & Palmer, A. R. (2003) *J Neurosci* **23,** 716-24.

130. Chialvo, D. R. (2003) *Chaos* **13,** 1226-30.

131. Attias, H. & Schreiner, C. E. (1999) *Low-order temporal statistics of natural sounds* (MIT Press, Cambridge, MA).

132. Nelken, I., Rotman, Y. & Bar Yosef, O. (1999) *Nature* **397,** 154-7.

133. Burns, E. M. & Viemeister, N. F. (1981) *J Acoust Soc Am* **70,** 1655-60.

134. Rose, G. J., Etter, N. & Alder, T. B. (1994) *J Neurosci* **175,** 467-474.

135. Hasenstaub, A., Shu, Y., Haider, B., Kraushaar, U., Duque, A. & McCormick, D. A. (2005) *Neuron* **47,** 423-35.

136. Benardo, L. S. (1994) *J Physiol* **476,** 203-15.

137. Shao, Z. & Burkhalter, A. (1999) *J Neurophysiol* **81,** 1014-24.

138. Tamas, G., Lorincz, A., Simon, A. & Szabadics, J. (2003) *Science* **299,** 1902-5.

139. Thomson, A. M. & Destexhe, A. (1999) *Neuroscience* **92,** 1193-215.

140. Gammaitoni, L., Hanggi, P., Jung, P. & Marchesoni, F. (1998) *Rev Mod Phys* **70,** 223-288.

141. Jung, P. (1993) *Phys Rep* **234,** 175-295.

142. Lindner, B., Garcia-Ojalvo, J., Neiman, A. & Schimansky-Geier, L. (2004) *Phys Rep* **392,** 321-424.

143. Zhou, C. S., Kurths, J., Allaria, E., Boccaletti, S., Meucci, R. & Arecchi, F. T. (2003) *Phys Rev E Stat Nonlin Soft Matter Phys* **67,** 015205.

144. Dykman, M. I., Mannella, R., McClintock, P. V., Stein, N. D. & Stocks, N. G. (1993) *Physical Review. E. Statistical Physics, Plasmas, Fluids, And Related Interdisciplinary Topics* **47,** 3996-4009.

145. Neiman, A. & Schimansky-Geier, L. (1994) *Physical Review Letters* **72,** 2988-2991.

146. Sherwin, M. S. & Zettl, A. (1985) *Physical Review B. Condensed Matter* **32,** 5536-5539.

147. Inchiosa, M. E., In, V., Bulsara, A. R., Wiesenfeld, K., Heath, T. & Choi, M. H. (2001) *Phys Rev E Stat Nonlin Soft Matter Phys* **63,** 066114.

148. Baker, C. L., Jr. & Mareschal, I. (2001) *Prog Brain Res* **134,** 171-91.

149. Nikouline, V. V., Linkenkaer-Hansen, K., Huttunen, J. & Ilmoniemi, R. J. (2001) *Neuroreport* **12,** 2487-91.

150. Tuckwell, H. C. (1988) *Introduction to theoretical neurobiology* (Cambridge University Press, Cambridge MA).

151. Fourcaud, N. & Brunel, N. (2002) *Neural Comput* **14,** 2057-110.

152. Lindner, B. & Schimansky-Geier, L. (2001) *Phys Rev Lett* **86,** 2934-7.

153. Brunel, N., Hakim, V. & Richardson, M. J. (2003) *Phys Rev E Stat Nonlin Soft Matter Phys* **67,** 051916.

154. Berman, N. J. & Maler, L. (1998) *J Neurophysiol* **80,** 3214-32.

155. Borst, A. & Haag, J. (2001) *J Comput Neurosci* **10,** 213-21.

156. Rauch, A., La Camera, G., Luscher, H. R., Senn, W. & Fusi, S. (2003) *J Neurophysiol* **90,** 1598-612.

157. Womelsdorf, T., Fries, P., Mitra, P. P. & Desimone, R. (2006) *Nature* **439,** 733-6.

158. Stocks, N. G. (2000) *Phys Rev Lett* **84,** 2310-3.

159. Reyes, A. D. (2003) *Nat Neurosci* **6,** 593-9.

160. Gabbiani, F., Metzner, W., Wessel, R. & Koch, C. (1996) *Nature* **384,** 564-7.

161. Dayan, P. & Abbot, L. F. (2001) *Theoretical Neuroscience* (MIT Press, Cambridge).

162. Rieke, F., Warland, D., van Stevenick, R. R. & Bialek, W. (1997) *Spikes: exploring the neural code* (MIT Press, Cambridge).

163. Joris, P. X., Schreiner, C. E. & Rees, A. (2004) *Physiol Rev* **84,** 541-77.

164. Galarreta, M. & Hestrin, S. (2001) *Nat Rev Neurosci* **2,** 425-33.

165. Lewis, T. J. & Rinzel, J. (2003) *J Comput Neurosci* **14,** 283-309.

166. Chow, C. C. & Kopell, N. (2000) *Neural Comput* **12,** 1643-78.

167. Gerstner, W. & Kistler, W. M. (2002) *Spiking Neuron Models: Single Neurons, Populations, Plascticity* (Cambrige University Press, Cambridge, UK).

168. Hodgkin, A. L. & Huxley, A. F. (1952) *J Physiol* **117,** 500-44.

169. Rulkov, N. F., Sushchik, M. M., Tsimring, L. S. & Abarbanel, H. D. (1995) *Physical Review. E. Statistical Physics, Plasmas, Fluids, And Related Interdisciplinary Topics* **51,** 980-994.

170. Rosenblum, M. G., Pikovsky, A. S. & Kurths, J. (1996) *Physical Review Letters* **76,** 1804-1807.

171. Hunter, J. D., Milton, J. G., Thomas, P. J. & Cowan, J. D. (1998) *J Neurophysiol* **80,** 1427-38.

172. Ritt, J. (2003) *Phys Rev E Stat Nonlin Soft Matter Phys* **68,** 041915.

173. Tiesinga, P. H., Fellous, J. M. & Sejnowski, T. J. (2002) *Neural Comput* **14,** 1629-50.

174. Tiesinga, P. H., Fellous, J. M. & Sejnowski, T. J. (2002) *Neurocomp* **44-46,** 195-200.

175. Strogatz, S. H. (2001) *Nonlinear dynamics and chaos: with applications to physics, biology, chemistry and engineering* (Perseus Books Publishing, Cambridge).

176. Chow, C. C., White, J. A., Ritt, J. & Kopell, N. (1998) *J Comput Neurosci* **5,** 407-20.

177. Csicsvari, J., Jamieson, B., Wise, K. D. & Buzsaki, G. (2003) *Neuron* **37,** 311-22.

178. Machens, C. K., Gollisch, T., Kolesnikova, O. & Herz, A. V. (2005) *Neuron* **47,** 447-56.

179. Marsat, G. & Pollack, G. S. (2004) *J Neurophysiol* **92,** 939-48.

180. Carr, C. E. (1993) *Annu Rev Neurosci* **16,** 223-43.

181. deCharms, R. C., Blake, D. T. & Merzenich, M. M. (1998) *Science* **280,** 1439-43.

182. Kilgard, M. P. & Merzenich, M. M. (1998) *Nat Neurosci* **1,** 727-31.

183. Buracas, G. T., Zador, A. M., DeWeese, M. R. & Albright, T. D. (1998) *Neuron* **20,** 959-69.

184. Gutig, R. & Sompolinsky, H. (2006) *Nat Neurosci* **9,** 420-8.

185. Destexhe, A. & Contreras, D. (2006) *Science* **314,** 85-90.